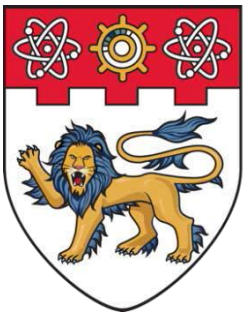

NANYANG TECHNOLOGICAL UNIVERSITY
SINGAPORE

DENSITY FUNCTIONAL THEORY INVESTIGATION OF EMERGING TWO-DIMENSIONAL HETEROSTRUCTURED MATERIALS

KISTANOV ANDREY

SCHOOL OF MECHANICAL AND AEROSPACE ENGINEERING

2019

DENSITY FUNCTIONAL THEORY INVESTIGATION OF EMERGING TWO-DIMENSIONAL HETEROSTRUCTURED MATERIALS

KISTANOV ANDREY

School of Mechanical and Aerospace Engineering

A thesis submitted to the Nanyang Technological University
in partial fulfillment of the requirement for the degree of
Doctor of Philosophy

2019

Statement of Originality

I hereby certify that the work embodied in this thesis is the result of original research, is free of plagiarised materials, and has not been submitted for a higher degree to any other University or Institution.

9 May 2019 . . . . .Andrey Kistanov . . . . . .
. . . . . .
Date

Supervisor Declaration Statement

I have reviewed the content and presentation style of this thesis and declare it is free of plagiarism and of sufficient grammatical clarity to be examined. To the best of my knowledge, the research and writing are those of the candidate except as acknowledged in the Author Attribution Statement. I confirm that the investigations were conducted in accord with the ethics policies and integrity standards of Nanyang Technological University and that the research data are presented honestly and without prejudice.

2 July 2019

. . . . . .

Date

. . . . . .Zhou Kun . . . . . .

Authorship Attribution Statement

This thesis contains material from 7 papers published in the following peer-reviewed journals where I was the first and/or corresponding author.

Chapter 3 is published as

- A.A. Kistanov, Y. Cai, K. Zhou, S.V. Dmitriev, Y.W. Zhang. Large electronic anisotropy and enhanced chemical activity of highly rippled phosphorene. *The Journal of Physical Chemistry C* **120**(12), 6876–6884 (2016)
- A.A. Kistanov, Y. Cai, K. Zhou, S.V. Dmitriev, Y.W. Zhang. The role of H_2O and O_2 molecules and phosphorus vacancies in the structure instability of phosphorene. *2D Materials* **4**(1), 015010 (2017).

The contributions of the co-authors are as follows:

- Associate Professor Zhou and Dr. Zhang proposed the ideas of the research works and revised and edited the drafts of the manuscripts.
- I performed all the calculations, collected the data, conducted the data evaluations, and drafted the manuscripts.
- Dr. Cai provided technical support of the research and revised the drafts of the manuscripts.
- Professor Dmitriev revised the drafts of the manuscripts.

Chapter 4 is published as

- A.A. Kistanov, Y. Cai, K. Zhou, N. Srikanth, S.V. Dmitriev, Y.W. Zhang. Exploring the charge localization and band gap opening of borophene: A first-principles study. *Nanoscale* **10**, 1403–1410 (2018).
- A.A. Kistanov, D. Kripalani, Y. Cai, K. Zhou, S.V. Dmitriev, Y.W. Zhang. A first-principles study on the adsorption of small molecules on antimonene: Oxidation tendency and stability. *Journal of Materials Chemistry C* **6**, 4308–4317 (2018).
- A.A. Kistanov, Y. Cai, K. Zhou, S.V. Dmitriev, Y.W. Zhang. Atomic-scale mechanisms of defect- and light-induced oxidation and degradation of InSe. *Journal of Materials Chemistry C* **6**, 518–525 (2018).

The contributions of the co-authors are as follows:

- Associate Professor Zhou and Dr. Zhang proposed the ideas of the research works and revised and edited the drafts of the manuscripts.
- I performed all the calculations, collected the data, conducted the data evaluations, and drafted the manuscripts.
- Dr. Cai provided technical support of the research and revised the drafts of the manuscripts.
- Professor Dmitriev, Dr. Srikanth and Mr. Kripalani revised the draft(s) of their co-authored manuscript(s).

Chapter 5 is published as

- A.A. Kistanov, Y. Cai, K. Zhou, S.V. Dmitriev, Y.W. Zhang. Effects of graphene/BN encapsulation, surface functionalization and molecular adsorption on the electronic properties of layered InSe: A first-principles study. *Physical Chemistry Chemical Physics* **20**, 12939–12947 (2018).
- A.A. Kistanov, Y. Cai, Y.W. Zhang, S.V. Dmitriev, K. Zhou. Strain and water effects on the electronic structure and chemical activity of in-plane graphene/silicene heterostructure. *Journal of Physics Condensed Matter* **29**(9), 095302 (2017).

The contributions of the co-authors are as follows:

- Associate Professor Zhou and Dr. Zhang proposed the ideas of the research works and revised and edited the drafts of the manuscripts.
- I performed all the calculations, collected the data, conducted the data evaluations, and drafted the manuscripts.
- Dr. Cai provided technical support of the research and revised the drafts of the manuscripts.
- Professor Dmitriev the drafts of the manuscripts.

9 May 2019
. . . . . .
Date

. . . . . .Andrey Kistanov . . . . . .

Acknowledgements

I would like to express my sincere thanks to and acknowledge the endless support from my supervisor Associate Professor Zhou Kun and co-supervisor Dr. Zhang Yong-Wei. I am infinitely grateful for their efficient guidance and encouragement. This research would not have been possible without their constructive advice and help. It has been my great honour and pleasure to study and work under their supervision.

I would also like to give my kind appreciation to Dr. Cai Yongqing, my friendly collaborator from the Institute of High Performance Computing, Agency for Science, Technology and Research (A*STAR), Singapore. His great experience, useful suggestions and kind help, undoubtedly, have made my research work fruitful.

I wish to address my special thanks to the A*STAR for financially supporting my Ph.D. study and the Nanyang Technological University for providing all the necessary support for my research work.

I am also grateful to the A*STAR Computational Resource Centre, Singapore and the National Supercomputing Centre, Singapore for computational support.

I express my special appreciation to Professor Sergey V. Dmitriev for his helpful advice and kind help.

Last but not least, I am immensely indebted to my family, colleagues and friends for their warm-hearted support during my Ph.D. life.

Table of Contents

Abstract

Over the last few years, many studies have been performed on two-dimensional (2D) materials, such as graphene, silicone and MoS_2, owing to their unique properties and successful applications in nanoelectronics, photonics and other fields. It has been shown that the structural stability and various properties of 2D materials can be influenced by different factors, such as defect and strain engineering, electric field, edge functionalization, and adatom adsorption. Furthermore, the internal vacancy defects can easily emerge at the surface of 2D materials in the manufacturing process. Meanwhile, it is well known that 2D materials possess high chemical activity. Therefore, during the manufacturing and application of 2D materials, it is important to control their structural stability and properties which may change significantly under the influence of environmental and exploitation conditions.

Hybrid 2D materials such as graphene-boron nitride (BN), graphene-silicene and graphene-MoS_2 have also been found to be superior to their individual 2D counterparts in terms of structural stability and properties. For instance, chemically unstable 2D materials, like silicene and phosphorene, can be protected by their passivation by chemically more stable 2D materials, such as graphene and BN.

The recent successful fabrication of several new 2D materials (phosphorene, borophene, InSe and antimonene) - has triggered increasing attention to these materials due to their distinctive opto-electronic and mechanical properties, such as a wide and tunable band gap, high carrier mobility and flexibility. However, these unique 2D materials are still poorly investigated.

Therefore, this Ph.D. study has aimed to systematically investigate the atomic structure, opto-electronic properties and chemical activity of phosphorene, InSe, borophene and antimonene under the influence of various factors, such as large deformations, vacancies and molecules of the surrounding environment. In addition, heterostructures of these 2D materials have been considered. The investigations have been carried out within the framework of the density functional theory using first-principles calculations.

The studies of the atomic structure, electronic properties and chemical activity of phosphorene under the strain and defect engineering have shown that phosphorene enables the withstanding of a large compressive strain and exhibits anisotropic electronic properties. Moreover, compressive strain and the presence of mono- (MV) and di- (DV) vacancy defects significantly alter the chemical activity of phosphorene as evidenced by the enhanced adsorption and charge transfer between the environmental molecules, such as H_2O, O_2 and NO, and phosphorene surface.

Typical methods, such as defect engineering and surface functionalization, have been applied for the exploration of possible avenues for opening the band gap of borophene. The metallicity in borophene has been found to be immune to the surface functionalization and the presence of vacancies. More importantly, the anisotropy of the electronic properties and the nature of the orbitals at the Fermi level can be altered upon the surface functionalization, enabling the modulation of the borophene properties. Due to the high density of itinerant electrons in the atomically thin borophene sheet, the band gap opening via quantum confinement, which is effective for graphene, becomes ineffective for borophene.

Several critical issues with the structural degradation of InSe due to oxygen and humidity at ambient conditions have been studied. The oxidation of monolayer InSe has been

explored by examining the roles of light illumination, oxygen, water and defects. Pristine InSe has shown a much lower oxygen affinity than MoS_2 and phosphorene. However, the presence of MV and light excitation have significantly accelerated the oxidation by greatly decreasing the barrier through forming chemical oxygen species. These atomic O species, which are associated with strong polar O-In bonds, can quench the defective states of MV, and further act as the adsorption and trapping centres of H_2O molecules. The apical O atoms in the form of terminated Se-O bonds have been shown to allow even spontaneous water splitting and the formation of hydroxyl groups at room temperature. Accordingly, the following three strategies have been proposed to suppress the oxidation of InSe: i) insulating InSe from O_2 molecules; ii) maintaining the InSe surface stoichiometry; iii) avoiding the exposure of InSe to light illumination.

The energetics and charge transfer of small molecules (CO, NO, NO_2, H_2O, O_2, NH_3, and H_2) adsorbed on antimonene have been considered. NO_2 has the strongest adsorption energy among all the considered molecules, which may arise from the coexistence of a large dipole moment of NO_2 and resonant molecular levels with the antimonene states. The strong acceptors, like NO_2, NO, and O_2, bind more strongly to the antimonene surface than the phosphorene surface, while the weak acceptors, like CO, H_2, and NH_3, show a weaker adsorption. The interaction of O_2 with antimonene has been found to be much stronger than that with phosphorene. The found low kinetic barrier for the splitting of the O_2 molecule on antimonene suggests that pristine antimonene may undergo oxidation in ambient conditions. Fortunately, the acceptor role of H_2O on antimonene, opposite to the donor role in phosphorene, helps to suppress further structural degradation of the oxidized antimonene by preventing the proton

transfer between water molecules and oxygen species to form acids. By comparing antimonene with phosphorene and InSe, it has been predicted that the acceptor role of water may be a necessary condition for a good environmental stability of such 2D layers to avoid structural decomposition.

Individual 2D materials have been combined to form heterostructures. The investigations of the effect of compressive (tensile) strain on the chemical activity of the in-plane graphene-silicene heterostructure with the H_2O molecule have shown that compressive (tensile) strain is able to increase (decrease) the binding energy of the H_2O molecule compared with the adsorption on a planar surface. At the same time the charge transfer between H_2O molecule and the graphene-silicene sheet can be modulated by strain. The in-plane graphene-silicene heterostructure has been found to be metallic in a strain range from -7% (compression) to +7% (tension). In addition, the modulation of monolayer InSe electronic properties by graphene and BN encapsulation has been found. In particular, graphene (donor) and BN (acceptor) have been found to play an opposite charge donating role in InSe, which is dramatically different from phosphorene, where both graphene and BN play the same role (donor). The changing of the interlayer spacing of the InSe-graphene (BN) heterostructure has been predicted as an effective technique to dramatically change the bands alignment and control the band gap of the heterostructure.

This Ph.D. dissertation has explored and explained in detail the unique structural and opto-electronic properties of novel 2D materials and their hybrids. This research will not only help to understand the routes for controlling and modifying the properties of 2D materials and thus to enhance their performance, but also contribute to the development of techniques for the growth, storage and applications of different 2D materials.

List of Publications

[1]. **A. A. Kistanov**, Y. Cai, K. Zhou, N. Srikanth, S. V. Dmitriev, Y. W. Zhang. Exploring the charge localization and band gap opening of borophene: A first-principles study. *Nanoscale*, 2018, **10**, 1403–1410. (Impact Factor 2017: 7.233)

[2]. **A. A. Kistanov**, D. Kripalani, Y. Cai, K. Zhou, S. V. Dmitriev, Y. W. Zhang. A first-principles study on the adsorption of small molecules on antimonene: Oxidation tendency and stability. *Journal of Materials Chemistry C*, 2018, **6**, 4308–4317. (Impact Factor 2017: 5.976)

[3]. **A. A. Kistanov**, Y. Cai, K. Zhou, S. V. Dmitriev, Y. W. Zhang. Atomic-scale mechanisms of defect- and light-induced oxidation and degradation of InSe. *Journal of Materials Chemistry C*, 2018, **6**, 518–525. (Impact Factor 2017: 5.976)

[4]. **A. A. Kistanov**, Y. Cai, K. Zhou, S. V. Dmitriev, Y. W. Zhang. Effects of graphene/BN encapsulation, surface functionalization and molecular adsorption on the electronic properties of layered InSe: A first-principles study. *Physical Chemistry Chemical Physics*, 2018, **20**, 12939–12947. (Impact Factor 2017: 3.906)

[5]. D. R. Kripalani, A. A. Kistanov, Y. Cai, M. Xue, K. Zhou. Strain engineering of antimonene by a first-principles study: Mechanical and electronic properties. *Physical Review B*, 2018, **98**, 085410. (Impact Factor 2017: 3.813)

[6]. **A. A. Kistanov**, Y. Cai, K. Zhou, S. V. Dmitriev, Y. W. Zhang. The role of H_2O and O_2 molecules and phosphorus vacancies in the structure instability of phosphorene. *2D Materials*, 2017, **4**, 015010. (Impact Factor 2017: 7.042)

[7]. **A. A. Kistanov**, Y. Cai, Y. W. Zhang, S. V. Dmitriev, K. Zhou. Strain and water effects on the electronic structure and chemical activity of in-plane graphene/silicene heterostructure. *Journal of Physics Condensed Matter*, 2017, **29**, 095302. (Impact Factor 2017: 2.617)

[8]. **A. A. Kistanov**, Y. Cai, K. Zhou, S. V. Dmitriev, Y. W. Zhang. Large electronic anisotropy and enhanced chemical activity of highly rippled phosphorene. *The Journal of Physical Chemistry C*, 2016, **120**, 6876–6884. (Impact Factor 2017: 4.484)

[9]. A. R. Davletshin, S. V. Ustiuzhanina, **A. A. Kistanov**, D. Saadatmand, S. V. Dmitriev, K. Zhou, E. A. Korznikova. Electronic structure of graphene– and BN–supported phosphorene. *Physica B: Condensed Matter*, 2018, **534**, 63–67. (Impact Factor 2017: 1.453)

List of Figures

List of Tables

Chapter 1 Introduction

Since 2004 when a single layer of graphite, graphene, was successfully isolated for the first time, a great deal of research has been directed to investigate two-dimensional (2D) materials because of their unusual characteristics and potential applications as semiconductors, electrodes, photovoltaics, etc. Nowadays many researchers in the fields of physics, chemistry, engineering, and biology are studying 2D materials, ranging from fundamental science to novel applications.

1.1 2D materials

One of the goals of modern science is the intensive search of ways to obtain new 2D materials and to deeply investigate already known ones. Recent experimental and theoretical researches have reported dozens of different 2D materials and their properties [1]. In general, 2D materials can be divided into different classes [2]:

- **X-enes.** They are materials with one atom-thin layer, consisting of atoms belongs to one single element and arranged in a hexagonal order. The most known examples are graphene [2], silicene [3], germanene [4], and phosphorene [5]. Figs. 1.1(a)-(c) show the typical structures of those materials.

- **X-anes and Fluoro-X-enes.** X-anes have a hexagonal structure with the hydrogen atoms bonded to the surface on both sides in a succession, above or below the plane. Figs. 1.2(a) and (b) show the typical structure of the X-anes. The Fluoro-X-enes copy the X-anes structure, but their lattice atoms are bonded out of the plane to fluorine atoms, instead of hydrogen atoms.

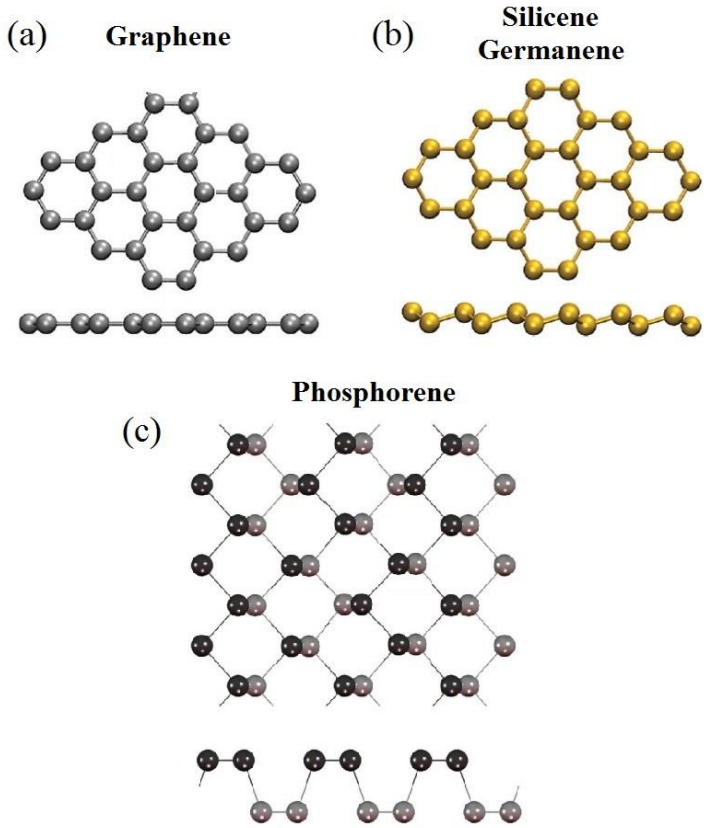

Fig. 1.1. The structure of atomically thin 2D materials: (a) graphene, (b) silicene (germanene) and (c) phosphorene [1].

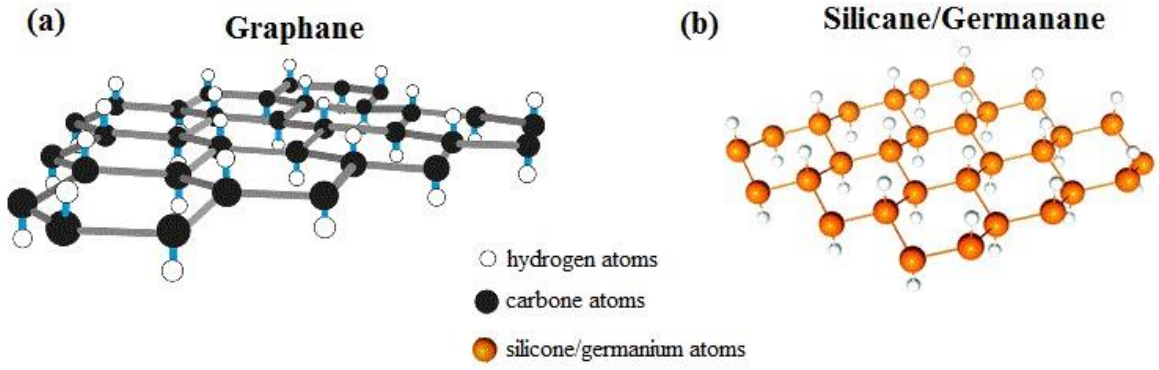

Fig. 1.2. The structure of (a) graphene and (b) silicane (germanane) [6]. Black, orange and white spheres represent carbon, silicon or germanium, and hydrogen atoms, respectively.

• **TMDs.** Transition metal dichalcogenides (TMDs) represent a group of 2D layered materials that consist of transition metal (M) and chalcogen (Q). Single layer TMDs consist of three atomic layers, where the M atom layer is placed between two layers of Q atoms. One of the most famous examples in this group of 2D materials - MoS_2, its lattice structure is shown in Fig. 1.3.

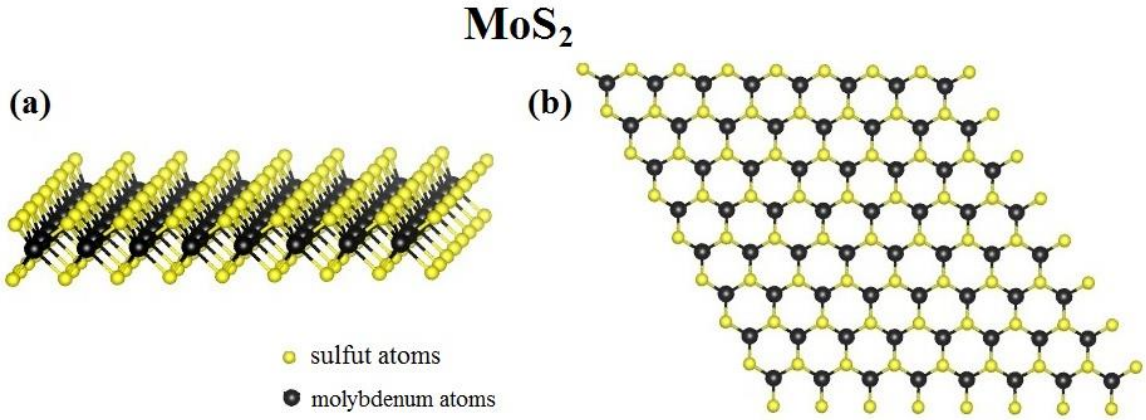

Fig. 1.3. The structure of MoS_2: (a) side-view and (b) top-view [7]. Black and yellow spheres represent molybdenum and sulphur atoms, respectively.

1.2 Motivations

The electronic properties of 2D materials directly depend on their atomic structures. During the manufacturing process, the formation of typical point defects, such as vacancies, together with the effects of environment significantly affects the structures of 2D materials and, hence, their properties. Moreover, the opto-electronic properties of 2D materials can be modulated via different methods, including strain engineering [8-12], adatom adsorption and chemical functionalization [13, 14], and electric field engineering [15]. Therefore, the deep knowledge on the nature and mechanisms of changes in the atomic and electronic structures

of 2D materials is not only of scientific significance but also of great implication for their potential device applications.

The recent success in the fabrication of both the horizontally and vertically stacked 2D heterostructures has become an important step for the realization of the small-scale and flexible electronic and optical devices with a high density of functional components. The found synergistic effects in these 2D heterostructures are promising both for improvements of existing applications and for discoveries of new phenomena [16-18]. So far, most of the previous studies have been focused on the investigation of common 2D materials, such as graphene and MoS_2, and their heterostructures, while the new materials such as phosphorene, borophene, InSe, and antimonene have not been explored well. Thus, the investigation of these materials becomes a motivation of this Ph.D. study.

Due to the expensiveness, significant labour inputs and time-cost of the experimental investigations of nanomaterials, atomic simulations are usually conducted before the experiment for its further optimization. Moreover, current computational techniques supported by modern highly effective supercomputers allow reaching the accuracy of simulation results comparable to the accuracy of the results obtained in experiments. Thereby, this Ph.D. study on 2D materials has been conducted using the first-principles simulation, currently one of the most effective and highly predictive computational techniques.

1.3 Objectives

This proposed Ph.D. research investigates the structures and electronic properties of 2D materials and heterostructures via first-principles simulation. Several novel and prospective 2D materials (phosphorene, borophene, InSe, and antimonene) are considered. The general objectives for the research have been set as follows:

- Investigate the structure stability and electronic properties of phosphorene, borophene, InSe, and antimonene, including band structure, charge conductivity, work function etc.
- Consider the effects of defect and strain engineering, isotopic doping and chemical functionalization on the structure integrity and electronic properties and understand the underlying mechanisms.
- Study the changes in the atomic structures and electronic properties taking place in the heterostructures partly formed by the considered 2D materials.
- Evaluate strategies for protection of the structure of 2D materials and its heterostructures, provide the possibilities to control and improve their electronic properties and explore their potential applications in nanoelectronics.

1.4 Report outline

The Ph.D. dissertation contains six chapters. After the introduction in Chapter 1, Chapter 2 gives a comprehensive literature review on the structure, physical, optical, magnetic, and electronic properties of 2D materials, description of the various factors that affect their properties, and discussion of potential applications of 2D materials. Chapter 3

presents the study on the structure stability and electronic properties of phosphorene. In Chapter 4, the electronic properties of borophene, InSe, and antimonene are considered and compared with these of phosphorene. Chapter 5 investigates the electronic properties and chemical activity of 2D hybrid structures. Finally, Chapter 6 concludes the research and proposes future works.

Chapter 2 Literature Review

A major scientific breakthrough in the area of 2D materials was done by Novoselov and his co-workers in 2004, who successfully isolated the single-layer 2D material - graphene [19]. Since then, many theoretical and experimental studies have been performed to discover new 2D materials, understand their properties and explore their applications. In the following, computational methodology and some of these researches are briefly reviewed.

2.1 Modelling of 2D materials and heterostructures

In modelling, the choice of boundary conditions is crucial to properly describe the properties of quantum-mechanical system. For consideration of 2D periodic boundary conditions, software with the local basis functions is usually used [20-24]. The commonly used software packages that are of high computational efficiency in modelling 2D systems are: VASP [25, 26], Abinit [27] and Quantum-Espresso [28] with the integrated plane-wave basis functions. These functions require a vacuum layer to avoid self-interaction between the system and its periodic replication in the direction perpendicular to the lattice plane, since even a weak interaction between layers may have a significant impact on the electronic structure. The size of the simulation system is also important in the plane-wave methods. Clearly, use of 2D boundary conditions can reduce the complexity of interactions of atoms. Compared to the three-dimensional (3D) bulk materials, the calculation of 2D materials is faster and more efficient.

Density functional theory (DFT) has become the most popular approach in solid state physics as this method is able to compute the electronic structure of a solid with an excellent

ratio of computational demand and accuracy [29]. However, there are some specifics in this method. Local density approximation and generalized gradient approximation functionals, such as BP86 (Becke88) [30] and PBE [31], can be implemented easily and the obtained band structures are of excellent quality. They also allow determining the effective masses of holes and electrons [32] and provide adequate conduction band spectrum and structure parameters [33]. However, they are shifted to lower energies, and as a result, the band gaps are often underestimated [34-37]. To generally improve the predicted band gap and make it comparable with the experimental findings, hybrid DFT functionals, such as HSE06 [38] or PBE0 [39] have been developed. The disadvantage of hybrid functionals is their high computational demand compared to generalized gradient approximation.

In this Ph.D. research, the DFT-based first-principles simulation realized through the VASP has been performed. Further, the foundations of the DFT are described, including the Hohenberg-Kohn theorems [40] and the Kohn-Sham equations [41], the local density approximation and the projector augmented-wave method [42]. It should be noted that the following description of the DFT approach closely follows the presentation in standard textbooks on the subject [43].

To describe the electronic structure of a solid, one needs to solve a quantum mechanical problem on the interaction of many-body system which is unsolvable in most cases. It is possible to simplify the problem by using the Born-Oppenheimer approximation and treating only valence electrons and ions, instead of all electrons and nuclei, but the problem remains unsolvable. However, the Born-Oppenheimer approximation allows separating electron and ion degrees of freedom because the ions are typically five orders of magnitude heavier than the electrons. This approximation is almost always true and taken as a basis for the DFT

calculations. A system of electrons bound by one or many nuclei can be described by the non-relativistic Schrödinger equation. The many-body Hamiltonian can be written as in Eq. 2.1:

$$\widehat{H} = \overbrace{-\frac{\hbar^2}{2}\sum_I \frac{\nabla_I^2}{M_I}}^{\text{Nuclei K.E.}} + \overbrace{\frac{1}{2}\sum_{I\neq J}\frac{Z_I Z_J e^2}{4\pi\epsilon_0|\mathrm{R_I}-\mathrm{R_J}|}}^{\text{Nucleus-Nucleus Interaction}} - \overbrace{\frac{\hbar^2}{2m}\sum_i \nabla_i^2}^{\text{Electrons K.E.}} + \underbrace{\frac{1}{2}\sum_{i\neq j}\frac{e^2}{4\pi\epsilon_0|\mathrm{r_i}-\mathrm{r_j}|}}_{\text{Electron-Electron Interaction}} - \underbrace{\sum_{i,I}\frac{Z_I e^2}{4\pi\epsilon_0|\mathrm{r_i}-\mathrm{R_I}|}}_{\text{Electron-Nucleus Interaction}} \tag{2.1}$$

where the first term $[-\frac{\hbar^2}{2}\sum_I \frac{\nabla_I^2}{M_I}]$ represents the kinetic energy of all nuclei, each with mass M_I. The second term $\left[\frac{1}{2}\sum_{I\neq J}\frac{Z_I Z_J e^2}{4\pi\epsilon_0|\mathrm{R_I}-\mathrm{R_J}|}\right]$ represents nucleus-nucleus interactions via Coulomb repulsive forces, which can be calculated efficiently using Ewald's method (which determines the electrostatic potential as well as the energy of point charges in a crystal). The third term $\left[-\frac{\hbar^2}{2m}\sum_i \nabla_i^2\right]$ represents the kinetic energy of electrons, each with mass m. The fourth term $\left[\frac{1}{2}\sum_{i\neq j}\frac{e^2}{4\pi\epsilon_0|\mathrm{r_i}-\mathrm{r_j}|}\right]$ represents the Coulomb interaction within pairs of electrons. The fifth term $\left[-\sum_{i,I}\frac{Z_I e^2}{4\pi\epsilon_0|\mathrm{r_i}-\mathrm{R_I}|}\right]$ represents electron-nucleus Coulomb interactions.

The first step to simplify the above presented Hamiltonian is to invoke the Born-Oppenheimer approximation, which is described in more details in the next section.

2.1.1 Born-Oppenheimer approximation

As it has been noted above, the Born-Oppenheimer approximation [45] simplifies the solution of the many-body Schrödinger equation (Eq. 2.1). This approximation gives two wave equations. The first equation describes the electronic motion, which can be solved separately by further approximations to evaluate the electronic wave function and the ground state energy. The second equation provides a description of the motion of the nuclei. As the result the final Born-Oppenheimer Hamiltonian can be simplified as follows:

$$\widehat{H}^{\mathrm{BO}} = \underbrace{-\frac{\hbar^2}{2m}\sum_i \nabla_i^2}_{\text{Electrons K.E.}} + \underbrace{\frac{1}{2}\sum_{i\neq j}\frac{e^2}{4\pi\epsilon_0|\mathrm{r_i}-\mathrm{r_j}|}}_{\text{Electron-Electron Interaction}} - \underbrace{\sum_{i,I}\frac{Z_I e^2}{4\pi\epsilon_0|\mathrm{r_i}-\mathrm{R_I}|}}_{\text{Electron-Nucleus Interaction}} + \underbrace{\frac{1}{2}\sum_{I\neq J}\frac{Z_I Z_J e^2}{4\pi\epsilon_0|\mathrm{R_I}-\mathrm{R_J}|}}_{\text{Nucleus-Nucleus Interaction}} \tag{2.2}$$

If assume that $\hbar = m_e = e = 4\pi\epsilon_0 = 1$, the Born-Oppenheimer Hamiltonian can be presented as:

$$\widehat{H}^{\mathrm{BO}} = \underbrace{-\frac{1}{2}\sum_i \nabla_i^2}_{\text{Electrons K.E.}} + \underbrace{\frac{1}{2}\sum_{i\neq j}\frac{1}{|\mathbf{r_i}-\mathbf{r_j}|}}_{\text{Electron-Electron Interaction}} - \underbrace{\sum_{i,I}\frac{Z_I}{|\mathbf{r_i}-\mathbf{R_I}|}}_{\text{Electron-Nucleus Interaction}} + \underbrace{\frac{1}{2}\sum_{I\neq J}\frac{Z_I Z_J}{|\mathbf{R_I}-\mathbf{R_J}|}}_{\text{Nucleus-Nucleus Interaction}} \tag{2.3}$$

2.1.2 Hohenberg-Kohn theorems

As in has been shown in Section 2.1.1, the Born-Oppenheimer approximation simplifies the Hamiltonian of the many-body problem. However, the number of degrees of freedom in the system is still too large, which makes it impossible to find its exact solutions. Nevertheless, by considering the problem using the charge density instead of the wave function containing all the information about the electrons, it becomes dramatically simplified. This is the approach taken in the Hohenberg-Kohn theorems [43]. Those theorems are formulated below:

Theorem I: "For any system of interacting particles in an external potential $V_{ext}(r)$, the potential $V_{ext}(r)$ is determined uniquely, by the ground state particle density $n_0(r)$."

Based on the Theorem 1, Eq. 2.3 can be rewritten as:

$$\widehat{H} = -\frac{1}{2}\sum_i \nabla_i^2 + \frac{1}{2}\sum_{i\neq j}\frac{1}{|r_i - r_j|} + \sum_i V_{ext}(r_i) \tag{2.4}$$

Theorem II: "The ground state energy could be expressed in terms of a universal functional of the electron density $E[n(r)]$ valid for any external potential V_{ext}. For any particular $V_{ext}(r)$, the exact ground state energy of the system is the global minimum value of this functional, and the density $n(r)$ that minimizes the functional is the exact ground state density $n_0(r)$."

Thereby, it is possible to write a universal function for the energy which contains a functional that does not depend on the external potential $V_{ext}(r)$ and only depends on the density:

$$E[n] = F[n] + \int \mathrm{d}^3\mathrm{r} V_{ext}(\mathrm{r}) n(\mathrm{r}) \tag{2.5}$$

where
$$F[n] = \underbrace{T_s[n]}_{\text{K.E.}} + \underbrace{d^3\mathrm{r} d^3\mathrm{r}' \frac{n(\mathrm{r})n(\mathrm{r}')}{|\mathrm{r}-\mathrm{r}'|}}_{\text{Hartree}} + \underbrace{E_{xc}[n(r)]}_{\text{Exchange-Correlation}} \tag{2.6}$$

F[n] is valid for any external potential $V_{ext}(r)$. All terms in Eq. 2.6 have a solution apart from the E_{xc}[n(r)] term.

2.1.3 The Kohn-Sham approach

The energy functional described above contains the term which represents a kinetic energy. Unfortunately, there is no known closed expression for calculating the exact value of this term. Hence, the functional cannot be evaluated as it stands. This problem can be solved by using the Kohn-Sham approach [44], where the difficult interacting many-body system is replaced with a solvable auxiliary non-interacting system. This is possible if assume that the ground state density of the original interacting system is equal to that of some chosen non-interacting system. Consequently, Eq. 2.3 can be represented as:

$$\widehat{H}^{\mathrm{KS}} = -\frac{1}{2}\nabla^2 + V_{ext}(\mathrm{r}) + \int d\mathrm{r}' \frac{n(\mathrm{r}')}{|\mathrm{r}-\mathrm{r}'|} + E_{xc}[n(\mathrm{r})] \tag{2.7}$$

2.1.4 Exchange-correlation functionals

The energy functional described in Section 2.1.2 also contains the exchange-correlation term E_{xc}[n(r)]. In solving the Eq. 2.7, the ground state energy and the density of the original interacting system are found with an accuracy limited by approximations utilized in the exchange-correlation functional. The exchange-correlation term can only be calculated

approximately. The most well-known approximation for E_{xc} calculation is the generalized gradient approximation (GGA). E_{xc} is presented as shown in Eq. 2.8:

$$E_{xc}^{GGA}[n(r)] = \int d\mathrm{r}\, f\big(n(r), \nabla n(\mathrm{r})\big) \tag{2.8}$$

2.1.5 Plane waves and pseudopotentials

In previous sections, approximations to the many-body Schrödinger equation have been introduced, ending in the Kohn-Sham equations. The ground state energy has been represented as a functional of the electronic density, which is calculated from the Kohn-Sham eigenstates. But to obtain the Kohn-Sham eigenstates, the exchange-correlation energy should be known. This problem can be solved by modelling the wave functions in terms of superpositions of numerical functions. In most cases, the Gaussian functions and plane waves are used to evaluate the exchange-correlation energy. The solving process is respited until a self-consistent solution is reached. The plane waves are always used together with the pseudopotentials, which aims to reduce the number of plane waves. Equation 2.9 expands the eigenstates in terms of an infinite number of plane waves with corresponding coefficients - $c_{\mathrm{K}}^{n,\mathrm{k}}$

$$\psi_{\mathrm{k}}^{n}(\mathrm{r}) = \sum_{\mathrm{K}} c_{\mathrm{K}}^{n,\mathrm{k}} e^{(\mathrm{k}+\mathrm{K}).\mathrm{r}} \tag{2.9}$$

Obviously, it is impossible to numerically evaluate an infinite number of coefficients for the basis set. Because of that, the solution is limited for K by specifying a limiting value $\mathrm{K}_{max,}$ which is the radius of a sphere in the reciprocal space whose centre is the origin.

Therefore, the limiting factor for all the K is set to $K \leq K_{max}$ and the corresponding free electron energy, the cut-off energy, can be expressed as:

$$E_{\text{cut-off}} = \frac{\hbar^2 K_{\max}^2}{2m_e} \tag{2.10}$$

where m_e is the electron mass. However, due to the fact that electronic wave functions are very steep in the close neighbourhood of the nucleus, the limitation introduced by choosing a plane wave cut-off will cause high inaccuracy. This problem can be solved by replacing the potential in the close neighbourhood of the nucleus with a pseudopotential that models the electronic wave functions properly in the interstitial region. Since most of the chemical bonding appears away from the nucleus in the interatomic region, the result of using pseudopotentials has a much lower computational cost for the same accuracy.

2.1.6 Adsorption energy and charge transfer calculations

The adsorption energy E_a is often a key quantity, in particular when the interaction between molecules and surfaces is involved. Since DFT calculations provide total energies, E_a is evaluated as a difference between the energy of the molecularly adsorbed system and the energies of the component parts. Particularly, E_a of a molecule on a surface is calculated as:

$$\Delta E_a = E_{mol+surf} - E_{surf} - E_{mol} \tag{2.11}$$

The electronic interaction between the molecules and the surface is considered by calculating the differential charge density (DCD) $\Delta\rho(r)$ defined as the difference between the

total charge density of molecularly adsorbed system subtracted by the sum of the charge densities of the isolated molecule and the naked surface.

The exact amount of transferred charge between the molecules and the surface, the plane-averaged DCD $\Delta\rho(r)$ along the normal direction (z) of the surface, is calculated by integrating $\Delta\rho(r)$ within the basal plane at the z point. The amount of transferred charge at z point is given by:

$$\Delta Q(z) = \int_{-\infty}^{z} \Delta\rho(\mathrm{z}')dz' \tag{2.12}$$

Based on the $\Delta Q(z)$ curves, the total amount of charge donated by the molecule is read at the interface between the molecule and the surface, where $\Delta\rho(r)$ shows a zero value.

2.2 Fabrication of 2D materials and heterostructures

Generally, there are two types of fabrication processes for 2D materials:

"Bottom-up" method. The bottom-up approach implies adding layers onto a substrate or growing them from smaller atomic or molecular components. Typically, there are two main methods: epitaxial growth [46, 47] and chemical vapour deposition [48]. The bottom-up approach for the graphene is schematically illustrated in Fig. 2.1(a).

"Top-down" method. The top-down approach employs exfoliation of natural or synthetic bulk material into single or few-layer nanosheets. The most commonly used methods of this approach are liquid-phase [49], electrochemical [50], and mechanical exfoliation [51]. The top-down approach for graphene is schematically shown in Fig. 2.1(b).

For the fabrication of heterostructures, the following methods are commonly used: mechanical exfoliation [52, 53], oxide powder vaporization [54] and chemical vapour deposition [55-57].

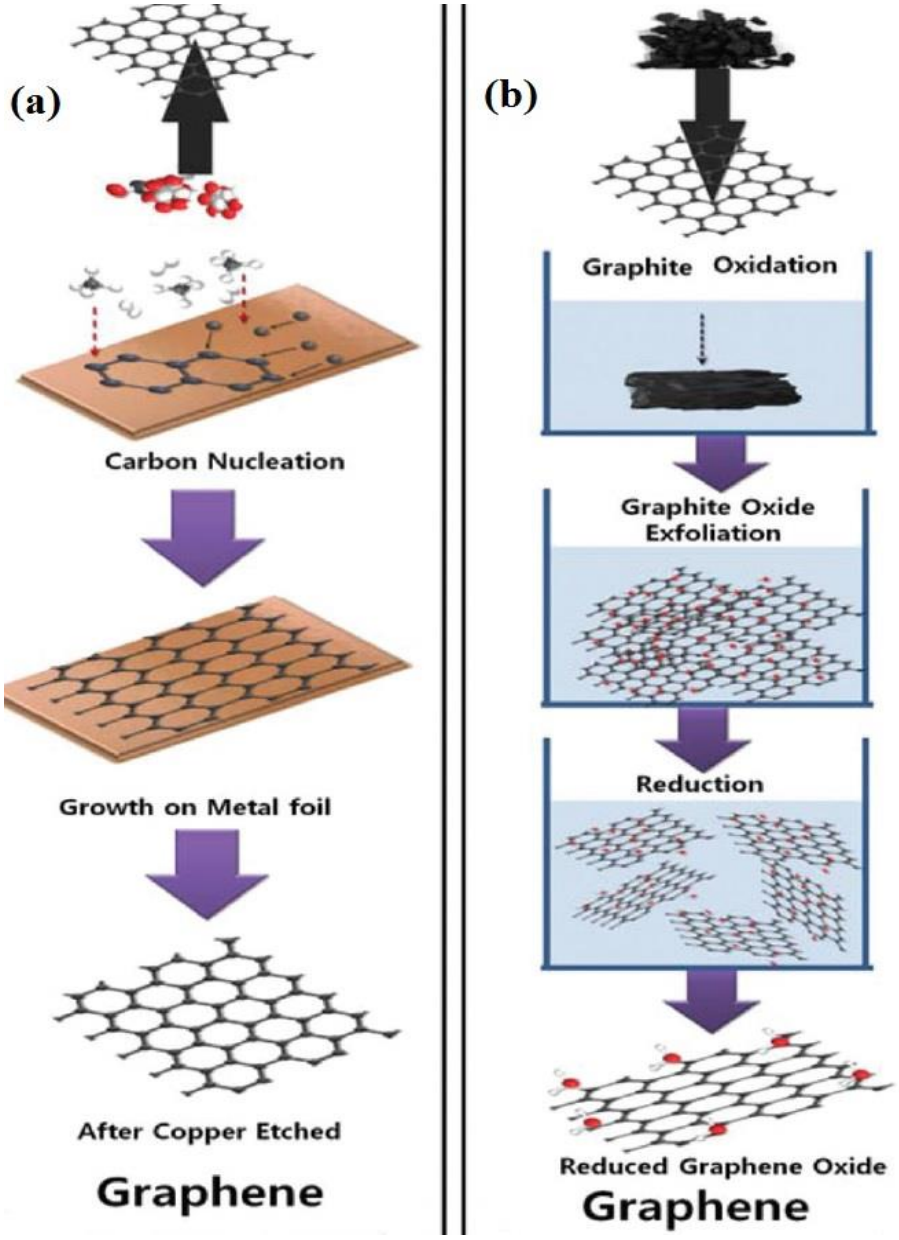

Fig. 2.1. The schematic of the graphene synthesis process: (a) "bottom-up" and (b) "top-down" approaches [58].

2.3 Exciting electronic, optical, magnetic, and mechanical properties of 2D materials and heterostructures

2.3.1 Electronic properties

The electronic performance of a material is usually characterized by the values of its carrier mobility. The remarkably high electron mobility is a distinctive feature of all the most common 2D materials.

For example, up to 20,000 $cm^2/V{\cdot}s$ of charge carrier mobility has been reported for a single layer graphene at low temperatures by Novoselov et al. [59]. In [60], Morozov et al. have reported that the electron mobility exceeds 200,000 $cm^2/V{\cdot}s$ for graphene and its bilayer at room temperature. They have also found an extremely low electron-phonon scattering rate, which sets the fundamental limit on carrier mobility at low temperature and identified defects as the dominant scattering mechanism in graphene. An enhanced carrier mobility of around 25,000 $cm^2/V{\cdot}s$ has been achieved by the improvement of sample preparation technique [61]. Further increase of graphene carrier mobility has been obtained by complete removal of the substrate. In fact, Banszerus et al. have described the fabrication of graphene-based devices with mobilities as high as 350,000 $cm^2/V{\cdot}s$ [62]. In addition, this remarkably high electron mobility in graphene has given capabilities to achieve an extraordinary quantum Hall effect [63].

No less attractive material from the point of view of carrier mobility is phosphorene. Li et al. [64] have found that the carrier mobility is thickness-dependent in phosphorene. Based on their finding, they have fabricated field-effect transistors with a thickness of 10 nm

and carrier mobility of 1,000 $cm^2/V{\cdot}s$. The theoretical study of phosphorene mobility has shown similar results. Indeed, Qiao et al. have found that the carrier mobility depends on the number of layers [65]. Their calculation predicted hole mobility to increase from 600 $cm^2/V{\cdot}s$ for a monolayer to 4000 $cm^2/V{\cdot}s$ for five layers of phosphorene. Moreover, they have found a high hole mobility of 10000-26000 $cm^2/V{\cdot}s$.

High electron mobility exceeding 103 $cm^2/V{\cdot}s$ and 104 $cm^2/V{\cdot}s$ at room and liquid-helium temperatures, respectively, has been found in atomically thin InSe, allowing the observation of the fully developed quantum Hall effect [66].

Another glowing example of 2D high mobility materials is borophene. Cheng et al. have predicted the carrier mobility in 8B-P*mmn* borophene at room temperature up to $\sim 30\times10^5$ $cm^2/V{\cdot}s$ [67]. Their result suggests that borophene is a competitor of graphene in terms of carrier mobility.

Wang and Ding [68] have shown that antimonene nanoribbons and antimonene nanosheets have moderate carrier mobility of 10^2 and 10^3 $cm^2/V{\cdot}s$, respectively. High carrier mobilities up to 4000 $cm^2/V{\cdot}s$ has been found in multilayer structure of arsenene [69].

2.3.2 Optical and magnetic properties

It is known that electrons absorb light in the ultraviolet region, invisible to the human eye. Bulk materials usually become highly transparent when thinned down to the monolayer. For example, in the visible range, graphene layer has transparency which linearly decreases with the increase of layer thickness.

In [70], it has been reported an incredible transmittance of more than 95% for 2-nm thick graphene layer and 70% for 10-nm thick films. Bae et al. [71] have theoretically found that the transparency or the light absorption is directly dependent on the number of layers of graphene. Each layer has decreased the absorption value by 2.3%. Moreover, by either cutting down graphene into nanoribbons and quantum dots or by chemical treatment with different gases methods, graphene becomes photoluminescent.

Sundaram et al. [72] have developed MoS_2 based transistors that can detect and emit visible light. Both photoluminescence and electroluminescence in a single layer MoS_2 has been observed in their work. The transparent MoS_2-graphene heterostructure has been successfully fabricated via the electrophoresis of MoS_2-graphene nanosheet nanocomposites onto a fluorinated tin oxide glass substrate [73].

The first-principles investigations of the optical absorbance of graphene, silicene and germanene have been performed by Matthes et al. [74]. They have found a blueshift of the optical absorption peaks coming from the quasiparticle corrections. Moreover, the low-frequency absorbance has been modified due to spin-orbit transparency edge, resulting in an increase of absorbance in the fundamental absorption region.

Matte et al. [75] have studied the magnetic properties of different graphene samples. They have shown the dominance of both ferromagnetic and antiferromagnetic interactions. Furthermore, all the graphene samples used in the experiment have magnetic hysteresis at room temperature. They have also found that the magnetic properties strongly depend on the thicknesses and the number of layers of graphene, the reported magnetization increases with the decrease of thicknesses or/and layer number.

Magnetic properties of MoS_2 have been experimentally investigated by Tongay et al. [76]. They have found a temperature dependent diamagnetic background when cooling down from 300 to 10K, and ferromagnetism which comes from zigzag edges with associated magnetism at grain boundaries.

2.3.3 Mechanical properties

The 2D materials, such as graphene, MoS_2, phosphorene etc., are generally distinguished by their unique strength and flexibility along with the high Young's modulus. One of the first experimental investigations on the mechanical properties of graphene has been done by Lee et al. [77]. They have patterned an array of circular wells onto a substrate by nanoimprint lithography and reactive ion etching. Then the graphite flakes have been mechanically deposited onto the substrate and loaded by a tip of atomic force microscope. According to their results, graphene shows non-linear elastic behaviour and brittle fracture. Moreover, the value of Young's modulus of 1.0 TPa, the third-order elastic stiffness of -2.0 TPa and a critical stress of brittle fracture of graphene of 130 GPa are the highest ever measured for real materials.

In the framework of the DFT, the phonon spectra of graphene as a function of uniaxial tension have been studied by Liu and co-authors [78]. They have found a Young's modulus of 1.05 TPa and an intrinsic strength of 110 GPa. Furthermore, they have predicted an innate tendency to brittle fracture of graphene at room temperature due to the soft phonons longitudinal elastic wave nature. The mechanical properties of pristine graphene discussed above are consistent with the results of experimental investigations [77].

Castellanos-Gomez et al. have aimed to investigate the mechanical properties of MoS_2. In their experimental study [79], freely suspended MoS_2 nanosheets with thicknesses of up to five layers have been bent with a tip of atomic force microscope. They have observed an unusually high Young's modulus of 0.33 TPa and an extraordinary toughness, capable to withstand elastic deformations up to tens of nanometres. In accordance with its high Young's modulus and elasticity, they also suggest that MoS_2 is an attractive substitute or alternative for graphene.

These previous results are well consistent with the results for MoS_2 achieved by Kis and co-workers [80]. They have developed their own measurement method, where the elastically deforming beam firmly held on each end while the normal force is applied by using an atomic force microscope. Experimental measurements have shown Young's modulus of 120 GPa and an approximate value of the inter-tube shear modulus of 160 MPa.

Jiang and Park [81] have examined the mechanical properties of graphene-MoS_2-graphene heterostructure, by using molecular dynamics simulations. They have shown that the interface spontaneous strain energy arises due to the lattice mismatch between graphene and MoS_2. For their fabricated heterostructure, the value of Young's modulus has been found three times larger than that of MoS_2. However, the yield strain of their heterostructure has been found at around 70% of that for MoS_2.

Later, Jiang and Park have performed the first-principles calculations on the mechanical properties of phosphorene [82]. They have found a highly anisotropic and nonlinear Young's modulus due to phosphorene puckered structure. For in-plane direction perpendicular to the pucker, the Young's modulus has been found three times smaller than in the parallel direction, 41.3 GPa and 106.4 GPa, respectively.

Mechanical flexibility of phosphorene has been investigated in the framework of the DFT by Wei and Peng [83]. They have reported a superior strength of 18 GPa in the zigzag and 8 GPa in the armchair directions, and the critical strain up to 30%. Moreover, their calculations have also proved a high anisotropy of the mechanical properties of phosphorene. Specifically, the Young's modulus in the zigzag direction is about 4 times larger than in the armchair direction, 166 GPa and 44 GPa, respectively.

Another interesting mechanical property of phosphorene is its Poisson's ratio. Jiang and Park et al. in their first-principles calculations [84] have shown a negative Poisson's ratio of a single-layer phosphorene which comes from its puckered structure. They have also marked anisotropy of Poisson's ratio which is strongly negative only in the out-of-plane direction under uniaxial deformation in the direction parallel to the pucker.

2.4 The effect of various factors on the properties of 2D materials and heterostructures

It is known that the structural, electronic, optical, magnetic, and thermal properties of 2D materials can be tuned by defect and strain engineering [85-95], electric field [96-98] and adatom adsorption [99-106]. For this reason, many studies have been performed to investigate the effect of these factors on the various properties of 2D materials.

2.4.1 Strain engineering

The investigation of strain engineering effect is one of the most exciting issues of all the research on the properties of 2D materials. For example, Choi et al. [85] have investigated

the influence of uniaxial strain on the band gap of graphene. The semi-metallic behaviour of graphene has been reported for up to 30% of applied strain along the armchair direction, similarly, no sizable band gap has been found for the strain less than 26.2% along the zigzag direction [85]. Interestingly, an insignificant band gap of 45.5 meV has been established for the strain value of 26.5%, however, it is rapidly closed with strain increased. In addition, those authors have also demonstrated anisotropy of the Fermi velocity, which quickly decreases and vanishes parallel to the strain direction, while it greatly increases in the perpendicular direction. Semi-metallic nature of graphene under the small strains has been demonstrated by Mohr et al in [86], where the authors have used the first-principales calculations for analysis of the electronic properties of strained graphene.

In the theoretical analysis [87], Pereira and Neto have considered the tensional strain effect on the band structure of graphene. They have shown zero band gap of graphene under the strain less than 20%; the tensional strain 20% and higher leads to band gap opening. Furthermore, these authors have linked the band gap opening to the integration of two Dirac points, which causes the anisotropy of Fermi surface and Fermi velocities in graphene.

The effect of large localized strain on the band structure of atomically thin MoS_2 has been studied in both experimental and theoretical ways [88]. There, Castellanos-Gomez et al. have carried out scanning photoluminescence measurements on the wrinkled samples and developed their own tight-binding model in addition to the experiment. They have found direct-indirect band gap transition and funnelling of photo generated excitons under the strain ranged from 0.2 to 2.5%. Experimental and theoretical results have demonstrated a good agreement and presented a unique technique to local strain engineering for all atomically thin materials.

Pan and Zhang have investigated the effect of strain on the electronic and magnetic properties of MoS_2 nanoribbons via first-principles calculations [89]. They have found that MoS_2 nanoribbons are highly flexible. Moreover, their calculations have predicted a band structure change with the strain, specifically, in the armchair direction, due to the shift of the energy states near the Fermi level; band gap changed from a direct one under the slight tensile strain to indirect one under the large strain up to 10%. The applied strain of 10% along the zigzag direction leads to an increase in the magnetic moments by 2 times.

Extensive experimental research on the ways to control the optical and phonon properties of the MoS_2 layers has been performed by Hui et al. [90]. They have demonstrated an electro-mechanical device capable of applying a uniform and controllable biaxial compressive strain of 0.2% together with photoluminescence and Raman detections. In their experiment, piezoelectric substrates for the strain application and graphene layer as a top electrode transparent for the photoluminescence have been used. The experiment has shown a blueshift of MoS_2 direct band gap for 300 meV per 1% strain and the photoluminescence intensity increase of 200%. Moreover, a high tunability and controllability of MoS_2 band gap by strain have also been demonstrated.

Another perspective material for strain engineering, which is presently attracting a great deal of interest, is phosphorene. For example, Peng et al. [91] have studied the effect of strain on the phosphorene electronic structure via first-principles calculation in the frameworks of the DFT and hybrid functionals. They have evaluated five special zones in the electronic band structure, each constrained by its own critical strain in a range from 11.3 to −10.2% strains. Furthermore, they have shown that a considerable in-plane strain causes a

direct-indirect band gap transition in phosphorene. In addition, they also observed strongly anisotropic transport of carriers, which can be dramatically changed by strain.

In [92], first-principles calculations together with the non-equilibrium Green's function method have been used to investigate the thermal transportation of phosphorene. In their work, Ong et al. have observed significant anisotropy in thermal conductance of phosphorene at room temperature. Along zigzag direction, the found conductivity is 40% higher than that along armchair direction. They have also found that the thermal conductance along zigzag direction increases under the zigzag applied strain and decreases for the armchair applied strain, while the thermal conductivity along the armchair direction decreases in both these cases. These results suggest phosphorene as a material with the high and strain-controlled thermal transport anisotropy.

Kou et al. [9] have examined a shallow ripple deformation in phosphorene induced by up to 10% compressive strain by first-principles calculations. They have found that the ripple deformation is anisotropic, and it occurs only along the zigzag direction, but not along the armchair direction. These authors have postulated that this is due to the phosphorene puckered structure with coupled "hinge" bonding configurations. In addition, in the framework of classical elasticity theory, an analytical model for the mechanisms of changes in the structural and electronic properties in phosphorene has been presented [9].

The mechanical and electronic properties of silicene subjected to strain have been studied. For example, Qin et al. [93] have shown that strain is able to cause a semi-metal to metal transition in silicene. The semimetal state is typical for the biaxial strain of 7% or less; while for the strain higher than 7%, silicene undergoes a semimetal to metal transition. They

have also found that the work function, which is well tunable with a strain, increases for small strain values and then becomes nearly unchanged for the high strain values.

All the above listed features suggest that strain engineering is a very promising method to tune the mechanical, electronical and thermal properties of 2D materials.

2.4.2 Electric field effects

Electric field engineering is also an effective way to control and modify band structure, electronic and thermal conductivities of the 2D materials and heterostructures. For example, Castro et al. [96], both experimentally and theoretically, have investigated the influence of the electric field on the band structure of graphene. They have found that the band gap can be changed extensively from zero to mid-infrared energies.

A novel way to apply an external electric field on the ripple of the membrane of MoS_2 with the aim to control the band gap has been proposed [97]. There, Qi et al. via first-principles calculations have shown a great tunability of band structure of MoS_2 under the surface-perpendicular electric field and have also explained its nature on the basis of the charge density redistribution.

In another work [98], density functional theory has been used to find out the effect of the vertical electric field on the electronic properties of bilayer MoS_2. Liu et al. have found the band gap reduction, down to zero, during the monotonic increment of the electric field. Their *ab initio* quantum transport simulations of a dual-gated bilayer MoS_2 channel have also confirmed the feasibility of applying the electric field to manipulate the transmission gap.

In addition, first-principles studies [99, 100] have presented the band gap extension via vertical electric field engineering in silicene, germanene, and phosphorene. The effective carrier mass and the band gap rise linearly with increasing the electric field in silicene and germanene, while the phosphorene undergoes a transition from the normal insulator to a metal.

2.4.3 Effects of adatom adsorption and atomic point defects

Adsorption of different atoms and molecules, as well as, the presence of atomic defects can drastically change the properties of 2D materials. For instance, by using first-principles calculations, Zhou et al. have shown that the graphene magnetic and electronic properties can be significantly changed by Cl, S, and P atomics adsorption [101]. They have found that the Fermi level shifts to valence band upon Cl adsorption, and as a result, metallic states exist, while the S atom adsorption on graphene leads to the band gap of 0.6 eV opening. They have also reported the lack of the magnetic moment upon either Cl or S adsorptions, but for the P-absorbed graphene, the magnetic moment of 0.86μB appears. Thereby, this work suggests the atom adsorption as a perspective way for modifying the magnetic properties and conductive behaviour of graphene.

The effect of metal adatom adsorption on graphene has been investigated by Chan et al. [102]. In the framework of the DFT, they have analysed adsorption energy, stability, the density of states, dipole moment and the work function of adatoms-absorbed graphene. Absorption of metal adatoms which belong to the groups I-III of the Periodic Table is able to entail just minor changes in the electronic states, but the charge transfer can be enhanced significantly, as well as a work function can be greatly shifted. Furthermore, the authors have

shown that the adsorption of the transition, noble, and group IV metal adatoms leads to the strong hybridization between adatom and graphene electronic states.

A systematic study on the absorption of the small gas molecules on the either pristine and doped or defect-containing graphene has been done by Zhang et al. [103]. Their *ab initio* calculations have predicted that the structural and electronic properties of the molecule-adsorbed graphene have a strong dependence on the initial graphene structure and the molecular configuration. All the considered molecules (CO, NO, NO_2 and NH_3) have shown a strong adsorption on the doped or defective graphene, while on the pristine graphene, molecules have been physisorbed with the small adsorption energies and a weak charge transfer. In addition, the authors have also found dramatic changes in the electronic properties of graphene. Specifically, B-doped graphene has a two times higher sensitivity of transport behaviour than that of the pristine one. Thereby, the gas sensitivity of graphene can be significantly improved by molecular doping or defect.

He et al. [104] have examined MoS_2 monolayer for the non-metal adatom absorption. Their first-principles calculations have demonstrated the possibility of the chemical absorption of H, N, B, O, F, and C atoms on the monolayer. Moreover, they have also observed no magnetic moment in the O-absorbed MoS_2 and the magnetic moment of 1.0, 1.0, 2.0, 1.0, and 1.0μ_B in the H, N, B, F, and C -absorbed MoS_2, respectively. In addition, an extension of spin density, as well as, *n*-type semiconducting behaviour in the H-absorbed MoS_2 and *p*-type behaviour in the N-absorbed MoS_2 monolayer has been found.

Sivek et al. have used *ab initio* calculations to study the structural, magnetic and electronic properties of silicene upon chemical absorption of B, P, N, and Al atoms [105]. They have reported the strong bond between adsorbates and silicene along with the metallic

behaviour of adsorbed-silicene. Moreover, B, N, and P adatoms have been found as strong acceptors, with *p*-type doping of silicene, while Al adatoms have a weak charge transfer to silicene. Additionally, the authors have provided molecular dynamics simulation to demonstrate the stability of adsorbed-silicene at the temperature of 500 K. According to their obtained results, silicene is suggested as a highly sensitive and well modifiable material.

The interaction of phosphorene with organic molecules has been considered in the framework of the DFT by Jing et al. [106]. They have shown a strong bonding between tetracyanoquinodimethane (TCNQ), tetracyanoethylene (TCNE) and tetrathiafulvalene (TTF) molecules and the phosphorene surface along with a large amount of charge transfer between them. As a result, doping by the organic molecules could remarkably decrease the band gap of the mono- and bilayer phosphorene. Furthermore, the comparison of the optical properties of the pure phosphorene with the molecule-absorbed one has revealed substantial enhancement of the light harvesting abilities of phosphorene.

Wang et al. have studied the effect of vacancy and self-interstitial P-defects in phosphorene. Their calculations, based on the hybrid DFT including the van der Waals correlation functional, have shown that both defects exhibit a weak acceptor behaviour, which is consistent with the experimental observation of the *p*-type conductivity in few-layer phosphorene [8]. They have also found the correlation between formation energies and transition levels and phosphorene film thickness. Specifically, the thickness increase induces the formation energies and transition levels decrease, which is the cause of *p*-type conductivity in few-layer phosphorene.

2.5 Application of 2D materials and heterostructures

The 2D materials and heterostructures have a wide range of use, for example, in the fundamental research, electronic and opto-electronic devices, and gas sensing application.

2.5.1 Fundamental research

A large amount of research effort has been directed to find new 2D materials and to deeply understand their interesting properties, such as ferromagnetism, superconductivity, phase transitions, light-matter interaction etc. [107-113].

2.5.2 Electronic and opto-electronic devices

Due to their high electrical conductivity, excellent transparency, strong electron acceptance property, tunable band gap and flexibility, 2D materials have been actively investigated for application in solar cells and photodetectors [114-116], pressure sensors [117-120], high-density storage devices [121-133] and others [134-138]. The basic requirement for solar energy devices is their capabilities for commercial application, in other words, their high-cost effectiveness.

Lin et al. through their theoretical simulation and experimental investigation [114] have demonstrated a highly efficient graphene-semiconductor heterojunction solar cell. Based on their theoretical analysis, the authors proposed the following optimization: (I) the number of graphene layer should be precisely selected; (II) antireflection layers should be introduced to avoid the energy dissipation from the optical reflection. They have considered a periodically patterned surface to reduce the reflectance. The theoretical conversion efficiency of their optimization achieved 9.2%. To verify this result in practice, they manufactured and

examined solar cells based on acid modified graphene films and silicon pillar arrays, with the efficiency of around 7.7%. In addition, the authors noted that the cell performance can be further improved up to the theoretically obtained maximum value.

In [115], Tsai et al. by using ultraviolet photoemission spectroscopy successfully confirmed the possibility to create a type-II heterojunction between monolayer MoS_2 and *p*-Si. They have reported the fabrication of a heterojunction solar cell device with a fabulous power efficiency of 5.23%. Their experiment has shown that MoS_2 can be fully integrated into the manufacturing process and demonstrated that different 2D materials can be applied in solar cell devices.

In the pioneer experimental work [116], Deng et al. for the first time have demonstrated a 2D heterostructure using black phosphorus. They have presented phosphorene-MoS_2 heterojunction *p-n* diode, which shows a hundred times larger photodetection responsivity than that of black phosphorus phototransistors and around thirty times larger than that of WSe_2 *p-n* diodes. Moreover, they have shown that the current is generated throughout the total overlapped *p-n* junction region, and consequently, it is feasible to use their diode in photodetectors and solar cells.

Another promising field for graphene-based material application is micro-electro-mechanical systems (MEMS) [117], where the extraordinary stiffness of graphene with Young's modulus of 1 TPa [77], high electrical conductivity, excellent flexibility, and stretch ability can be used. Since the resistivity of graphene varies linearly with strain [48], this piezoresistive effect can be widely used in MEMS smart sensors, including pressure sensors.

In [118], Bae et al. have demonstrated a strain sensor capable to track a body motion. They have used a traditional micro-fabrication process and ultrathin, flexible plastic or

stretchable rubber as substrates to fabricate graphene-based sensor in a form of the rosette. As a part of their experiment, the electrical resistance related to the applied strain was measured. They have specified three different regions: (I) when applied strain is ≤ 1.8%, an approximately linear function resistance/strain has been observed with the gauge factor of ≈2.4; (II) a nonlinear function for the strain is in the range from 1.8% to 7.1% with the gauge factor ranging from 4 to 14; and (III) the strain values ≥ 7.1% corresponding to the sharp growth of the resistance, and, as a consequence, to a mechanical fracture. Their sensor achieved a good transparency up to 80% and an impressive gauge factor, comparable to that in a metallic strain gauge. This study has successfully demonstrated the possibility to create graphene-based highly sensitive transparent strain sensors for detection of the direction and amplitude of motion.

Sorkin and Zhang [120] have studied the mechanical failure of graphene-based pressure sensors. Their pressure sensor model consisted of a circular graphene nanoflake placed on the substrate; the inner part of the graphene nanoflake was suspended, while the outer part was supported by the underlying substrate. The authors applied an atomistic approach to investigate the failure behaviour of the sensor subjected to an external load. They have identified two types of mechanical failure. The first one was due to the full detachment of the graphene flake from the supporting substrate. The second type of failure happened because the atomic bonds broke within the graphene flake. They have found the following regularity: if the width of clamped region was smaller than a critical value, then destruction occurred due to graphene detachment, while graphene fracture typically for the width of the clamped region was higher than the critical value. Their investigation provided valuable

information about the design and fabrication of graphene nanoflakes strain sensors for potential application.

Because of their large surface area, excellent thermal and electrical conductivity and chemical stability, 2D materials and its heterostructures are being actively investigated and successfully used to develop high-density storage devices, such as supercapacitors [121-127].

Graphene-based supercapacitor, prepared using the gas-based hydrazine reductions, has been fabricated by Wang et al. [121]. Their supercapacitor has shown a high specific capacitance of 205 F/g, the energy density of 28.5 Wh/kg and power density of 10 kW/kg. In [122], Cao et al. have developed a high voltage asymmetric supercapacitor with 1 M Na_2SO_4 aqueous electrolyte by using amorphous MnO_2 nanoparticles and graphene as positive and negative electrode materials, respectively. They have achieved a specific capacitance of 37 F/g at a discharge current density of 5 mA/cm^2 and an energy density of 25.2 Wh/kg at a power density of 100 W/kg. The obtained asymmetric system also exhibits impressive capacitance retention of 96% after 500 cycles.

Xie et al. have presented a supercapacitor with wavy-shaped polyaniline-graphene electrode with a maximum specific capacitance of 261 F/g and an energy density of 23.2 Wh/kg at a power density of 399 W/kg for a 0.8 V voltage window [123]. Their tests have shown capacitance retention of 89% over 1000 cycles in conjunction with a high mechanical strength even under the strain of 30%.

MoS_2-based micro-supercapacitors have been created by Cao et al. [124]. Via spray painting of MoS_2 nanosheets on Si/SiO_2 chip and subsequent laser patterning, they have created micro-supercapacitors with a high current density (2.2 mA/cm^2) and excellent cyclic performance at around of 92% capacitance during 1000 cycles. These results surpassed any

previous results that have ever been found. Subsequently, Choudhary et al. have fabricated a large-scale flexible and high-capacitance MoS_2 supercapacitor electrodes with the excellent capacitance retention of ~97% and cyclic stability up to 5000 cycles [125].

Huang and co-workers have succeeded in synthesizing layered MoS_2-graphene composites [126]. They have reported a specific capacitance of 243 F/g at a discharge current density 1 A/g for the composite compared to 120 and 35 F/g for pure MoS_2 and graphene, respectively. Moreover, they have achieved suitable capacitance retention above 92% even after 1000 cycles.

Composite membranes made of an exfoliated dispersion solution of semiconducting MoS_2 and semi-metallic graphene have been demonstrated by Bissett et al. [127]. They have found the optimal layer number ratio of the MoS_2 and graphene is 1:3. At this ratio, the composite membrane has shown a high specific capacitance of 11 mF/cm^2. Moreover, they have found that continued charge/discharge cycles lead to an increase in the membrane efficiency of ~800%.

2D materials are also promising candidates for anode materials for rechargeable batteries, such as lithium [128-137] and sodium ion-batteries [140]. The main shortcoming of lithium-ion batteries is the interfacial reaction with Li^+ ions that have a negative effect on cycling capability. Therefore, a lot of research aims to find out better interfacial layer materials.

For example, Xia et al. have examined graphene as an interfacial layer in lithium-ion battery anode based on silicon nanowires [128]. Their experiment has shown that the cycling stability of the silicon-graphene anode can be significantly improved in comparison with a

pure silicon-based anode. Particularly, the obtained specific charge capacity of ~2400 mAh/g has exceeded the value of the silicon-based anode by more than 170%.

The theoretical study on potential applications of phosphorene as a material for the lithium-ion batteries has been conducted by Zhao and co-authors [129]. Their first-principles calculations have shown a semiconductor to metal transition for phosphorene upon lithiation, which could provide additional electrical conductivity. Moreover, their calculated theoretical capacity of 432.79 and 324.59 mAh/g for mono- and bilayer phosphorene, respectively, exceeds the capacity of commercial anodes used in lithium-ion batteries.

Interesting results have been obtained by Guo et al. in their systematic first-principles study of the phosphorene-graphene heterostructure as anode material for lithium-ion batteries [130]. They have reported a high binding energy of Li on the phosphorene-graphene heterostructure compared to the pristine phosphorene or graphene, 2.6 eV compared to 1.9 and 1.3 eV, respectively. Furthermore, their calculations have shown extraordinary ultrahigh stiffness of phosphorene-graphene heterostructure which is more than 10 times higher along the armchair direction and more than 4 times higher along the zigzag direction, compared to pristine phosphorene and graphene. The capacity of heterostructure has also surpassed the capacity of its individual components. Therefore, phosphorene-graphene heterostructure is a promising material for the lithium-ion batteries application.

2.5.3 Gas sensing

Along with many other attractive properties, 2D materials exhibit a high chemical activity that makes them promising candidates for gas sensing application [139-145]. The

main challenge for all the gas sensors is a low level of sensitivity. The reason for this is thermal fluctuations since the intrinsic noise may exceed the signal from individual atom or molecules by many orders [139]. However, Schedin et al. have invented a micrometre-size gas sensor made of graphene which can detect the interaction of an individual gas molecule with the graphene surface [140]. Their research has provided a wide range of opportunities for studying 2D materials for gas sensor application.

Motivated by the previous work, Leenaerts et al. have conducted a theoretical investigation of the adsorption of different gas molecules on the graphene surface by using first-principles calculations [141]. They have investigated the charge transfer between graphene and the molecules to determine the nature of molecular doping mechanism. The H_2O and NO_2 molecules have shown acceptor behaviour, while NH_3, CO, and NO are donors. These results are well consistent with the experiment data [142]. In addition, the exact orientation on the surface and preferential binding site of molecules have also been identified by calculating their binding energy. Thereby, their study has presented an interesting mechanism for future gas sensors.

Kou et al. [143] have systematically investigated the adsorption of gas molecules like CO, CO_2, NH_3, NO, and NO_2 on monolayer phosphorene via first-principles calculations. Due to significant changes of the charge transfer and electronic band structure, induced by the adsorption of NO and NO_2 molecules, a high sensitivity of phosphorene to these toxic gas molecules has been predicted. They have also shown that the current reduces upon NH_3 molecule absorption but increases upon NO absorption. These changes in conductivity of phosphorene have been strictly anisotropic along both armchair and zigzag directions. Consistent results have been presented in [13], where the physisorption of CO, O_2, NO, NO_2,

H_2O, NH_3, and H_2, molecules has been investigated via first-principles calculations. Their study has shown significant changes in the electronic properties of phosphorene through the physisorption of foreign molecules. For example, it has been shown that H_2O, NH_3, CO, and H_2 molecules are weak donors, while NO, NO_2, and O_2 are strong acceptors. Moreover, a strong binding energy and a distinct charge transfer have been found between NO_2, NO, and O_2 molecules and phosphorene. Based on the foregoing, the authors have suggested phosphorene as a promising material for molecular sensor applications.

2.6 Summary

The effects of strain and defect engineering, edge functionalization, electric field engineering, and adatom adsorption on the stability, opto-electronic, and magnetic properties of 2D materials have been briefly reviewed. The commonly used experimental and theoretical approaches for the investigations of 2D materials properties have been outlined. The first-principles simulation approach has been adopted, and the fundamentals of this approach have been discussed.

Chapter 3 The effects of strain and vacancy defects on stability and electronic properties of phosphorene

A detailed study of the strain and vacancy defects on the atomic structure evolution and changes in electronic properties of phosphorene is performed. In addition, the effects of strain and vacancy defects on the chemical activity of phosphorene upon the adsorption of typical environmental molecules H_2O, O_2, and NO are comprehensively examined.

3.1 Computational details

The research methodology is based on the spin-polarized first-principles calculations by using the plane-wave Vienna *ab initio* simulation package (VASP) [26] within the framework of DFT. The exchange-correlation functionals are selected as the PBE functional under the GGA [31]. Dispersive interactions during the noncovalent chemical functionalization of phosphorene with small molecules are analyzed using the van der Waals corrected functional with Becke88 optimization [30]. All the structures are fully relaxed until the force is smaller than 0.01 eV/Å.

Rippled structures are created by using the 10×1×1 and 1×10×1 supercells (40 phosphorus atoms) for applying strain along the zigzag and armchair directions, respectively. A 10×3×1 supercell is adopted for single NO adsorption. The first Brillouin zone is sampled with a 1×10×1 (10×1×1) k-mesh grid for the 10×1×1 (1×10×1) supercell and 1×3×1 grid for the 10×3×1 supercell. Different supercells are adopted for modelling the rippled structures along the zigzag and armchair directions. For the supercell initially in the planar configuration, a period of ripple is formed upon applying a period of sinusoidal out-of-plane

displacements to the atoms along the zigzag or armchairs directions, followed by an energy minimization by using VASP. The length of the ripple corresponds to the wavelength of the sinusoidally shaped phosphorene along the zigzag (or armchair) direction, the wavelength is shown in Fig. 3.1. Since periodical boundary condition with a fixed period is applied laterally, that is, along the armchair (or zigzag) direction, the lattice spacing along the armchair (zigzag) direction remains unchanged. It is noted that the studied compressive strain has large out-of-plane component and should be considered as effective strain.

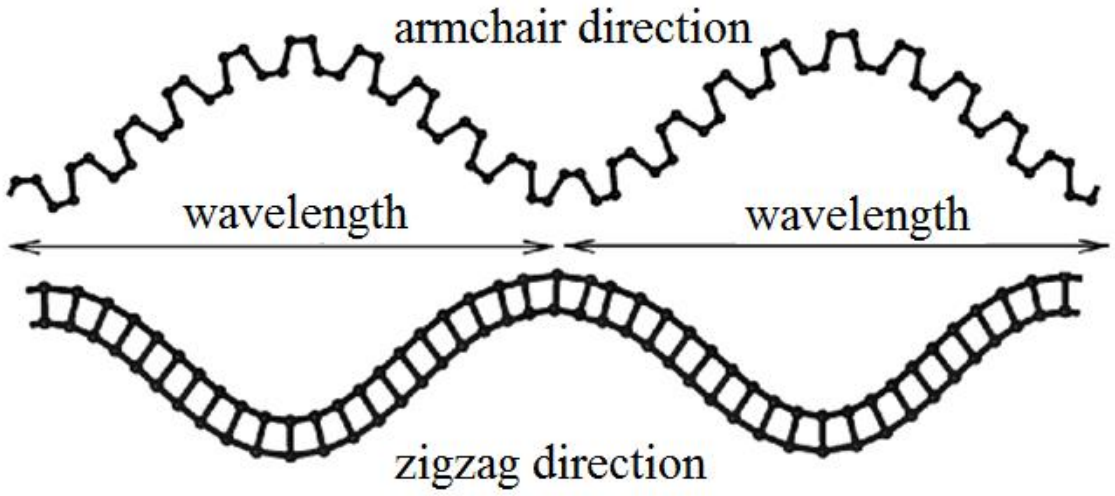

Fig. 3.1. The schematic representation of the ripple length, defined as the wavelength of the sinusoidally shaped phosphorene along the zigzag or armchair directions.

The effects of mono- (MV) and divacancy (DV) defects in phosphorene are considered by removing one or two phosphorus atoms in a 4×5×1 supercell (80 phosphorus atoms) as it is shown in Figs. 3.2(a) and (b), respectively. The first Brillouin zone is sampled with a 10×10×1 k-mesh grid. Periodic boundary conditions are applied in the two in-plane

transverse directions, while a vacuum space of 20 Å is applied along the out-of-plane direction. Kinetic energy cut-off is set to 450 eV. The absorption energy E_a of a molecule on rippled phosphorene is calculated as

$$E_a = E_{Mol+P} - E_P - E_{Mol} \tag{3.1}$$

where E_{Mol+P}, E_P, and E_{Mol} are the energies of molecule adsorbed phosphorene, the phosphorene sheet, and the single molecule, respectively.

The electronic interaction between the H_2O and O_2 molecules with phosphorene is calculated by the differential charge density (DCD) $\Delta\rho(r)$, defined as the difference between the total charge density of molecularly adsorbed phosphorene system subtracted by the sum of the charge densities of the isolated molecule and the naked phosphorene. To obtain the exact amount of transferred charge from the H_2O or O_2 molecule, the plane-averaged DCD $\Delta\rho(r)$ along the normal direction (z) of the phosphorene sheet is calculated by integrating $\Delta\rho(r)$ within the basal plane at the z point. The amount of transferred charge at z point is given by

$$\Delta Q(z) = \int_{-\infty}^{z} \Delta\rho(z')dz'. \tag{3.2}$$

Based on the $\Delta Q(z)$ curves, the total amount of charge donated by the molecule is read at the interface between the molecule and the phosphorene, where $\Delta\rho(r)$ shows a zero value. The reaction barriers are calculated by using the climbing image nudged elastic band (CI-NEB) method [146].

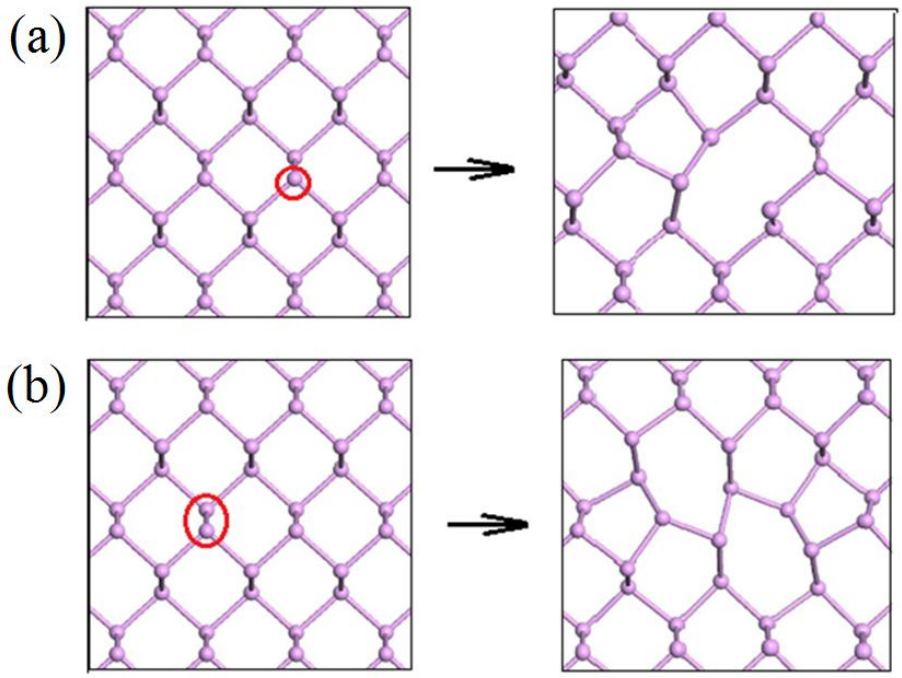

Fig. 3.2. The phosphorene structure containing (a) MV and (b) DV, obtained by removing one and two phosphorus atoms in a supercell of 4×5×1 dimension, respectively.

3.2 Results and discussion

3.2.1 Structure and electronic properties of phosphorene under compressive strain

Fig. 3.3(a)-(e) presents the relaxed rippled structure (upper panel) and the variation of band gap (lower panel) of monolayer phosphorene under compressive strain of 0%, -5%, -20%, -25%, and -35%, respectively, along the armchair direction. It is seen that the phosphorene remains a direct band gap semiconductor within the strain range. For the compressive strain in the range from 0% to -20%, the band gap decreases from 0.84 eV to 0.51 eV. The calculated results for the strain range from 0% to -10% are in good agreement

with previous results [9]. For the compressive strain higher than -20%, the band gap achieves approximately a constant value at about 0.51-0.54 eV.

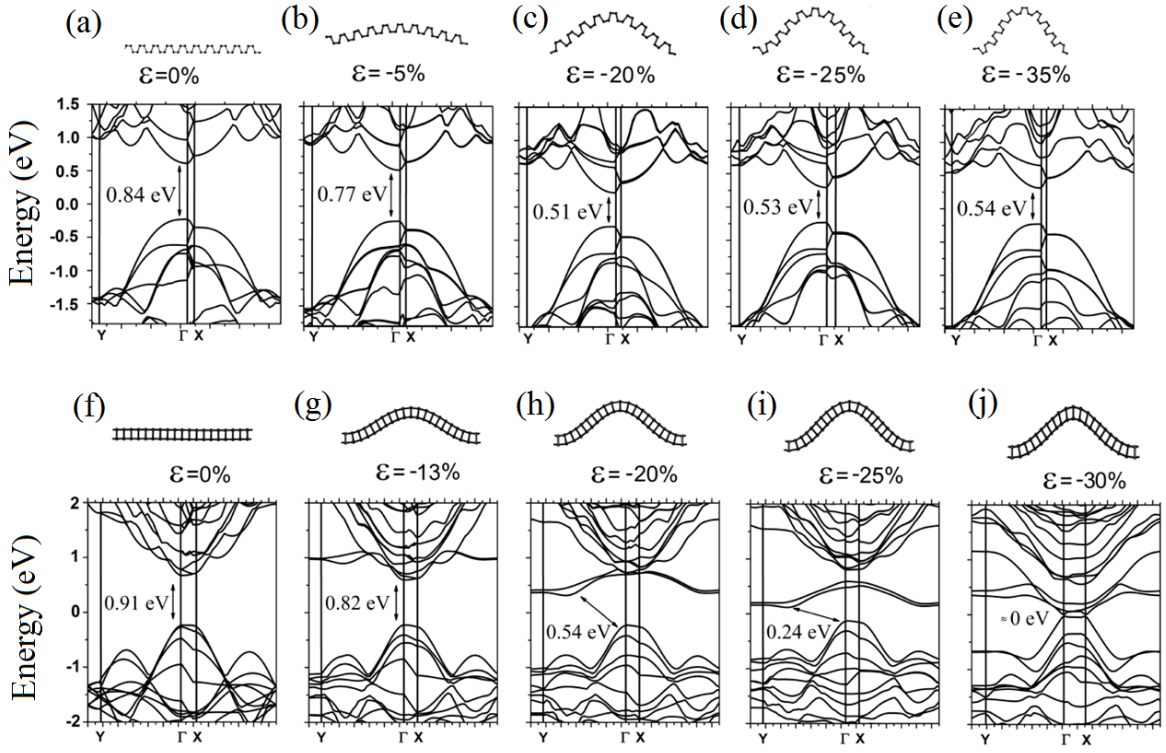

Fig. 3.3. The relaxed structure and variation of band gap of monolayer phosphorene under a compressive strain applied along the armchair direction (a)-(e) and the zigzag direction (f)-(j). The applied strain is (a) 0%, (b) -5%, (c) -20%, (d) -25%, and (e) -35%, (f) 0%, (g) -13%, (h) -20%, (i) -25%, and (j) -30%.

Figs. 3.3(f)-(j) presents the relaxed rippled structure (upper panel) and the variation of band gap (lower panel) of monolayer phosphorene under compressive strain of 0%, -13%, -20%, -25%, and -30%, respectively, along the zigzag direction. It is seen that the band gap decreases rapidly from 0.91 eV to 0 eV as the compressive strain increases from 0% to -30%. Meanwhile, the conduction band minimum (CBM) shifts from Γ to a point between the Γ

and Y points (Figs. 3.3(h) and (i)), indicating a direct-to-indirect band gap transition. Moreover, at -30% compressive strain and higher, the band gap disappears completely (Fig.3.3 (j)), signifying a semiconductor-to-metal transition. Hence, it is possible to switch phosphorene from a direct band gap semiconductor to an indirect semiconductor and further to a metal simply by applying the compression strain along the zigzag direction.

To understand the underlying physical origins for the band gap variation, the structural deformation of the rippled phosphorene is investigated by examining the ripple-induced bonding configuration changes. For both zigzag and armchair directions, the variation of bonding configurations of the unit cell on the top peak of the rippled structure is tracked as shown in Figs. 3.4(b) and (c), respectively. The justification for choosing these unit cells is that only the atoms in these unit cells have significant contributions to the valence band maximum (VBM) and CBM. As defined in Fig. 3.4(a), the following parameters during compression deformation are tracked: the bond length connecting the hinges l_1, the bond length of the hinges l_2 and l_3, and the hinge angles α and γ. The calculated relative variations of the bond lengths, that is, $\Delta l_1 = (l_1-l_1^0)/l_1^0$, $\Delta l_2 = (l_2-l_2^0)/l_2^0$, $\Delta l_3 = (l_3-l_3^0)/l_3^0$, and the angle difference (α-γ) are presented in Figs. 3.5(b) and (c), respectively.

For the compressive strain along the armchair direction, it is seen that with increasing the strain from 0 to -10%, the relative variations of the bond lengths Δl_1, Δl_2, and Δl_3 decrease, while the angle difference (α-γ) is roughly unchanged. For the compressive strain from -10% to -20%, the bond lengths l_1 and l_2 slightly increase, while l_3 slightly decreases, and the angle difference (α-γ) slightly increases. For the compressive strain higher than -20%, all the parameters remain roughly unchanged.

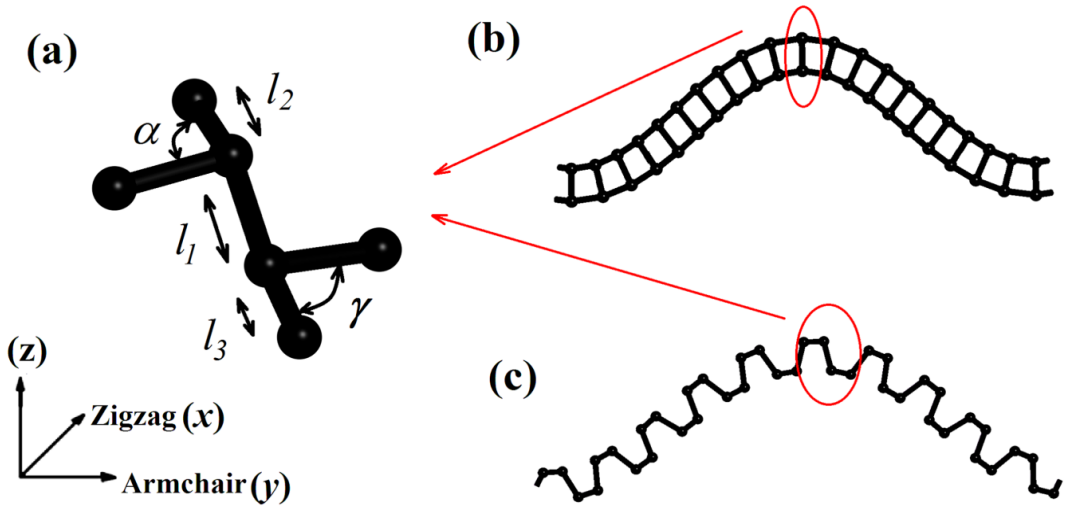

Fig. 3.4. (a) The definitions of the structural parameters for phosphorene. The unit cell at the top peak of the rippled phosphorene is used to analyse the bonding configuration changes under compressive strain along the zigzag (b) and armchair (c) directions.

By comparing the behaviour of the band gap as shown in Fig. 3.5(a) and that of the relative variations of the bond lengths Δl_1 and Δl_2 as shown in Fig. 3.5(b), the correlation between the band gap change and the bonding configuration changes is found. More specifically, the band gap decrease is correlated with the increase of the difference between angles (α-γ), for the strain up to -20%, and after that, the band gap and the angle difference (α-γ) are roughly unchanged. Thus, it can be concluded that the strain sensitivity of the band gap for the compression strain up to -20% comes from the angular distortion of the bonds, which leads to substantial changes in the overlapping of the wave functions of neighbouring atoms and thus the variation of the band gap. The small variation of the band gap for the compression strain beyond -20% can be explained by the comparative immutability of the bond angles and lengths.

When the compressive strain is applied along the zigzag direction, the angle difference (α-γ) and the relative variation of bond length l_2 drastically increase, while the relative bond lengths l_1 and l_3 only slightly decrease as shown in Figs. 3.5(b) and (c). By comparing the band gap change and the bonding configuration changes, the drastic band gap change is it found to be correlated with the changes in the variation of the bond length Δl_2 and the angle difference (α-γ). It is the bonding configuration changes that lead to the significant change in the band gap.

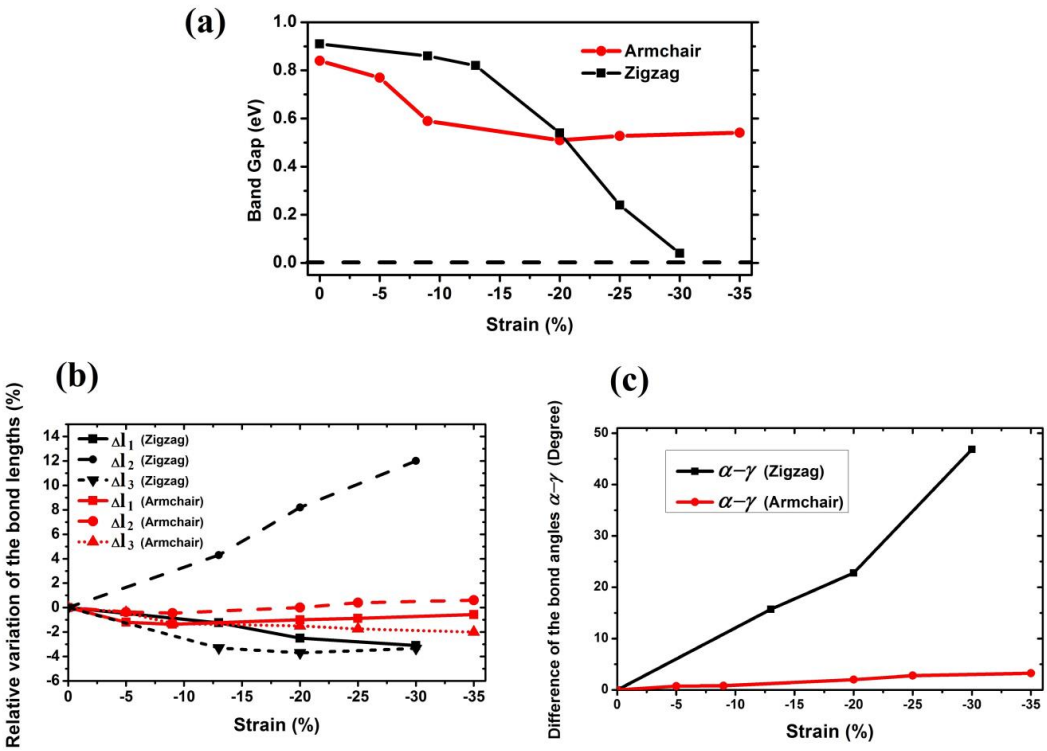

Fig. 3.5. (a) The variation of band gap for rippled phosphorene obtained under the compressive strain along the armchair (red line) and zigzag directions (black line). Zero band gap is denoted by the black dashed line. (b) The relative variations of bond lengths $\Delta l_1 = (l_1\text{-}l_1^0)/l_1^0$, $\Delta l_2 = (l_2\text{-}l_2^0)/l_2^0$, $\Delta l_3 = (l_3\text{-}l_3^0)/l_3^0$ and (c) hinge angle difference (α-γ) for phosphorene under compressive strains along the armchair (red line) and zigzag direction (black line).

To further understand the behaviour of the band gap, the density of states (DOS), the partial density of states (PDOS), and the local density of states (LDOS) of rippled phosphorene under the compressive strain applied along both armchair and zigzag directions are also considered. Fig. 3.6 shows the PDOS of phosphorene under the typical strains of 0, -20%, and -35% along the armchair direction and 0, -20%, and -30% along the zigzag direction. For the uncompressed phosphorene, that is, under zero strain, the *s*, p_x, p_y, p_z states are nearly equally distributed across the whole energy spectrum except the area within the band gap, where the frontier state is only comprised of p_z orbital in both cases, which is consistent with previous work [147].

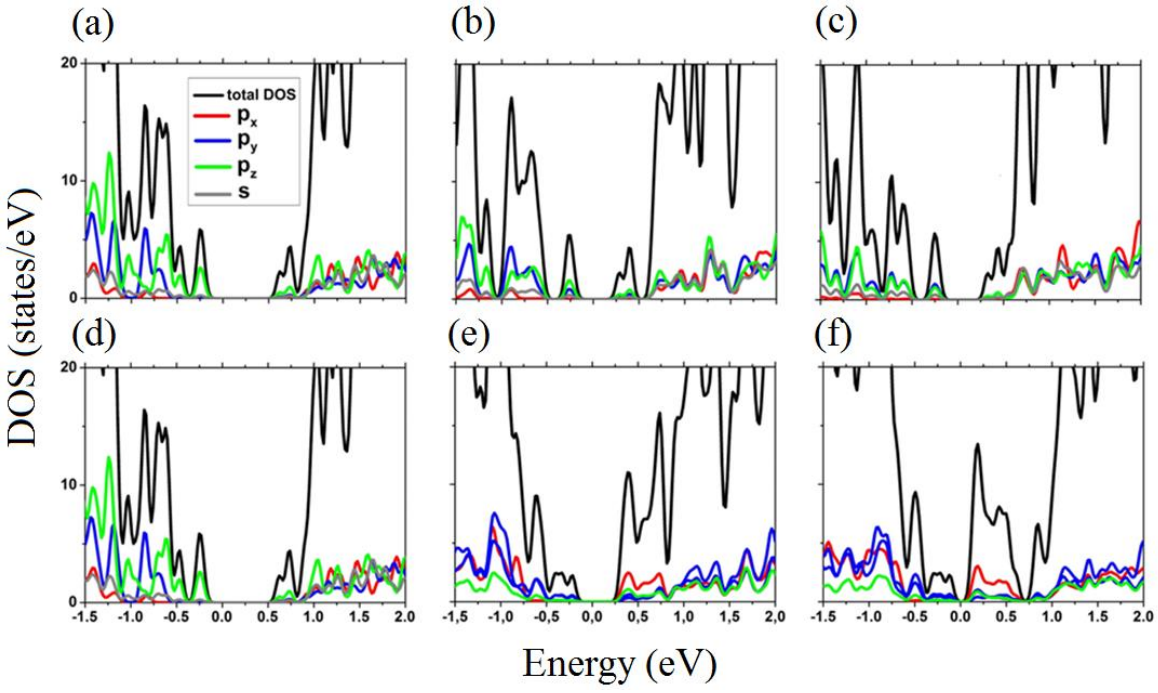

Fig. 3.6. The DOS and PDOS of the rippled phosphorene under the compressive strain: (a) 0%, (b) -20%, and (c) -35% along the armchair direction, and (d) 0%, (e) -20%, and (f) -30% along the zigzag direction. For each case, the electronic states *s*, p_x, p_y, p_z are represented by grey, red, blue and green lines, respectively. The total DOS is plotted as the black line.

As shown in Fig. 3.6(b), at -20% strain along the armchair direction, the contribution of p_y state to both the VBM and CBM increases and the VBM shifts towards the CBM. Under -35% strain as shown in Fig. 3.6(c), the gap between the VBM and the CBM is nearly unchanged, and p_y and p_z states have an equal contribution. Therefore, the contribution of p_y state to the VBM and the CBM increases accompanying the change of the band gap. As shown in Figs. 3.6(e) and (f), at -20% and -30% strains applied along the zigzag direction, the CBM shifts towards the VBM and the contribution of p_x state increases with the increase of the compressive strain. There is an important difference between the flat phosphorene and the rippled phosphorene: for the flat phosphorene, in the valence top, only p_y state is present while p_x state is clearly absent, signifying the linear dichroism in the flat phosphorene [147]. For the rippled phosphorene along the zigzag direction, a strong mixing of p_x and p_y states occur in the valence top, suggesting the disappearance of linear dichroism in the rippled phosphorene.

Next, the localized electronic properties by looking into the PDOS of atoms on different parts of the ripple, particularly, those atoms that are highly strained and located at the peaks, are examined. Figs. 3.7(a) and (c) show the rippled phosphorene configurations at a strain of -20% along the armchair and zigzag directions, respectively. The PDOS of the atoms marked by "1"-"4" are considered. For the rippled phosphorene compressed along the armchair direction, the main contribution to the CBM is from p_z states of atoms "1"-"4", with a dominant contribution from atom "1", as shown in Fig. 3.7(b). In contrast, for the zigzag case, as shown in Fig. 3.7(d), the main contribution to the CBM is from p_x states of atoms "1" and "3", which experiences the largest tensile strain. It is seen that these atoms make the largest contribution to the states from 0.1 to 0.5 eV, which are related to the flat bands around

the Fermi level in Fig. 3.3(h). This means that the flat bands are related to the localized states of these atoms, which become less bonded and passivated with their neighbours. Consequently, these atoms, which are on the top (atom "1" and "3") and under high tension, are responsible for the reduction of the band gap.

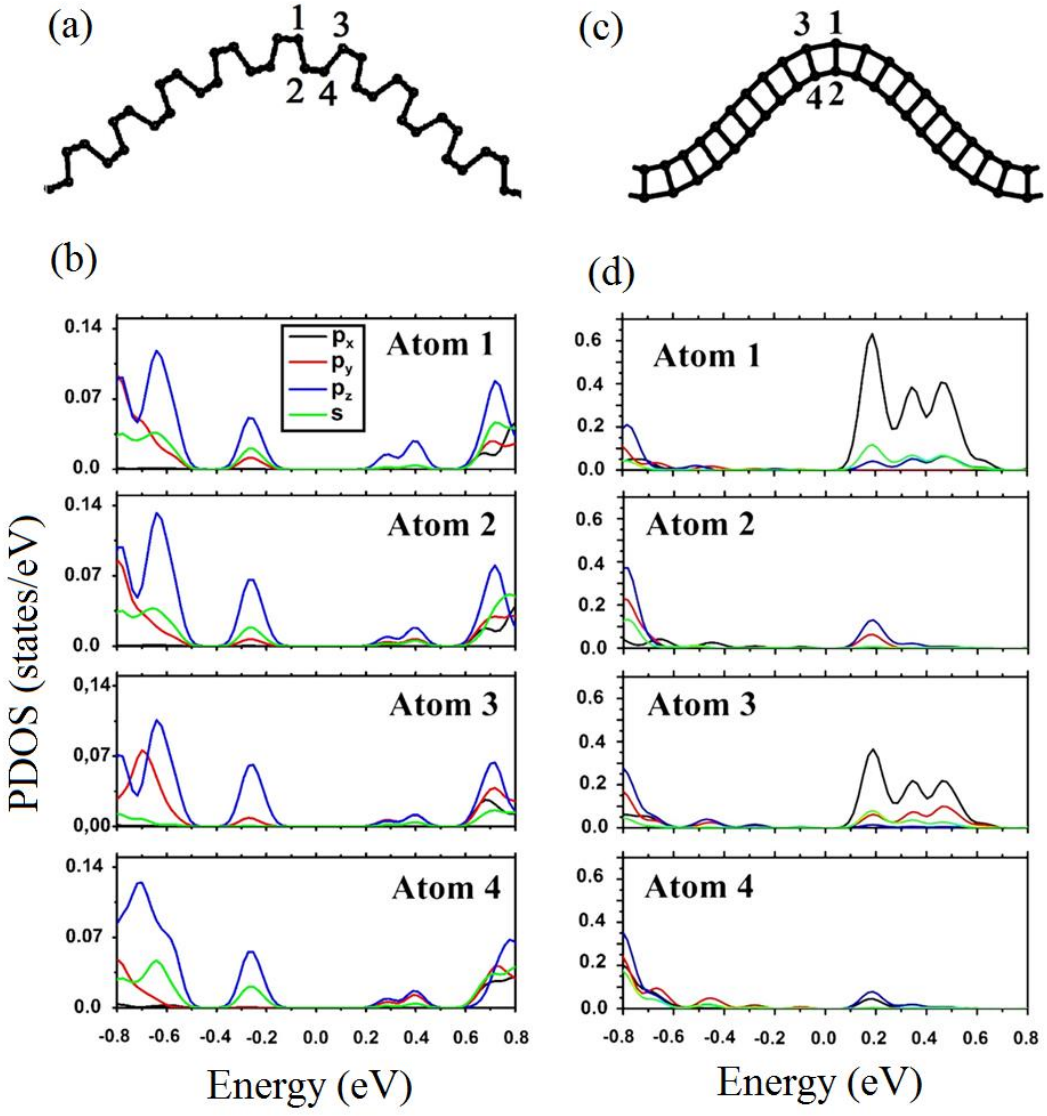

Fig. 3.7. The rippled phosphorene under a compressive strain of -20% along (a) the armchair and (c) zigzag direction, respectively. (b) and (d) show the PDOS for the atoms "1"-"4" in (a) and (c), respectively.

To present the spatial variation of the electronic structures, the LDOS of each pair of atoms along the line profiles of the ripples under the compressive strain of -35% along the armchair (Fig. 3.8(a)) and -30% along the zigzag direction (Fig. 3.8(b)) is plotted.

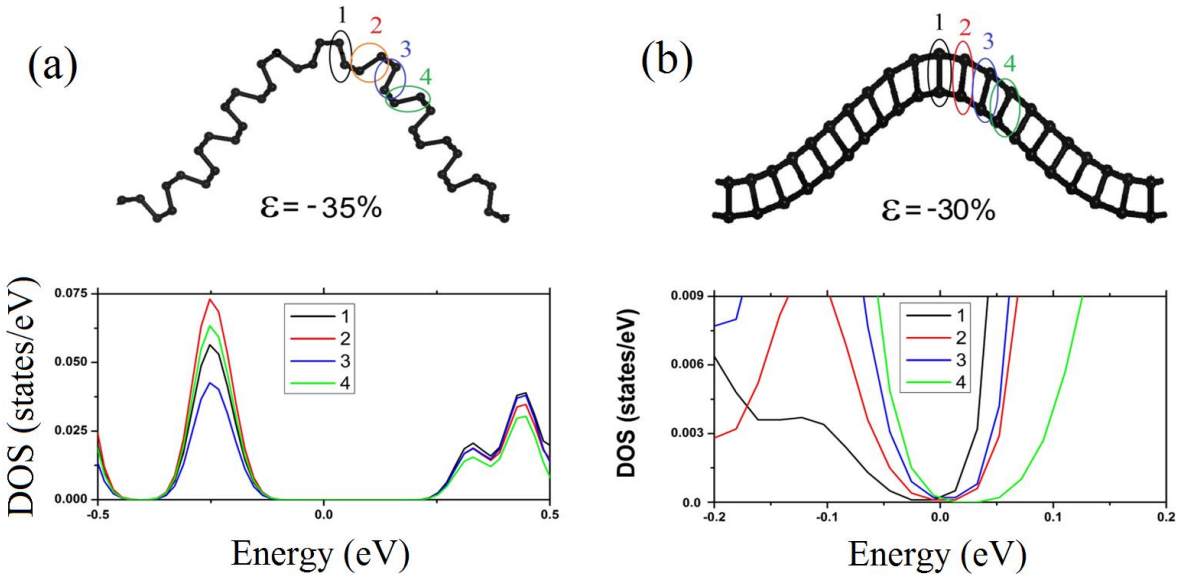

Fig. 3.8. The LDOS for the atom pairs of the rippled phosphorene compressed along (a) the armchair direction with a strain of -35% and (b) the zigzag direction at a strain of -30%, respectively. The atom pairs are marked as "1"-"4" and the colour of marker corresponds to the colour of the line for the LDOS.

For the ripples along armchair direction, it is seen that the local gaps of each pair of atoms are nearly overlapped, and there is no shift in the LDOS curves. On the contrary, for the rippled phosphorene along the zigzag direction, the LDOS of each atom pair shifts relatively towards each other. A red-shift of the states is predicted for atoms with positions approaching the peaks, while a blue-shift of states for atoms is located in the middle part of the wave-like profile. This explains the variation of band gap and confirms the extraordinary

tunable properties of the rippled phosphorene. Such spatially dependent alignment of valence and conduction bands is able to facilitate the separation of electrons and holes to different parts. Moreover, this spatial modulation of the band gap is also able to induce the funnel effect in a reduced spatial region. Funnelling has been recently proposed as a powerful strategy to enhance the efficiency of energy harvesting devices by facilitating the collection of photogenerated carriers [88, 148].

The obtained results suggest that the electronic structure of rippled phosphorene formed under compressive strain along the armchair direction is more robust than that along the zigzag direction. The latter should present strong spatially-dependent behaviour of the local quantities, such as electronic and optical properties, which allow the engineering of rippled phosphorene by taking advantage of its extraordinary flexibility.

3.2.2 Structure and electronic properties of vacancy-containing phosphorene

According to the band structure shown in Fig. 3.9(a) (lower panel), perfect phosphorene is a direct semiconductor with a band gap of 0.88 eV, which is consistent with previous studies [14, 149-152]. Herein only the lowest energy configuration of MV, which consists of pentagon-nonagon (59) rings as shown in Fig. 3.9(b) (upper panel), and that of DV, which consists of pentagon-heptagon-pentagon-heptagon (5757) rings as shown in Fig.3.9 (c) (upper panel) are examined.

For the 59 MV, removal of a phosphorus atom from perfect phosphorene creates unpassivated atoms and dangling bonds in the defect core. While the MV-containing

phosphorene exhibits essentially the same band gap as perfect phosphorene, there is a significant readjustment of band lines according to Fig. 3.9(b) (lower panel). A partially occupied defect band, which crosses the Fermi level, appears at about 0.01 eV above the VBM of the host phosphorene, suggesting the easy production of hole states (*p*-type conduction) even upon moderate thermal excitations. Although MV-containing phosphorene still possesses a direct band gap, the VBM of the host phosphorene shifts from Γ point in the perfect case to Y point. This change in the band structure may affect the optical emission efficiency of phosphorene.

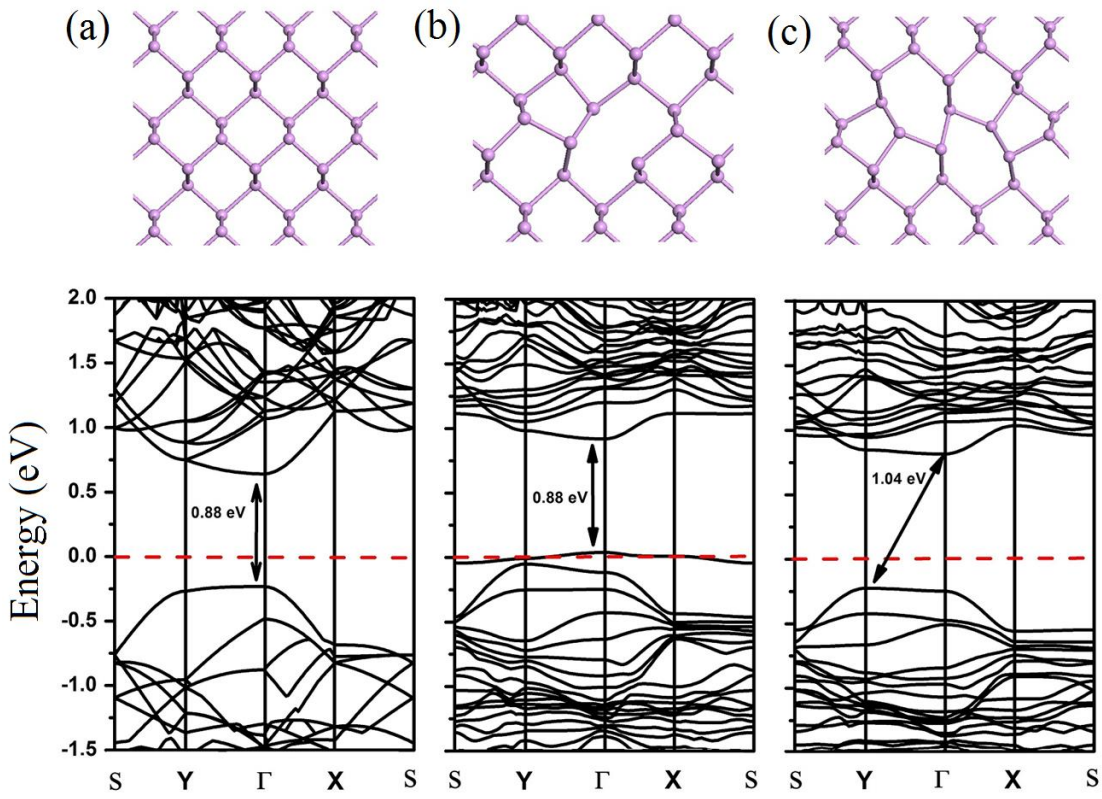

Fig. 3.9. The atomic configurations (upper panel) and band structure (lower panel) of phosphorene (a) perfect, (b) with 59 MV defect, (c) with 5757 DV defect. The red dashed line indicates the Fermi level.

For the DV-containing phosphorene, it is found that the 5757 DV defect shifts the VBM and CBM downward and upward, respectively, which leads to an increase in the band gap up to 1.04 eV (Fig. 3.9(c)). This increase may arise from the large lattice distortion and local strain induced by the DV [153]. Unlike MV defect, there is no defect state in the band gap for the DV-containing phosphorene due to the absence of dangling bond and the full passivation of atoms. Similar to the MV case, the VBM shifts from Γ to Y point, and there is a direct-indirect transition of the band gap upon the introduction of 5757 DV. Such direct-indirect band gap transition and an increase in the band gap could be detectable in the optical spectrum, and blue shifts of the emission and adsorption peaks may be used to corroborate the presence of the 5757 DV defect.

3.2.3 Interaction of rippled and vacancy-containing phosphorene with typical environmental molecules

Atomically thin 2D materials are highly flexible and tend to form ripples or wrinkles in either suspended or supported sheets [88, 148]. Curvatures due to ripples can induce inhomogeneous deformations of the lattice and modify the chemical properties, as shown in graphene and CNT [154-158]. It is also known that for atomically thin 2D materials, lattice imperfections can be easily introduced during fabrication or intentionally produced via electron beam or other high-energy particle excitations [159-161]. For phosphorene, this issue seems to be even more critical since the atomic vacancies in phosphorene are calculated to be easily formed and abundant at ambient condition with their much lower formation energy (1.65 eV) than other 2D materials [153]. In addition, vacancies in phosphorene are

highly mobile with an ultralow diffusion barrier of 0.30 eV compared to 1.39 eV for a vacancy in graphene [153]. Such itinerant vacancies may greatly affect the stability of phosphorene in the air with respect to the interaction with environmental molecules. Hence, it is important to investigate the effect of absorption of typical environmental molecules, such as H_2O, O_2 and NO on the electronic structures of perfect, MV- and DV-containing and rippled phosphorene.

Physisorption of H_2O and O_2 molecules above vacancies. The physisorption of the H_2O and O_2 molecules above the phosphorus-deficient phosphorene is considered. For each molecule, several possible absorption positions on perfect and defect-containing phosphorene are examined. All subsequent calculations on the electronic properties and energetics are based on the lowest-energy configuration. The lowest-energy configurations for H_2O and O_2 physical adsorptions on perfect, MV and DV-containing phosphorene are shown in Figs. 3.10 and 3.11, respectively. For the most stable binding configurations of the H_2O molecule adsorbed on perfect phosphorene (Fig. 3.10(a)), one of the O-H bonds is oriented parallel to the surface along the armchair direction while the other is nearly normal to the surface. The in-plane O-H bond is located directly above the ridge of phosphorene. The distance from the molecule to the surface d is 3.01 Å and the adsorption energy E_a is -0.187 eV, which is consistent with previous work on phosphorene [13]. For the most stable binding configuration of H_2O adsorption on the MV defect (Fig. 3.10(b)), both two O-H bonds are oriented nearly parallel to the surface and located directly above the MV position, with d = 2.42 Å and E_a = -0.193 eV. Figure 3.10(c) shows the lowest-energy geometry of H_2O adsorbed on phosphorene with the DV defect, where the H_2O is located above one of the pentagon rings of the 5757 defect with d = 2.66 Å and E_a = -0.205 eV.

For the most stable binding configuration of the O_2 molecule adsorbed on perfect phosphorene (Fig. 3.11(a)), the O-O bond is oriented parallel to the surface along the armchair direction and located directly above the ridge, with d = 2.80 Å and E_a = -0.489 eV. The most stable configuration for the O_2 molecule absorbed on the MV defect is presented in Fig. 3.11(b), where the O-O bond is located directly above the MV position, tilting about 45° away from the surface, with d = 2.94 Å and E_a = -0.489 eV. For the most stable binding configurations of O_2 adsorbed on the DV defect (Fig. 3.11(c)), the O-O bond deviates slightly from the in-plane surface and is located directly above the central P-P bond shared by the two neighbouring heptagons, with d = 3.02 Å and E_a = -0.705 eV.

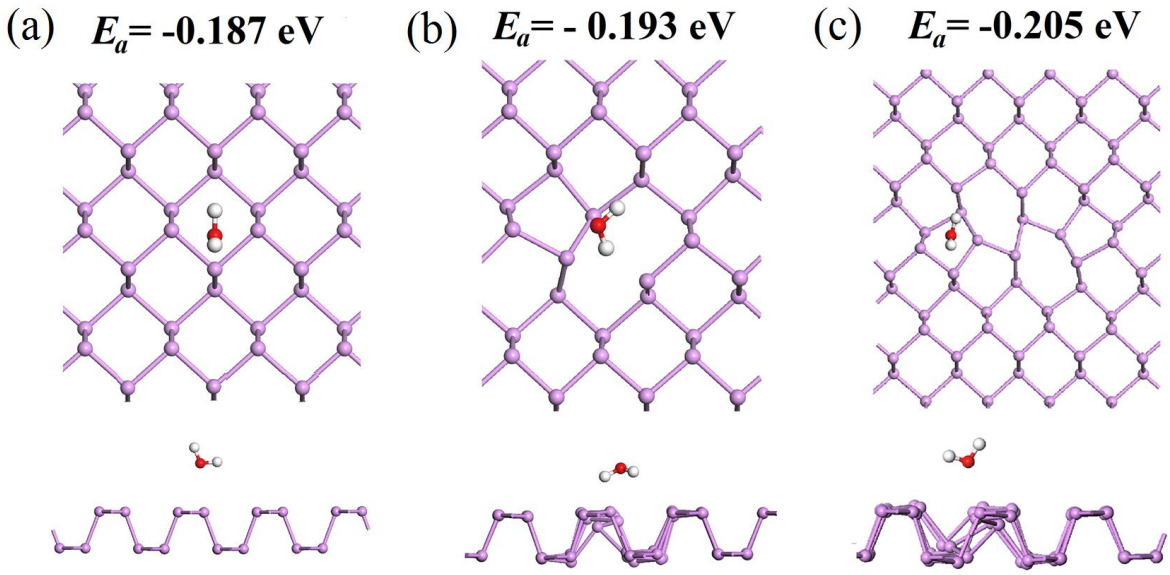

Fig. 3.10. The top and side views of the lowest-energy configurations of H_2O molecule adsorbed on phosphorene. (a) for perfect, (b) with MV defect and (d) with DV defect. The balls in blue, red and white represent phosphorus, oxygen and hydrogen atoms, respectively.

The O-O bond length of the isolated molecule changes from 1.22 Å to 1.25, 1.24, and 1.24 Å, upon adsorption on perfect, MV, and DV-containing phosphorene, respectively. This elongation of the O-O bond length signifies a strong electron transfer between the substrate and the O_2 molecule, and the transferred charges mostly occupy the $2\pi^*$ antibonding orbital. Therefore, the O-O bond is weakened even for a physisorbed O_2 molecule on phosphorene, and as a result, the energy for the O-O bond splitting is lowered, explaining the high affinity of phosphorene to oxygen.

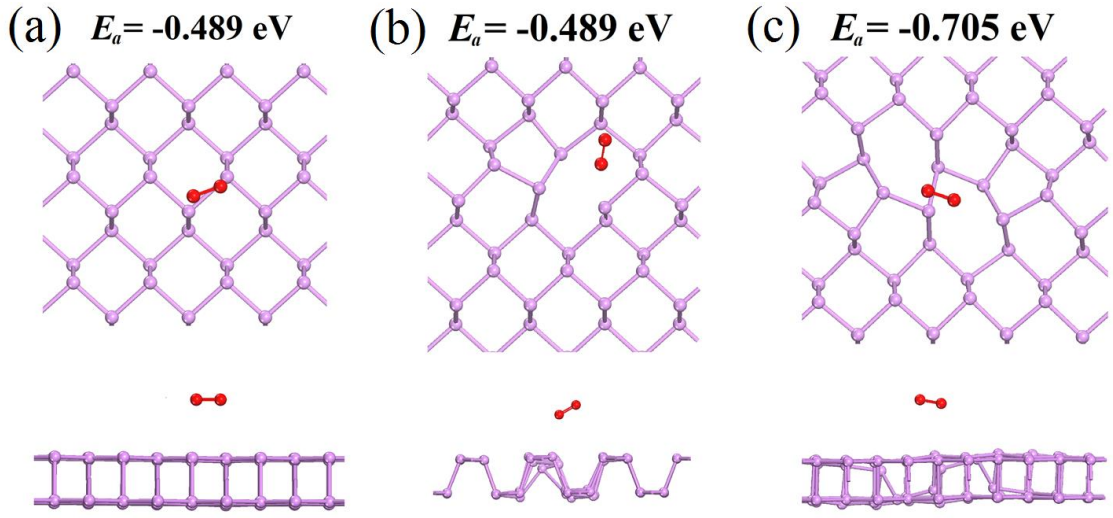

Fig. 3.11. The top and side views of the examined possible absorption configurations of the O_2 molecule adsorbed on phosphorene. (a), (b) and (c) perfect, (d), (e) and (f) with MV defect, (j), (h) and (i) with DV defect. The balls in blue and red represent phosphorus and oxygen atoms, respectively. The lowest-energy configurations of O_2 molecule adsorbed on phosphorene are shown in (a), (d) and (j) for perfect, with MV defect and with DV defect, respectively.

Interestingly, in contrast to the common notion that defects in 2D materials generally have a higher chemical affinity to adsorbates, the results here show that the presence of MV

has almost negligible effect on E_a of the H_2O and O_2 molecules compared with the adsorption on the perfect surface. A possible underlying reason is that the defect states are well self-passivated due to the highly puckered structure of phosphorene since the atoms in the defect core cross two neighbouring ridges and tend to have a stronger interaction and hybridization than other planar 2D materials like graphene and MoS_2. The above scenario is consistent with the previous study showing that the defects in phosphorene are nearly electronically inert [162]. For the DV defect, it can only slightly enhance the physisorption of the H_2O molecule (with E_a from -0.187 eV for perfect case to -0.205 eV for DV case) but greatly promote the adsorption of the O_2 molecule (with E_a from -0.489 eV for perfect case to -0.705 eV for DV case). The promoted interaction may be due to the large lattice distortion and bond deformation around the DV core. The current study suggests that the vacancy-containing phosphorene shows almost the same affinity to the water molecules from the thermodynamics point of view due to the comparable energy release with the physisorption above the perfect lattice.

Electronic structure and states alignment. Figures 3.12(a)-(c) present the DOS of perfect phosphorene, and phosphorene with MV and DV defects, respectively. It is seen that a MV defect can cause an enhancement in the electronic states around the top of the valence band as reflected by the increase in the peak intensity in the LDOS in Fig. 3.12(b) compared with that of perfect phosphorene in Fig. 3.12(a). This is attributed to the newly formed defect states above the VBM as shown in the band structure of Fig. 3.9. For the 5757 DV defect, as shown in Fig. 3.12(c), the DOS profile is quite similar to that of perfect phosphorene, and there are no defect states within the band gap.

In contrast, for the H_2O physisorption, no additional electronic state within the fundamental band gap is formed for either perfect or defected phosphorene (Figs. 3.12(d)-(f)). The value of the respective band gap for perfect, MV and DV-containing phosphorene is almost the same as for pristine phosphorene. However, the presence of vacancies on the surface significantly affects the alignment of the molecular levels of H_2O with respect to those of phosphorene. The three highest occupied molecular orbitals (HOMO) of the H_2O molecule, named according to the irreducible representation of the point group of H_2O, are $1b_1$ (HOMO), $3a_1$ (HOMO-1), and $1b_2$ (HOMO-2). All these levels are greatly upwardly shifted by around 1 eV in the MV- and DV-containing phosphorene. This readjustment of the molecular levels alignment is a clear indication of a different charge transfer amount and different interactions between water and phosphorene. Interestingly, for H_2O adsorbed on a perfect sheet, the $3a_1$ orbital is the most broadened one due to its favoured orbital mixing with the P atom. The situation becomes different for the adsorption of MV and DV defects, where the $1b_1$ state of the H_2O molecule is the most broadened one. This difference reflects the fact that H_2O is prone to have a different binding mechanism at the vacancy site compared with perfect one.

In contrast, for O_2 molecule, its physisorption can substantially modify the electronic structure of both perfect and defected phosphorene. Figures 3.12(g)-(i) show the LDOS for perfect, MV and DV-containing phosphorene, respectively. The adsorption of O_2 induces additional states with HOMO being located in the proximity of the VBM region. For all the cases, the antibonding LUMO state ($2\pi^*$, down) is located in the band gap of phosphorene above the Fermi level, while the HOMO state (2π, up) is slightly broadened for perfect and narrowed for MV and DV-containing phosphorene.

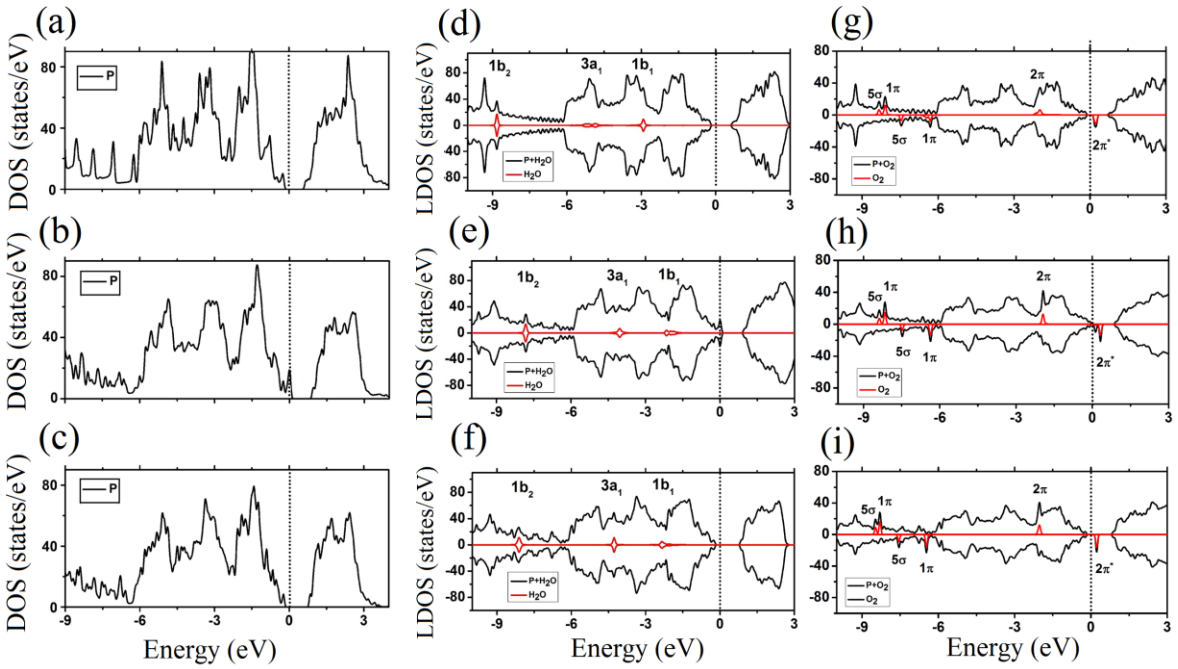

Fig. 3.12. The DOS structure of phosphorene: (a) perfect, (b) with MV defect, and (c) with DV defect. LDOS of H_2O and O_2 on phosphorene: (d), (g) perfect, (e), (h) with MV defect, and (f), (i) with DV defect. The spin-up and -down bands for H_2O and O_2 are symmetrical and shown by the red lines, while black lines represent the total DOS. The dashed line indicates the Fermi level.

Figure 3.13 shows the band structure of O_2-adsorbed phosphorene for the three cases. The spin triplet states (LUMO, $2\pi^*$) of O_2 remain unoccupied for all the cases with the degeneracy being strongly lifted for the perfect case. Unlike the case of the H_2O molecule absorption, the alignment of the energetic level of orbitals of O_2 with that of phosphorene is almost insensitive to the presence of vacancies. Therefore, the O_2 passivation of vacancies is able to induce trap states in the band gap of phosphorene, which is different from the case of sulphur vacancy in MoS_2, where the O_2 adsorption at the vacancy site can change the electronic nature of the vacancies from carrier-traps to electronically benign sites [149].

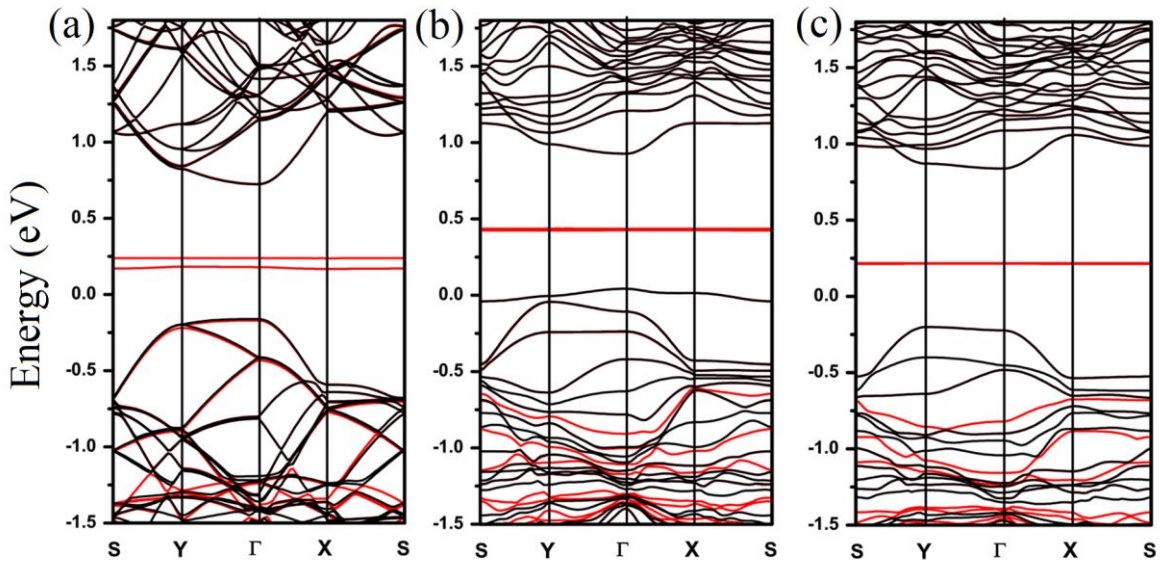

Fig. 3.13. The band structure of O_2 on phosphorene: (a) perfect, (b) with MV defect, and (c) with DV defect. The energetic levels associated with the O_2 molecule are plotted in red.

Modulation of carrier density and charge transfer. The electronic interaction between the H_2O and O_2 molecules with phosphorene is analysed by calculating the DCD $\Delta\rho(r)$ (as it is discussed in Section 3.2). The isosurface of $\Delta\rho(r)$ for the H_2O molecule adsorbed on perfect, MV- and DV-containing phosphorene are depicted in Figs. 3.14(a)-(c), respectively. It is seen that there is a depletion of electrons in the H_2O molecule and an accumulation of electrons in the nearest P atoms of the perfect surface (Fig. 3.14(a)), and the H_2O molecule donates electrons to phosphorene (~0.01 *e* per molecule). In the case of MV defect, the donor ability of the H_2O molecule increases, and the total amount of transferred charge increases significantly up to 0.12 *e* (Fig. 3.14(b)).

In case of DV defect, the total amount of the charge transferred from the H_2O molecule is 0.05 *e* (Fig. 3.14(c)). Due to the charge transfer from water to phosphorene, an effective dipole pointing toward vacuum should be established across the molecule-phosphorene

interface. It is expected that the surface coverage of H_2O molecules under humidity condition could decrease the work function of phosphorene layer due to the presence of the dipole layer, which in turn could affect the charge injection from the electrode to the channel layer and thus the device performance.

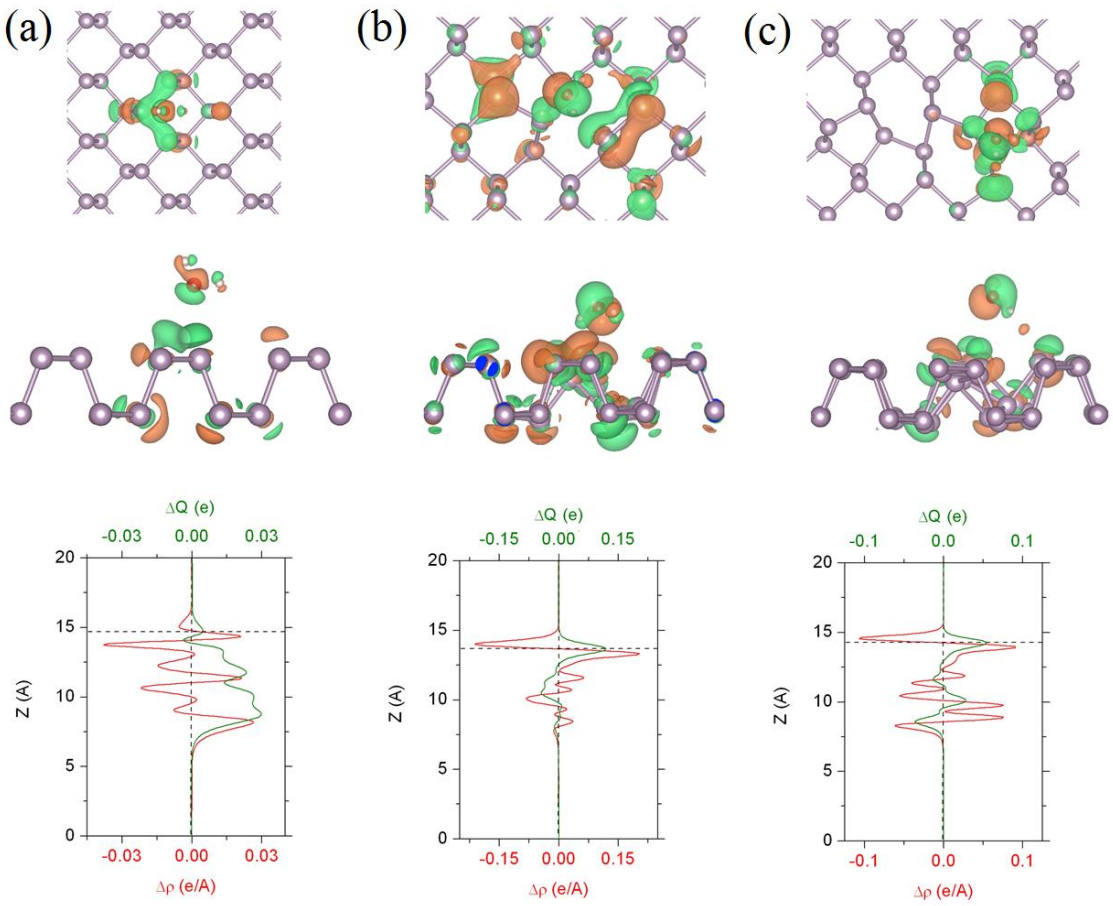

Fig. 3.14. The charge redistribution for the H_2O molecule absorbed on (a) perfect, (b) MV- and (c) DV-containing phosphorene. The top and middle panels: top and side views of the 0.02 $Å^{-3}$ DCD isosurface. The green (orange) colour denotes depletion (accumulation) of electrons. The bottom panel: plane-averaged differential charge density $\Delta\rho(z)$ (red line) and the amount of transferred charge $\Delta Q(z)$ (green line) between the H_2O molecule and phosphorene.

Figures 3.15(a)-(c) present the isosurface of $\Delta\rho(r)$ for the O_2 molecule adsorbed on perfect phosphorene, and phosphorene with MV and DV defects, respectively. It is found that O_2 accepts electrons from perfect phosphorene with around 0.035 *e* per molecule (Fig. 3.15(a)). The MV defect slightly decreases the donor ability of the O_2 molecule with the total amount of charge transfer amounting to 0.03 *e* (Fig. 3.15(b)). In contrast, the DV defect receives a tiny charge of 0.01 *e* from the molecule, partly due to the fully compensated structure and weak dipole interaction (Fig. 3.15(c)). Therefore, the carrier density of phosphorene can be modulated by water molecules, oxygen molecules, and vacancies.

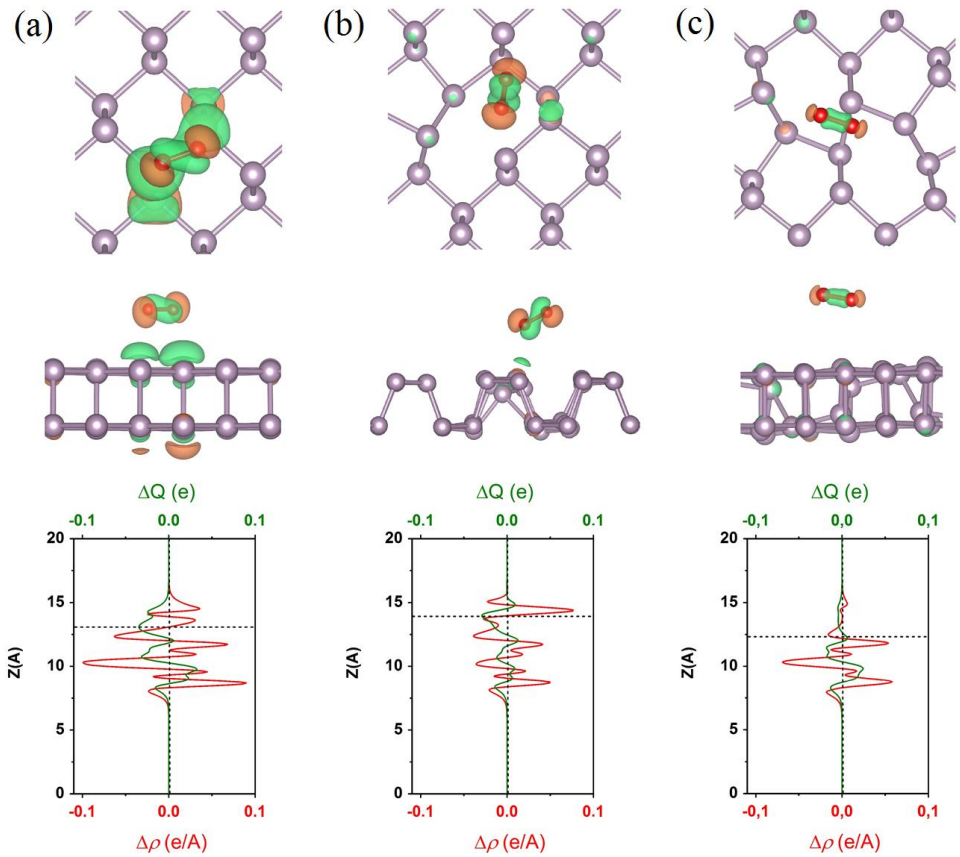

Fig 3.15. The same as in Fig. 3.14 but for the O_2 molecule.

Effect of the MV defect on the dissociation of the O_2 molecule. Experiments have shown that phosphorene can be easily oxidized under air condition largely due to the oxygen molecules [163-165]. However, the underlying mechanism of the kinetic process from the O_2 gas molecule to form chemically bonded O-P species is still unclear. Recent work [149] on GaS and MoS_2 semiconductors has shown that most molecules, including H_2O, are only physisorbed on defects, while the O_2 molecule may reach the chemisorbed state from the physisorbed state if the energy barrier is overcome.

The present study shows that the H_2O molecule can only be physisorbed while the O_2 molecule experiences an energy barrier E_b from the physisorption to chemisorption on phosphorene. It is also found that this barrier can be strongly affected by the presence of vacancies in phosphorene. The detailed pathway from the initial state (IS), to the transition state (TS) and to the final state (FS) for oxidation of phosphorene by the O_2 gas molecule on perfect and MV sites are shown in Figs. 3.16(a)-(c). The calculated E_b for the perfect case is 0.81 eV. From Fig. 3.16(b), it is seen that the presence of MV can significantly reduce the barrier to 0.59 eV. According to these results, a large amount of O_2 molecules in air is able to be physisorbed at room temperature. The obtained results on the chemisorbed energies (4 eV per O_2) are well consistent with a recent work [166].

According to the rate theory, the transition time from the physisorbed state to the chemisorbed state is

$$t \approx 1/\left(f \cdot e^{-E_b / k_b \cdot T}\right) \tag{3.3}$$

where E_b is the energy barrier, k_b is the Boltzmann constant, T is a temperature and f is the attempt frequency, defined as $f = n \cdot v \cdot s_d$, where n is the density of the O_2 molecules in air, v

is the speed, and s_d can be taken as the square of lattice parameter. Hence, at the room temperature of 300 K, one atmospheric pressure, and f of around 10^8 molecules/s, the time of the O_2 molecule chemisorption on perfect phosphorene is $t \approx 109$ hours. This value reduces to 1.33 min on the MV site, which is about 5000 times shorter.

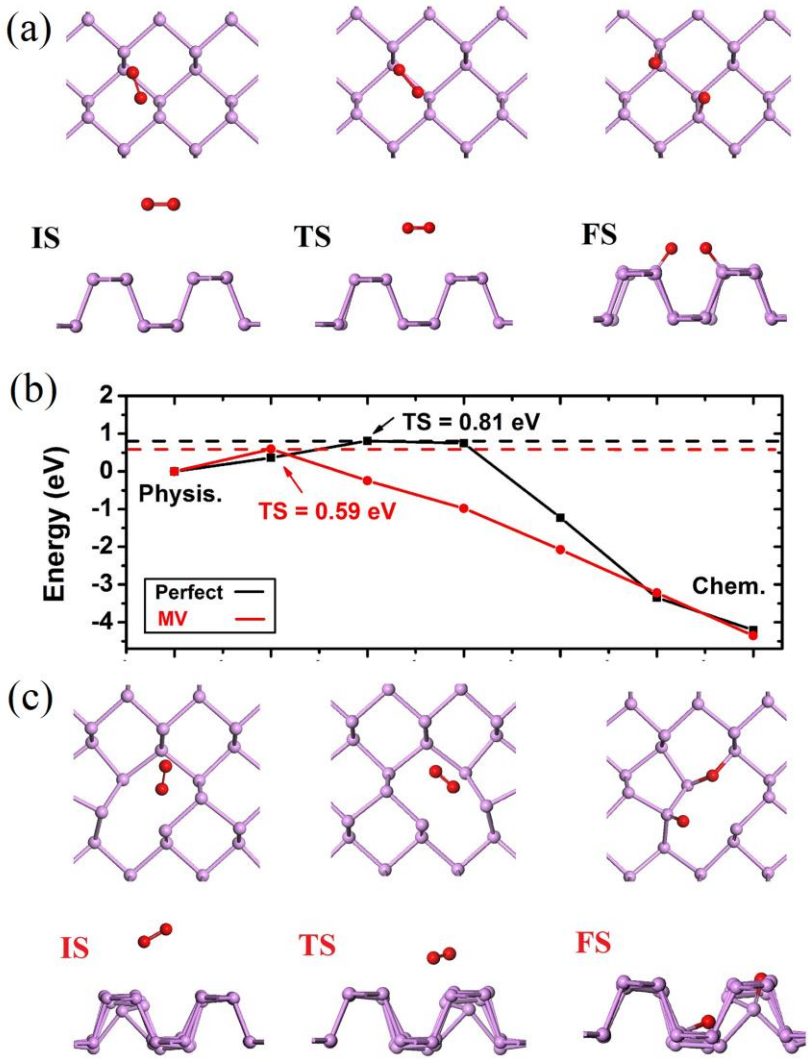

Fig. 3.16. The atomic configurations from the physisorbed to the chemisorbed state in the dissociation process of the O_2 molecule on (a) perfect (black line) and (c) MV-containing (red line) phosphorene. The P and O atoms are coloured in purple and red, respectively. (b) The energetic profiles of the reaction pathway obtained from NEB calculations.

Thus, the findings revealed here suggest that the oxidation rate is much higher at the vacancies than at the perfect sites and that phosphorene sheets with high-concentration vacancies can be more easily oxidized than vacancy-free phosphorene. Passivation and repairs of these vacancies in phosphorene should be effective in enhancing the chemical stability of phosphorene. However, the oxidation is also limited by the possible absorbed sites. The formation energy of P vacancy is 1.65 eV, and the concentration of the intrinsic vacancy estimated by $N_{host}\cdot\exp(-1.65/kT)$, where N_{host} is the total number of P atoms of the corresponding perfect lattice, is several orders of magnitude smaller than that of the host P sites. Hence, the oxidation rate of phosphorene is still largely dominated by the reaction at the perfect sites. Effects of vacancies tend to be more significant for small size phosphorene flakes which contain a large number of edges with accumulated vacancies.

Effects of ripples on the chemical activity of phosphorene with NO gas molecules. Next, the influence of ripples on the chemical activity of phosphorene upon interaction with the NO gas molecule is considered. Particularly, the absorption energy of the NO molecule on both planar and rippled phosphorene, and the charge transfer between the molecule and planar/rippled phosphorene are investigated. Several possible positions on the highly symmetric sites of the NO molecule on the both planar and rippled phosphorene, including both above the puckered hexagon and the zigzag trough, with the molecules being aligned either perpendicular or parallel to the surface are considered. To examine the curvature effect on the adsorption, the NO molecule adsorbed on both the concave and convex regions of the ripple are investigated. The lowest-energy configurations of the NO molecule adsorbed on the concave and convex regions are shown in Figs. 3.17(a) and (b), respectively.

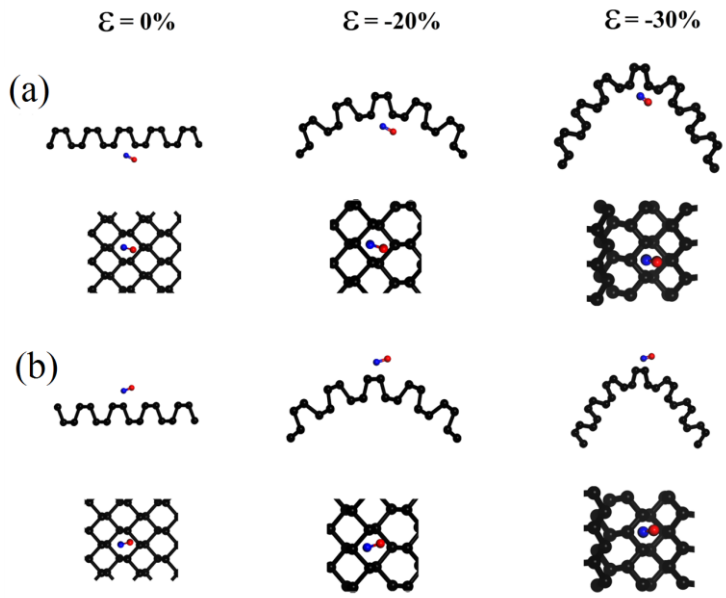

Fig. 3.17. The most stable adsorption positions of the NO molecule (a) below and (b) above the planar/rippled phosphorene surface. The balls in black, blue, and red colours represent the phosphorus, nitrogen and oxygen atoms, respectively.

It is found that for both cases, the absorption energy E_a of the NO molecule decreases with increasing the compressive strain for the position both above and below the phosphorene as shown in Fig. 3.18. The amount of charge transfer between the NO molecule and phosphorene is obtained by using the Bader analysis [167]. For the planar case, E_a= -0.29 eV, which is consistent with previous studies [13, 143]. It is found that the NO molecule accepts electron upon adsorption on phosphorene and the total amount of the charge transferred from phosphorene is 0.084 *e*. With increasing the strain from 0 to -30%, the acceptor ability of the NO molecule increases, and the total amount of transferred charge increases up to 0.206 *e*. Such changes can be attributed to the curvature effect which modifies the local carrier density and orbital hybridization as shown before. Therefore, ripple-induced deformation is an effective way to promote the chemical activity of phosphorene in terms of

absorption energy and charge transfer, and rippled phosphorene may be useful for gas sensing applications and for improving the doping efficiency by adsorbing chemical species.

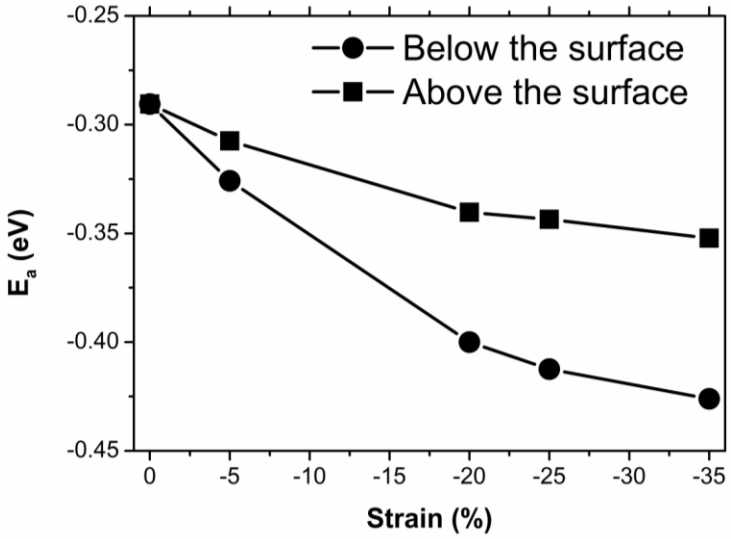

Fig. 3.18. The variation of the absorption energy of NO gas molecule on phosphorene surface with increasing the curvature by applying compressive strain.

3.3 Summary

In Chapter 3, the effects of ripples and vacancies on the electronic structure and chemical activity of phosphorene with typical environmental molecules have been analysed. By using first-principles calculations, it has been shown that ripples can lead to significant changes in the electronic properties of phosphorene. The strong spatial dependence of the electronic structure in rippled phosphorene along the periodic line profile may potentially allow the control of the carriers transport via ripple engineering. This study also helps to explain the recent experiment that observes the spatially dependent optical properties in rippled phosphorene, where periodic ripples with large curvatures have been obtained by

transferring phosphorene to a greatly pre-stretched elastomeric substrate, followed by a relaxation of the pre-strain in the substrate [168].

It has been found that different from other 2D materials, vacancy-containing phosphorene is almost inert to H_2O with the adsorption energy being almost the same as that in perfect phosphorene. For both perfect and vacancy-containing phosphorene, the H_2O molecule does not introduce any defect states in the band gap while the frontier orbitals of the O_2 molecule are aligned in the band gap of the VBM of the phosphorene. The O_2 molecule increases hole carriers and serves as a good electron scavenger for adsorption above perfect phosphorene. Moreover, the vacancy-modulated charge transfer from H_2O and O_2 molecules may allow the modulation of the concentration and polarity of carriers in phosphorene.

Finally, the investigations of the O_2 molecule dissociation kinetics have shown that the oxidation rate is around 5000 times faster in the vacancy site than the perfect site. Phosphorene samples with a large number of vacancies should be more easily oxidized than those of low-vacancy containing phosphorene. The new understandings revealed here for the interactions of the O_2 and H_2O molecules with phosphorene may inspire new strategies to exfoliate and protect phosphorene. In addition, we have also shown the abilities of the rippled phosphorene to promote the adsorption of the NO molecule and increase the charge transfer, signifying an enhanced chemical activity. The marked enhancement of the chemical activity suggests that rippled phosphorene is a promising material for gas sensing applications.

Chapter 4 Atomic-scale investigations of the unique properties of recently emerged 2D materials: Borophene, InSe, and antimonene and their comparison with phosphorene

The stability and electronic properties of borophene, indium selenide (InSe) and antimonene are studied and compared with these of phosphorene (considered in Chapter 3). In particular, investigations on i) the routes for the charge localization and the band gap opening of borophene via chemical functionalization, defect engineering and ribbon construction; ii) the mechanisms of InSe oxidation via its interaction with environmental molecules, by taking into account the roles of defects; and iii) the stability issue of antimonene under the environmental molecules are presented.

4.1 Exploring the charge localization and band gap opening of borophene

Recent success in synthesizing atomically thin 2D borophene on Ag (111) substrate [169, 170] has stimulated great interest in exploring the growth, structure and properties of this elemental 2D material [171, 172]. As a magic element with coexistence of covalent and ionic characters, boron can show a versatile electronic structure, including semiconducting, semi-metallic, and metallic phases [173-175]. Previous studies showed that free-standing borophene exhibits a highly anisotropic electronic structure [176]. With its high carrier concentration at the Fermi level, which is absent in graphene with a zero carrier density at the Dirac cone, the atomically thin borophene serves as an ideal platform for investigating the distribution and response of electron gas confined in an ultrathin layer with external perturbations.

As the boron atom has three valence electrons, it needs to pair with five additional electrons to satisfy the octet rule. However, in borophene, each boron atom forms bonds with six neighbours, thus favouring the metallic phase according to the band theory. The localization of its itinerant electrons and ultimately its band gap opening is an intriguing issue for electronic applications of borophene. Approaches for the band gap opening in 2D materials can be categorized into two groups: i) quantum confinement induced by the construction of finite-sized structures, like ribbons, edges and dots [177, 178], and ii) chemical functionalization [179]. However, the effectiveness of both approaches on the borophene band gap opening remains unclear. The formation of ionic bonds in a high-pressure boron phase [180] suggests a different charge distribution in boron materials in comparison with other 2D materials, especially graphene. The failure of the octet rule in pure borophene implies a new mechanism of the charge localization/delocalization, which is still to be understood. Hence, it is important to explore the routes for the charge localization and the band gap opening of borophene via chemical functionalization, defect engineering, and ribbon construction.

4.1.1 Computational details

For various chemically modified 2D borophene, a 20×15×1 Monkhorst-Pack grid is used for the *k*-point sampling in the first Brillouin zone. For the line (zigzag)-edge borophene nanoribbons (BNRs), a 20×1×1 (1×8×1) *k*-point sampling is used. To avoid the spurious interaction between periodical images, a vacuum space of 15 Å along the out-of-plane direction is created. The considered structures are relaxed until the forces become smaller

than 0.01 eV/Å. To more accurately describe the self-interaction and screening of carriers, the hybrid functional Heyd-Scuseria-Ernzerhof (HSE06) [38] is adopted for the work function calculations. AIMD simulations are performed at room temperature of 300 K using the Nose-Hoover method with a time step of 1.0 fs [181]. The formation energy E_{form} is defined as

$$E_{form} = E_{perfect} - E_{defect} - n \cdot E_{atom} \tag{4.1}$$

where $E_{perfect}$, E_{defect}, and E_{atom} are the total energies of the perfect and defective borophene, and the single boron atom, respectively, and n is the total number of the removed atoms.

To examine the stability of the considered structures, the average binding energy E_b of perfect borophene is calculated as

$$E_{binding} = (n_B \cdot E_B - E_{tot})/n \tag{4.2}$$

and the $E_{binding}$ of H- and F-functionalized borophene is calculated as

$$E_b = (n_B \cdot E_B + n_X \cdot E_X - E_{tot})/n \tag{4.3}$$

where E_{tot} is the total energy of the functionalized system, E_B is the energy of a single boron atom, E_X is the energy of a single H or F atoms, n_B is the total number of B atoms, n_x is the total number of H or F atoms, and n is the total number of atoms in the system.

The edge energy E_{edge} is defined as

$$E_{edge} = (E_{BNR} - n \cdot E_B)/L \tag{4.4}$$

where E_{BNR} is the total energy of the BNR, L is the length of the ribbon along the periodic direction, E_B is the total energy per atom in 2D borophene, and n is the total number of atoms.

4.1.2 Results and discussion

The modification of the electronic properties of borophene is explored via its surface functionalization by H and F atoms. It should be noted that several atomic models, showing long-wavelength negative phonon modes, have been proposed for monolayer borophene to match the experimental images of the samples grown under different conditions [182]. The closely-packed atomic model, as revealed in a recent experiment [169], is chosen (Fig. 4.1(a)) since other atomic models are its direct derivatives. The considered closely-packed model, which consists of equilateral triangles as the basic unit, has a P_{mmn} space group with a rectangular unit cell. It can be regarded as a staggered honeycomb lattice with additional atoms located at the hexagon centres. Each rectangular unit cell contains two symmetrically inequivalent boron atoms occupying the two 1a Wyckoff sites at the corner and face centre positions, respectively. The relaxed lattice constants are 1.618 and 2.864 Å along the *a* (line-edge) and *b* (zigzag) directions, respectively. To examine the extreme effect of the chemical functionalization, a 50% coverage of borophene surface with H- and F-functionalizing groups above a 2×2 supercell is considered due to the balance for maximizing the doping effect while maintaining the stability of the doped structure. Considering the relatively small radius of the boron atom, this concentration is quite high.

Figures 4.1(b) and (c) show the optimized structures and the electronic band structures of pristine, H- and F-functionalized borophene sheets with adsorption on both sides. Consistent with previous works [183, 184], the pristine borophene shows a metallic behaviour (Fig. 4.1(a)) with the Fermi level crossing the electronic levels. Owing to the puckered zigzag structure (side view), the pristine borophene shows an anisotropic electronic

structure with half-filled bands along the Γ-X (line-edge) direction but an energy gap along the Y-Γ (zigzag) direction. Such an intriguing electronic property implies an orientationally different quantum confinement effects in borophene, which may lead to angle-dependent plasmonic behaviour in this ultrathin metallic sheet.

Compared with the pristine borophene, the H-functionalized borophene shows only a small change in its lattice constant. In contrast, an F-functionalized borophene sheet shows significantly deformed B-B bonds, leading to a large distortion of the host borophene lattice. Such difference can be attributed to the strong subtraction of electrons from the sheet to the anionic adsorbents, in comparison with the H- group. Interestingly, the F-functionalization of borophene induces changes in the lattice constant along the zigzag direction, around 1%, while the change along the line-edge direction is only slight. Concerning the electronic properties, all these highly chemically functionalized borophene sheets remain metallic. This is in strong contrast to graphene where hydrogenation and fluorination are well known to lead to band gap openings. Therefore, the charge localization, which is necessary for the band gap opening, is hard to induce via the surface chemical functionalization of borophene.

Projected band analysis for the H-functionalized borophene (Fig. 4.1(b)) shows that the states around the Fermi level are predominantly populated with the H states. In contrast, the F states in the F-functionalized borophene are largely distributed below the Fermi level (Fig. 4.1(c)). In addition, upon the functionalization by these atoms, partially occupied levels are formed along the Y-Γ direction, which is on the contrary empty in pristine borophene. Therefore, selective atomic functionalization enables the modulation of the anisotropy in the electronic properties of borophene.

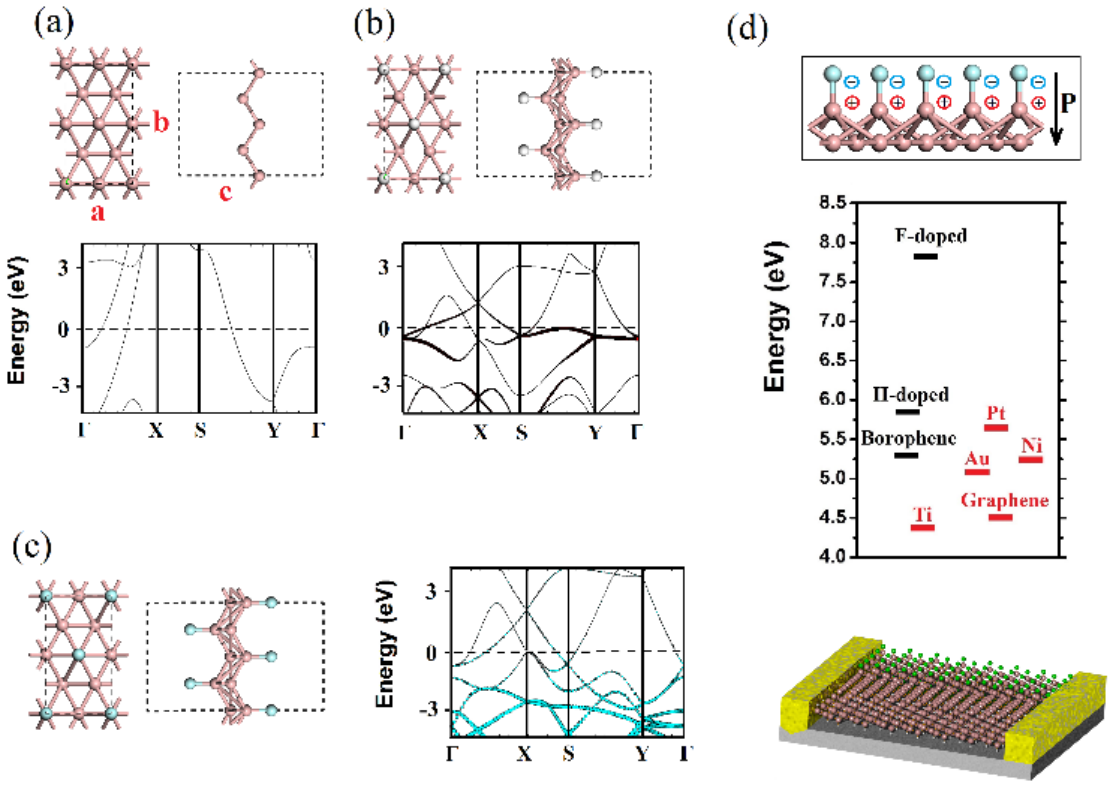

Fig. 4.1. The atomic configuration and the band structure of (a) pristine, (b) H- and (c) F-functionalized borophene. The component of the states scales with the radius of the black and cyan circles for H- and F-functionalized cases, respectively. (d) Inward dipole layer built in F-functionalized borophene due to the charge transfer (top panel). Comparison of the work functions of pristine, H-, and F-functionalized borophene (calculated with HSE method) with those of the common metals and graphene (middle panel). Schematic plot of the integration of the chemically functionalized borophene for improving the efficiency of the injection and carrier transport in nanoelectronics devices (bottom panel). The work functions of graphene and other metals are adopted from Refs. 185 and 186.

The above-mentioned robust metallicity in these surface functionalized borophene sheets is absent in graphene and TMDs. The finite density of these free carriers at the Fermi level suggests that borophene and its functionalized derivatives are promising for applications as interconnecting and field-emitting materials. Since the work function, which

quantifies the ability of electrons to move from the surface of a material to vacuum, is critically important for field emission and rectification of conducting barriers [187, 188], in the following, the change in the work functions of these functionalized borophene sheets is examined.

Figure 4.1(d) shows the energetic diagram of the work functions for various functionalized borophene sheets in comparison with other common bulk metals and graphene. From the diagram, the following important features can be identified. Firstly, the work function of a pristine borophene sheet is 5.31 eV (obtained via HSE calculation), which is larger than that of most listed metals, except Pt. Moreover, the work function of pristine borophene is also higher than that of graphene (~ 4.5 eV) [185]. This is surprising since a carbon atom has a larger electronegativity than a boron atom. The higher work function of borophene could be attributed to the nature of atomic states around the Fermi level. Borophene mainly consists of in-plane *s*-*p* hybridized (σ) states, which are lying lower than those the out-of-plane p_z (π) states in the graphene case. Thus, an electron in borophene is harder to knock out than that in graphene. Secondly, the work function of borophene increases slightly to 5.88 eV for the H-functionalized and dramatically to 7.83 eV for the F-functionalized borophene. This can be originated from the strong dipole layer pointing inward towards the central borophene layer due to its transfer of electrons to the functionalizing atoms (Fig. 4.1(d)). In other 2D materials, like graphene and TMDs, the density of electrons is negligible at the Fermi level, which means that the magnitude of the dipole layer is modest upon the chemical functionalization due to the limited charge transfer. In contrast, a borophene layer has a considerably high density of carriers at the Fermi level because of its intrinsic metallicity, giving rise to a pronounced charge flow and a built-in

dipole layer. This great tunability in the work function suggests that the chemically functionalized borophene sheets can be used as a buffer layer for reducing the contacting resistance and Schottky barrier at the interface. In addition, the high work function in the F-functionalized borophene sheet is particularly useful for electron collection and hole injection.

The effect of the atomic vacancies on the electronic properties of borophene. Both MV and DV with the loss of one and two boron atoms, respectively, in the 6×5 supercell (56 atoms), are considered (Fig. 4.2). In perfect borophene, each boron atom has a coordination number of six. With the creation of an MV, six peripheral atoms become fivefold coordinated and the defect core has a local symmetry of C_{2v} (Fig. 4.2(b)). For the DV, two different configurations exist: horizontal (C_{2v} symmetry) and tilted (C_i symmetry) DV, depending on the relative direction of the deleted boron dimer to the *a* lattice (Figs. 4.2(c) and (d)). The horizontal DV is slightly more stable with the energy of 0.07 eV and lower than that of the tilted DV. In the DV structures, there are two new-born fourfold boron atoms in the edge in addition to the six fivefold corner atoms. The calculated values of the formation energy E_{form} for MV, horizontal, and tilted DVs are -5.61, -12.58, and -12.51 eV, respectively. The relatively high values of E_{form} suggest that it is difficult to form isolated vacancies in borophene. However, the energy cost for forming an MV in borophene is smaller than that in graphene (-7.57 eV) and that of a boron MV in h-BN (from -7.50 to -10.20 eV) [153].

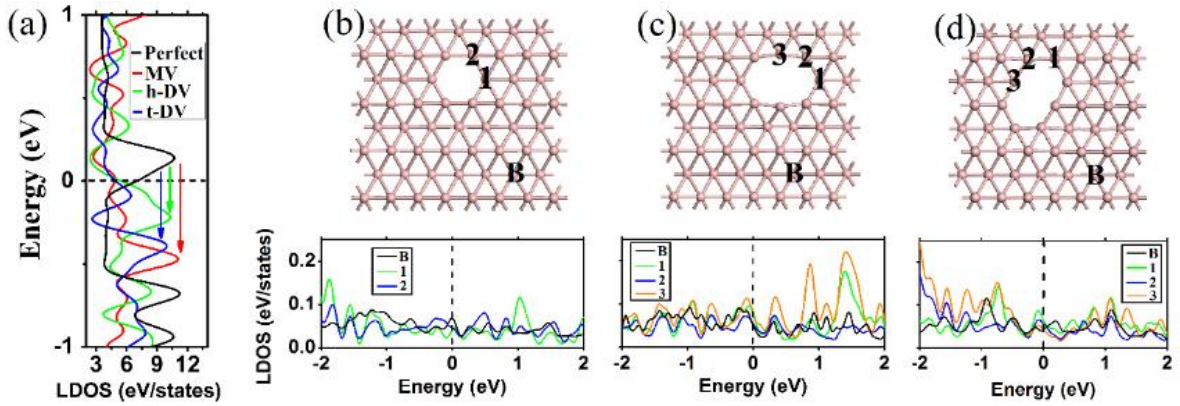

Fig. 4.2. (a) The comparison of the total DOS of perfect (black line), MV-containing (red line), horizontal DV-containing (green line), and tilted DV-containing (blue line) borophene. The atomic structure (upper panel) and LDOS (bottom panel) for several edge atoms of (b) the MV-containing, (c) the horizontal DV-containing, and (d) the tilted DV-containing borophene sheets. The LDOS of the labelled edge atoms (atoms 1, 2, and 3 are considered due to the symmetry reason) are compared with that of the boron atom (black line) far from the core of the vacancy. The black dashed line shows the position of the Fermi level.

It is well known that the electronic properties around the vacancy core may change dramatically owing to the breaking of the lattice periodicity [189]. Figure 4.2(a) shows the DOS in the perfect, MV-, and DV-containing borophene sheets. It is seen that the metallicity of these borophene sheets is robust against the presence of vacancies. Interestingly, the Fermi level significantly shifts upwards for the MV and DV cases compared with perfect borophene (see the arrows in Fig. 4.2(a)). The bands of vacancy-containing borophene sheets are non-zero at the Fermi level and mainly contributed by the p_z orbitals of the B atoms. Different from new localized states formed in the band gap-associated vacancies in MoS_2 [190] case, there are no peaks related to the dangling bond states due to vacancies in borophene. However, by comparing the LDOS of peripheral atoms in the defect core and

those of atoms far from the vacancy centre (Figs. 4.2(b)-(d), bottom panel), it is seen that there is a significant difference in the LDOS profiles, suggesting that the states are renormalized greatly in the defect centre.

To explore the routes to introduce localized states in the intrinsic metallic borophene, one-dimensional (1D) nanostructures of borophene, that is, nanoribbons are examined. Both the line- and zigzag-edge ribbons are considered. Following the normal nomenclature of nanoribbons in graphene, MoS_2, and phosphorene, the BNR along the line-edge or zigzag direction is named as LE-N_d BNR or ZZ-N_z BNR according to the number of B-B dimer lines (N_d) or zigzag chains (N_z) across the ribbon width. Figures 4.3(a) and (b) show the atomic models and the band structures of pristine LE-9 and LE-10 BNR, selected as the representatives for the odd- and even-width BNRs, respectively. It is seen that both types of BNRs are metallic without any localized states and band gap opening, which is in a strong contrast with graphene [191]. The orbital-resolved band structures suggest that the out-of-plane p_z and in-plane p_y orbitals of B atoms are dominant at the Fermi level, which may account for the quasi-planar structures at the edges (red circles in Figs. 4.3(a) and (b)). The transporting states consisting of p_x orbitals (blue lines in Figs. 4.3(a) and (b)) and aligned along the momentum (Γ-X) direction are quantized with an energy gap in the band dispersion. The isosurface plots of electronic densities of the valence band clearly reflect this quantized feature of p_x states with regular nodal planes across the width direction of ribbons. The formed quasi-1D p_x states are highly delocalized, which may facilitate the stabilization of the LE edge-terminated BNRs. In contrast, pristine ZZ BNRs undergo severe structural distortions and become disordered after structural relaxation.

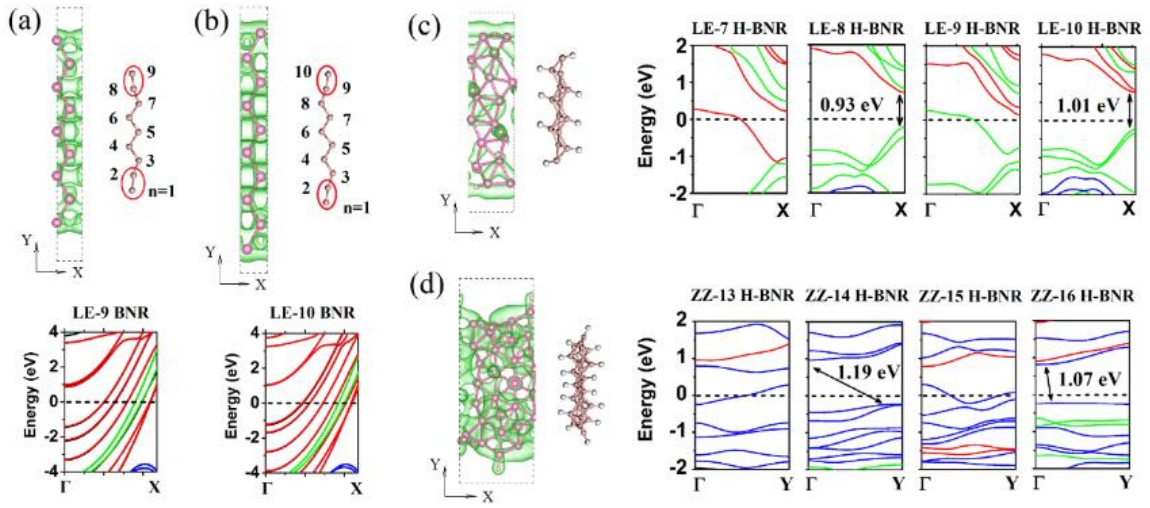

Fig. 4.3. The atomic model and the band structure of pristine (a) LE-9 and (b) LE-10 BNR. The top and side views of the atomic configurations, together with the charge distribution at the top of the valence band, are plotted in the upper panel. The atomic models of LE-8 and ZZ-15 H-BNRs with charge distribution for the states from E_f-1 eV to E_f are shown in the right panels of (c) and (d), respectively. The width-dependent odd-even oscillation of the band gap opening in LE and ZZ H-BNRs is shown in the left panels of (c) and (d), respectively. The blue, green, and red curves on the band structure plots represent the projected states for p_x, p_y, and p_z orbitals of the B atoms, respectively. The black dashed line shows the Fermi level.

Interestingly, the structural integrity is largely maintained for both H-functionalized LE (Fig. 4.3(c)) and ZZ (Fig. 4.3(d)) BNRs, which are created through cutting the 2D H-functionalized borophene, as shown in Fig. 4.1(b). The plots of the band structure show an odd-even oscillation of the band gap with the ribbon width for both H-functionalized LE and ZZ BNRs: the band gap is absent for odd H-functionalized BNRs but present for even H-functionalized BNRs. For instance, the band gap is 0.93 eV for LE-8 H-BNR while zero for LE-9 H-BNR. The band gap is 1.07 eV for ZZ-16 H-BNR but zero for ZZ-15 H-BNR. Therefore, depending on the width of the H-functionalized BNRs, the electronic states can

become partially localized and have a band gap opening, as supported by the isosurface plots of the partial charge density of the valence bands in Fig. 4.3. The orbital-resolved band structure plots (Fig. 4.3(c)) show that the frontier orbitals in LE H-BNRs are still p_y and p_z orbitals, similar to those in the pristine BNRs (Figs. 4.3(a) and (b)). For the ZZ H-BNRs, the frontier orbitals mainly consist of p_x components, as shown by the blue dispersion lines. The examinations of the charge density distribution of the LE-8 H-BNRs (Fig. 4.3(c)) show that such band gap opening in the specific type of H-BNRs is due to hydrogen-induced Peierls instability of the metallic states in the BNRs. This scenario is evidenced by the strong structural distortion of the BNR lattice and the tilted H-B bonds.

The investigation of the F-functionalized BNRs predicts that their electronic properties are insensitive to the ribbon width. Therefore, only one ribbon is selected as a representative for each of LE and ZZ BNRs. Figures 4.4(a) and (b) show the optimized atomic structure and the band structure of F-functionalized LE-10 and ZZ-16 BNRs, respectively. The orbital-resolved band structures show that F-BNRs remain metallic, as well as pristine BNRs. Different from the graphene case, where fluorination or ribbon construction can effectively open the band gap, the coexistence of fluorination and ribbon construction is not able to cause a metal-semiconductor transition, implying the robustness of metallicity in borophene. For the F-functionalized ZZ BNR, the in-plane p_y orbital of the B atoms is dominant at the Fermi level, which is different from the H-functionalized ZZ BNR with p_x as the frontier orbitals (Fig. 4.3(d)), suggesting that these functional groups can have a selective hybridization of the boron orbitals and alter the orbital population at the Fermi level.

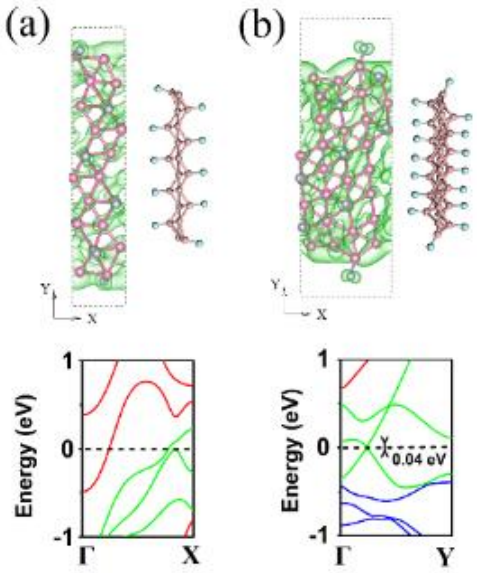

Fig. 4.4. (a) The atomic configuration and (b) the band structure of the F-functionalized BNRs. Integrated charge densities from E_f-1 eV to E_f are shown in (a, upper panel) LE and (b, upper panel) ZZ ribbons. The blue, green, and red curves in the band structure plots represent the occupation of the p_x, p_y, and p_z orbitals of B atoms.

To examine the stability of the considered structures, the average binding energy $E_{binding}$ of perfect, H- and F-functionalized borophene is calculated. The calculated values for the E_b for perfect, H- and F-functionalized borophene are 5.86, 4.78, and 5.25 eV, respectively. Clearly, all the three considered structures of the functionalized borophene show a better stability than the pristine borophene. To check the stability of the functionalized and vacancy-containing borophene, as well as the pristine and functionalized BNRs, AIMD calculations are performed. The snapshots of the simulation results are shown in Fig. 4.5. It is seen that during this long time (in terms of *ab initio* calculations), all the considered structures are stable. It should be noted that the ZZ H- and F- BNRs (Figs. 4.5(g) and (i)) exhibit a lower stability than the LE H- and F-BNRs.

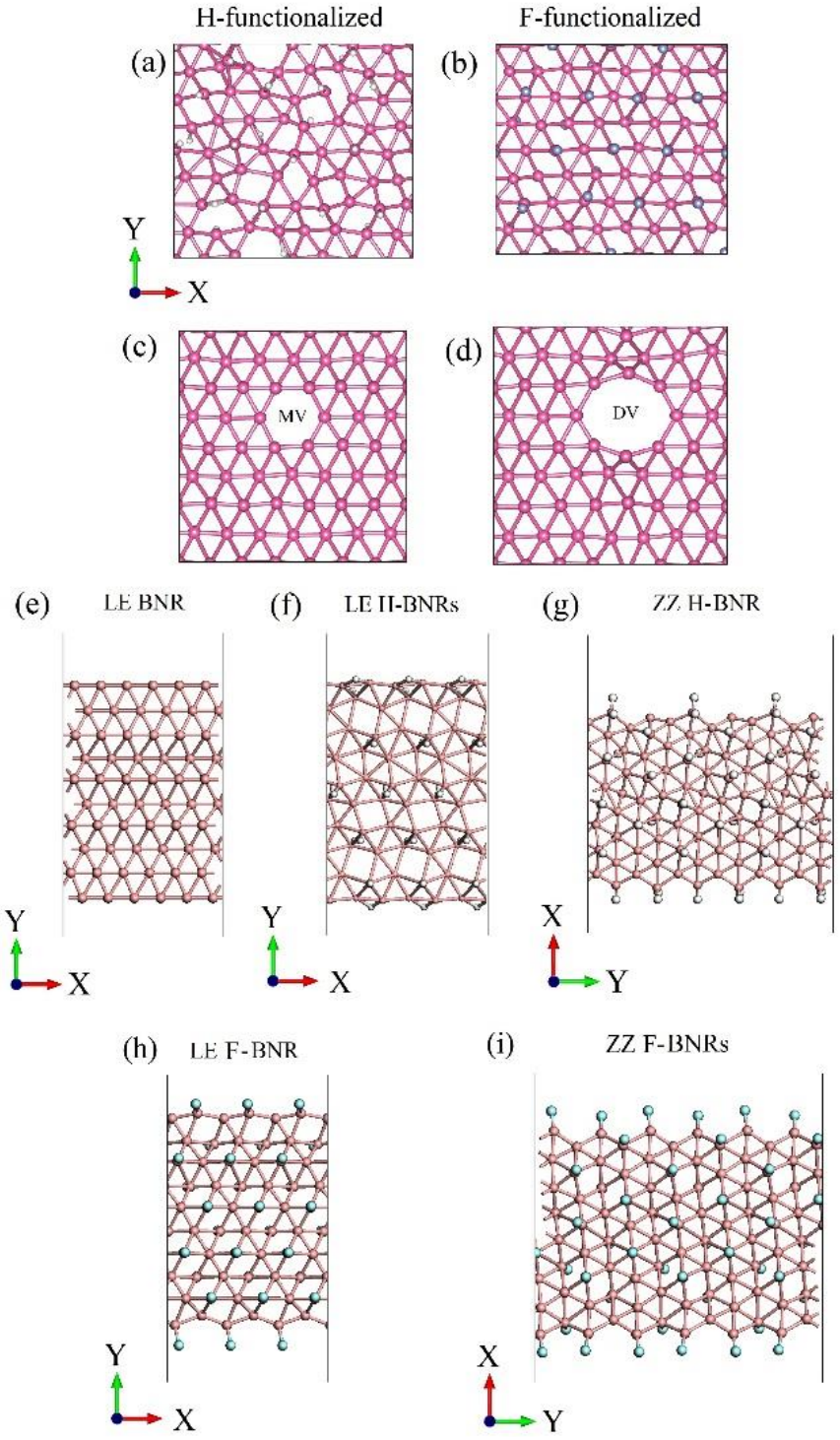

Fig. 4.5. The snapshots of the (a) H- and (b) F-functionalized borophene, (c) MV- and (d) DV-containing borophene, (e) LE, (f) LE H-, (g) ZZ H-, (h) LE F- and (i) ZZ F-BNRs calculated by AIMD at 300 K. Atoms B, H, and F are coloured in pink, white, and purple.

4.2 Atomic-scale mechanisms of defect- and light-induced oxidation and degradation of InSe

Oxidation plays a paramount role in affecting the integrity, property, and performance of materials. For instance, surface oxidation can make chemical catalysis inert [192], while it can also be used to modulate material properties, such as band gap opening of graphene [193]. In 2D materials, oxidation may lead to the structural degradation, thus decreasing their performance and impeding their applications [5]. For atomically thin 2D materials, two factors, light illumination [194] and atomic defects [149], are particularly eminent in affecting their oxidation in comparison with three-dimensional (3D) counterparts. The photo-induced effect tends to be pronounced in semiconducting layered materials due to their broadband photoresponse inherent in their tunable and quantum-confined electronic states [195]. The weak electronic screening in atomically thin materials often triggers a strong light-matter interaction [196]. In addition, 2D materials are also prone to forming atomic defects owing to their ultrathin sheets. Due to the break-up of lattice periodicity, redistribution of the electron density around defects core often occurs, rendering 2D sheets very active and sensitive to the environment [149, 190]. Phosphorene is a well-known example which shows a rapid oxidation due to chemical adsorption of O_2 molecules, photo-oxidation and defect-assisted oxidation [194].

InSe, a recently emerging layered metal monochalcogenide III-VI compound with each InSe layer composed of covalently bonded Se-In-In-Se atomic planes, has attracted great attention [197, 198], owing to its intriguing electronic properties and dramatically different behaviours compared with other 2D materials. For instance, in sharp contrast to

MoS_2 with the well-known direct (monolayer)-indirect (multilayer) transition, InSe has an opposite thickness-dependent behaviour with an indirect band gap for monolayer while a direct band gap for multilayer sheets when exceeding a critical thickness [199]. The thickness-dependent direct band gap of the thick InSe sheets allows a broad excitonic emission [200]. These unique properties trigger many studies on the growth [201, 202] and applications [203, 204] of InSe, for example, in optoelectronics, sensors, and photovoltaics. However, the performance of the InSe-based transistors at ambient conditions or under external fields has been found to be unsatisfying due to the degradation of their performance [205]. Its lone-pair states of the Se atoms at the top of the valence band of InSe induce high sensitivity to external adsorbates [206]. Previous experiments revealed that thinner InSe films tend to suffer from a more rapid degradation, largely in the form of oxidation, compared with bulk InSe [197]. Therefore, understanding the degradation mechanisms of InSe, which are predominantly involved with external adsorbates such as O_2 and H_2O at ambient conditions, is thus critically important for its practical applications. However, such understandings are still lacking. In particular, the knowledge of structure degradation arising from defect-environment-light coupling remains largely unknown. Therefore, in this section, the mechanisms of InSe oxidation is explored by using *ab initio* electronic structure calculations and *ab initio* molecular dynamics simulations.

4.2.1 Computational details

The considered structures are fully relaxed until the atomic forces are smaller than 0.01 eV/Å. To model the defective and gas-adsorbed InSe, as well as for AIMD simulations, a

4×4×1 supercell and the corresponding k-mesh is 10×10×1 are adopted. The plane-wave cut-off energy is 400 eV. A vacuum space with a thickness of 20 Å is introduced along the out-of-plane direction. Negatively charged the O_2 (O_2^-) molecule is introduced by adding one electron to the considered system. The Bader analysis [167] is used for the charge transfer calculations.

4.2.2 Results and discussion

Band alignment and indirect-direct gap crossover of few-layer InSe. Oxidation of a 2D material at ambient conditions can involve three chemical steps (Fig. 4.6(a)): adsorption of O_2 molecules, dissociation of O_2 molecules, and interaction of H_2O molecules with the anchored oxygen species. Before examining the light- and defect-assisted chemical dissociation of O_2 molecules on InSe, the electronic properties of pristine InSe and the mechanism of light-induced electron-hole pairs in InSe are studied. The band structure of monolayer InSe, calculated by the HSE method (as it was described in Section 4.1.1), is shown in Fig. 4.6(b) indicating an indirect band gap (E_g) of 2.12 eV. The striking feature of layered InSe is that for monolayer (1L) InSe and few-layer (nL) InSe with its layer number (n) below a critical value of (n_c), the CBM is always located at Γ point, while the position of the VBM is at the Λ point between the Γ and K points (refer to the band structures of 1L-4L InSe in Fig. 4.7). Above the n_c value (the exact value of n_c is still under debate: the experimental value n_c is equal to 7 at the critical thickness of 6 nm [207], but a theoretical result is n_c = 28 [208]), the few-layer and bulk InSe become a direct E_g. Figure 4.6(c) schematically shows this evolution of the band edges of few-layer InSe. The Λ point

gradually shifts towards the Γ point with an increase of the layer number and coincides with the Γ point upon $n > n_c$. The underlying reason for this phenomenon may originate from the interlayer coupling of the atomic lone-pair electrons between Se atoms in neighbouring layers. This indirect ($n < n_c$) to direct ($n > n_c$) transition behaviour is in sharp contrast to TMDs where only monolayer TMDs sheet has a direct E_g while few-layer one has an indirect E_g, suggesting different interlayer coupling mechanisms between InSe and TMDs.

The crossover to the direct gap for InSe sheets above the critical thickness n_c suggests that efficient light adsorption is favoured in multilayer InSe with more than n_c layers. However, for the indirect-gap InSe with $n < n_c$ layers, as the Λ point of the VBM is very close to the Γ point, light adsorption can still occur through phonon-involved excitations to remedy the momentum mismatch. Such a phonon-assisted process is schematically shown in the inset of Fig. 4.6(c). It has been shown that phonon-coupled phenomena can explain the luminescence of quantum wells and epitaxial layers [208]. In particular, for few-layer indirect-gap MoS_2, $MoSe_2$, and WSe_2, such a phonon-assisted process is able to lead to appreciable photoluminescence [209].

However, for few-layer MoS_2, the CBM lies around the middle of the Γ-K point and the VBM at Γ, implying a significant momentum mismatch, and thus the number of phonons eligible for such a process is quite limited. Herein, in monolayer and few-layer ($n < n_c$) InSe, the indirect-gap Λ point in the VBM is in the proximity of Γ, and thus the momentum mismatch is quite small. This allows a large number of long-wavelength flexural phonons to promote the light adsorption and trigger excitons. Indeed, significant excitation and strong light adsorption has been observed in monolayer and few-layer InSe [196, 199].

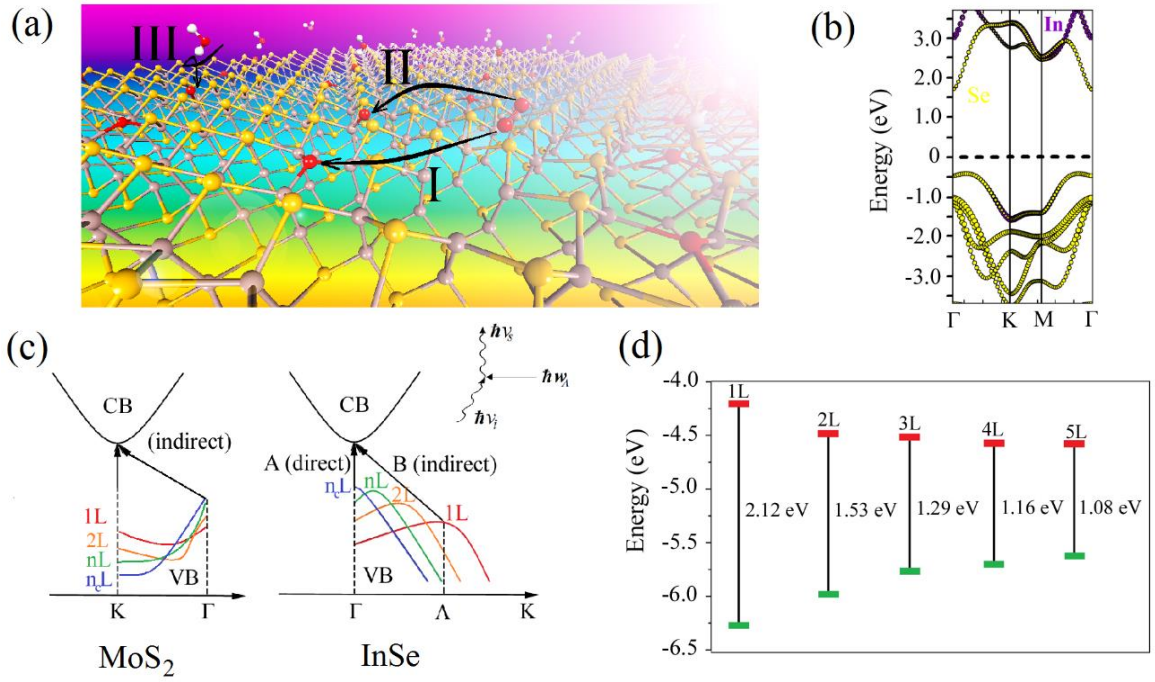

Fig. 4.6. (a) The schematic for the photo facilitated oxidation of InSe. Step I: Formation of superoxide anions ($O_2 + h\nu \rightarrow O_2^- + h^+$); Step II: Chemical dissociation of O_2^- into O atoms and oxidation of InSe; Step III: Adsorption of water molecules around the O atoms in the partially oxidized InSe. (b) The atomic projected HSE band structure for a perfect InSe sheet. (c) The schematic plot for the evolution of the valence band edges and the indirect-direct gap transition for InSe (right panel) and direct-indirect transition for MoS_2 (left panel) from 1L to *n*L, where *n* is the number of layers. Two different light adsorptions with "A" and "B" excitation for direct-gap layers ($n > n_c$) and indirect-gap layers ($n < n_c$), respectively. The inset shows the schematic process of the phonon ($\hbar\omega_\Lambda$, momentum Λ)-assisted light adsorption and emission in few-layer indirect-gap InSe with the incident ($\hbar\nu_i$) and scattered ($\hbar\nu_s$) photons. (d) Thickness-dependent band alignment of the VBM and CBM of few-layer InSe with respect to the vacuum potential.

Figure 4.6(d) shows the thickness-dependent position of the CBM and VBM for 1L-5L InSe aligned relative to the vacuum level (E_{vac}). The E_g decreases from 2.13 eV for monolayer InSe to 1.08 eV for 5L InSe with an upward (downward) shift of VBM (CBM).

The predicted widely tunable E_g may account for the observed broadband photoresponse in layered InSe [210]. In principle, upon light illumination, the photo-excited electrons can be transferred to the adsorbed O_2 molecules, thus affecting their adsorption and dissociation behaviour (refer to the schematic plot in Fig. 4.6(a)).

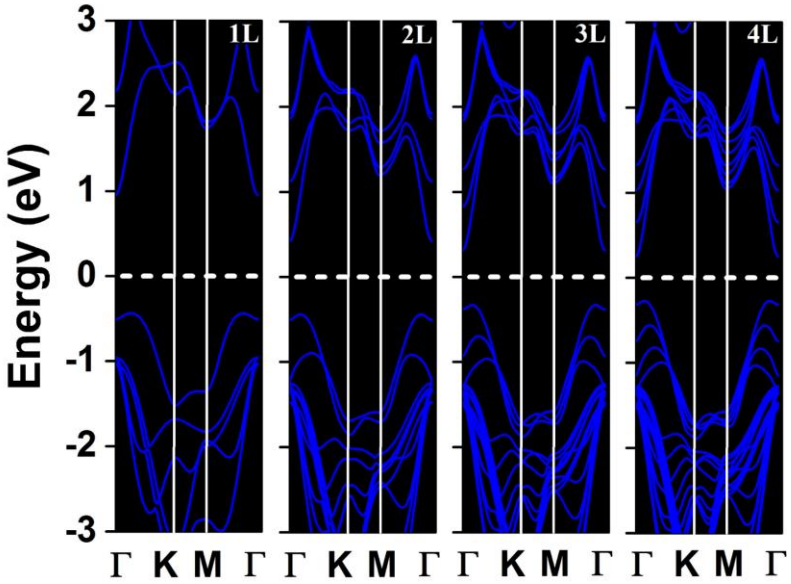

Fig. 4.7. Thickness-dependent band structures of InSe (from 1L to 4L) calculated by the GGA method.

Localized states of Se vacancies and molecular adsorption. Besides the light adsorption, intrinsic defects, like the atomic vacancies, can also influence the electronic properties and act as active sites for molecule adsorption. The most possible intrinsic defects, that is, the Se vacancies (V_{Se}) in InSe are examined. Figure 4.8(a) shows the DOS of perfect monolayer InSe together with those of the MV and DV in monolayer InSe. To highlight the V_{Se}-induced effects, all the DOS curves are plotted with the VBM of host InSe shifting to zero. Each loss of a Se atom in the InSe sheet creates three dangling bonds associated with

the unpaired orbitals of the three exposed In atoms. The unpaired orbitals in each MV V_{Se} evolve into the two defective states in the DOS: a lower-lying single "A_1" (occupied) state around 0.4 eV above the valence band and a doubly degenerated higher-lying "E" (unoccupied) state nearly coinciding with the conduction band edge. The two levels are named according to their symmetries in the irreducible representation of the local symmetry (C_{3v}) of the MV V_{Se}.

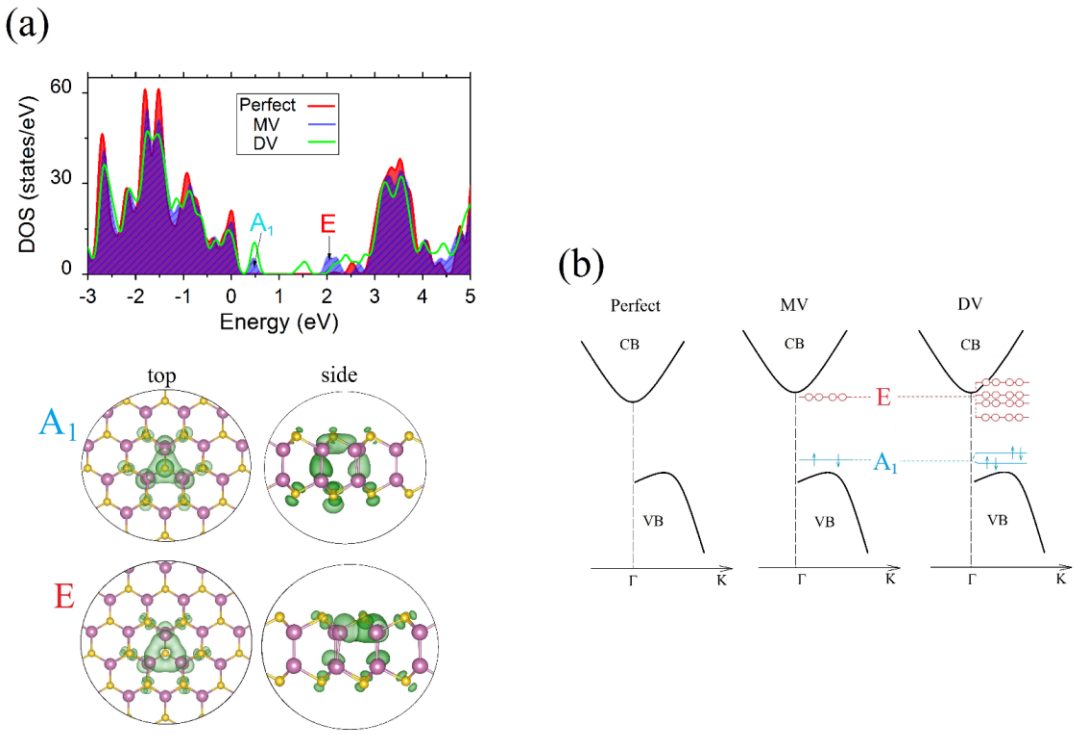

Fig. 4.8. The localized defective states associated with the V_{Se} in InSe. (a) The DOS of perfect and defective InSe containing MV and DV of Se atoms. All the energy levels are referenced to VBM of InSe. The A_1 and E correspond to the occupied and empty defective levels associated with MV V_{Se}, respectively. The inset shows the top and side views of the spatial distributions of the A_1 and E states around the MV V_{Se}. The In and Se atoms are coloured in purple and yellow, respectively. (b) The relationship and evolution of the defective levels of MV and DV.

The spatial distribution of both states is highly localized and plotted in the bottom panel of Fig. 4.8(a). It can be seen that both A_1 and E states are distributed across the top and bottom surfaces with significant impact on the In atoms. It is remarkable that the A_1 (E) is a bonding (antibonding) state of the middle In-In bond. With the removal of another Se atom neighbouring a pre-formed V_{Se}, a DV V_{Se} is thus formed, with more defective states than the MV case, which is reflected by the enhancement and broadening of peaks in the DOS plot in Fig. 4.8(a). The singly occupied "A_1" level of an MV V_{Se} evolves into two slightly split levels in the DV case whereas the degenerate pair of "E" level splits considerably into four levels, originated from the relatively strong coupling of the dangling states of the two V_{Se}. The evolution of the defective states at Γ from the MV to DV-containing InSe is schematically shown in Fig. 4.8(b). Exact alignment and positions of these defective levels are more clearly reflected by the comparison of the band structures of perfect, MV- and DV-containing InSe as plotted in Fig. 4.9(a).

It should be noted that to compare the band gap of perfect InSe with those of InSe with low defect concentrations, the band gaps of defective InSe are calculated by measuring the VBM and CBM related to the host InSe with the defective states being excluded. The calculations show that the band gap increases with the defect concentration growth. More specifically, perfect InSe has the smallest band gap of ~1.4 eV. With the increase of the vacancy concentration from 2 to 3.13 and further to 6.26 %, the band gap size increases from 1.52 to 1.55 and further to 1.68 eV, respectively. To facilitate the comparison of the defective states, the band structures of the different systems in Fig. 4.9(a) are all adjusted to align the VBM of host InSe. The presence of MV and DV V_{Se} increases the E_g of InSe by 0.16 and 0.33 eV, respectively, which can explain the experimental blue shift of the

photoluminescence peak after thermal annealing (~35 meV at 175 °C) [211]. It is expected that these defective states act as trapping and scattering centres for conducting carriers and decrease their electronic mobility.

The presence of defects on the surface of a material can greatly modify its physical properties in terms of energetics, kinetics and charge transfer during gas adsorption [149, 190]. Hence, the effects of V_{Se} on the adsorption energy E_a (calculated as it is shown in Section 3.1) are considered (compiled in Table 4.1). The charge transfer analysis shows that the O_2 and H_2O molecules are molecular acceptors for both the perfect and V_{Se}-containing InSe (refer to the differential charge transfer plots in Figs. 4.9(b) and Figs. 4.10(a) and (b)). Compared with the adsorption on perfect InSe (Table 4.1), the presence of MV V_{Se} triggers a much larger effect on the H_2O molecule than on the O_2 molecule: the E_a changes from -0.17 eV (perfect InSe) to -0.41 eV (V_{Se} site) for H_2O, while there is almost no change in the E_a for the O_2 (-0.10 eV) molecule. Similarly, for the Se-deficient InSe, the H_2O molecule has a significantly enhanced oxidization ability compared with the perfect surface as judged from the amount of charge transfer between the molecule and the surface. For the H_2O molecule, the amount of charge transfer is more than four times larger at the V_{Se} site (-0.09 e) than at the perfect surface (-0.02 e), while for the O_2 molecule, the charge transfer (around -0.03 e) is almost insensitive to the presence of V_{Se}.

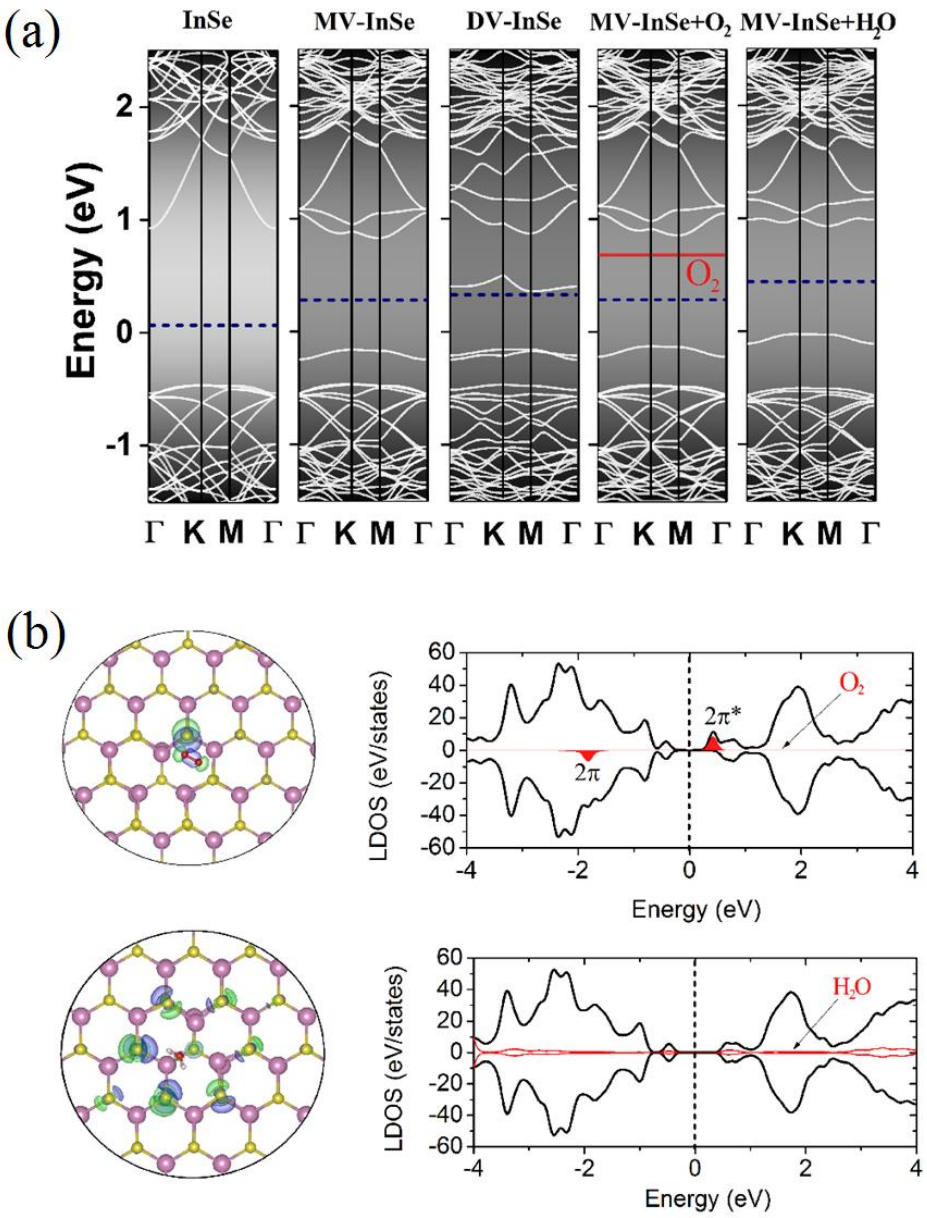

Fig. 4.9. (a) The comparison of the band structures (GGA method) of perfect monolayer InSe, V_{Se}-containing InSe (MV and DV), and O_2/H_2O physisorbed MV-InSe. It should be noted that all the bands in different systems are shifted to align with VBM of the host InSe. (b) The isosurface plots of the differential charge density after O_2/H_2O physisorption, where the green/blue colour denotes depletion/accumulation of electrons (left panel) and DOS for O_2/H_2O molecule adsorbed on the V_{Se} site (right panel) with the Fermi level (dashed line) aligned at zero. States of O_2/H_2O (total system) are denoted by the red (black) lines.

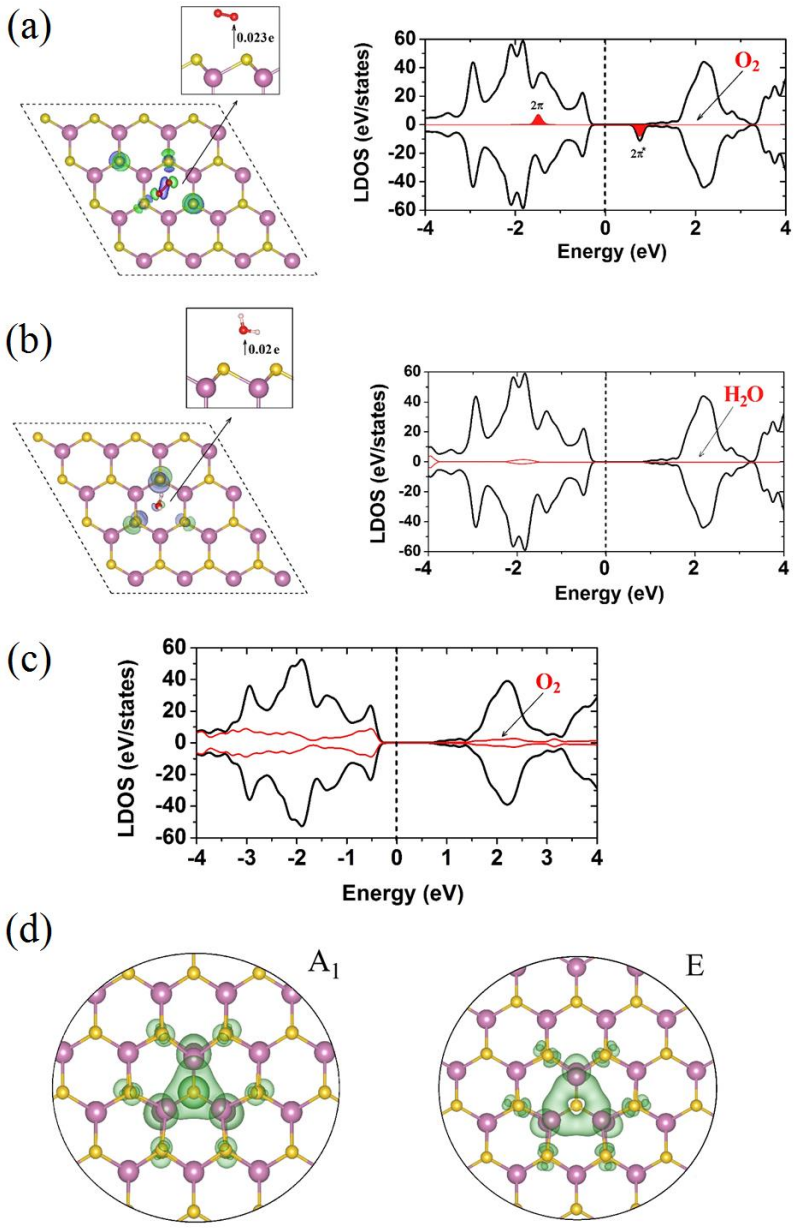

Fig. 4.10. The adsorption of the O_2 (a, left panel) and H_2O (b, left panel) molecules on perfect InSe. The LDOS for the O_2 (a, right panel) and H_2O molecules (b, right panel) adsorbed on perfect InSe with the Fermi level (dashed line) aligned at zero. States of O_2/H_2O (total system) are plotted by the red (black) lines. (c) The LDOS for the O_2 molecule chemisorbed at the V_{Se} site of InSe. (d) The isosurface plots of the differential charge density after O_2/H_2O physisorption on perfect InSe, where the green/blue colour denotes depletion/accumulation of electrons (left panel).

Table 4.1. The adsorption energy E_a for physisorption of H_2O and O_2 molecules and the charge transfer Δq from these molecules to perfect and defective InSe sheets. A positive Δq indicates the transfer of electrons from the molecules to the surface.

Structure	Adsorbate	E_a (eV)	Δq *(e)*
Perfect InSe	H_2O	-0.17	-0.020
	O_2	-0.12	-0.023
MV-containing InSe	H_2O	-0.41	-0.090
	O_2	-0.10	-0.027
Preoxidized perfect InSe	H_2O	-0.33	-
Preoxidized MV-containing InSe	H_2O	-0.34	-

The band structures and DOS of O_2 and H_2O adsorbed on the MV V_{Se} site (Fig. 4.10) are shown in Figs. 4.9(a) and (b), respectively. Upon being adsorbed around the V_{Se} centre, the O_2 takes a parallel geometry and H_2O adopts a tilted configuration with the two H-O bonds pointing away from the surface. The LUMO state ($2\pi^*$) of the O_2 molecule is slightly below the empty "E" defective level, suggesting that any captured electrons in this defective level can be easily transferred to the O_2 molecule. For the H_2O molecule, there is no H_2O related state within the band gap of InSe. However, the presence of V_{Se} makes the highest occupied molecular orbital (HOMO) state ($1b_1$) of H_2O significantly downward shifted by ~2.2 eV compared to the adsorption on the perfect InSe (Fig. 4.10(b)). This may be the underlying reason for the above-mentioned large differences in the E_a and the charge transfer for adsorptions of H_2O on the V_{Se} site compared with perfect InSe.

Chemical dissociation of O_2 molecules and the effect of H_2O molecules. Next, the kinetics of the O_2 molecule dissociation on the InSe is investigated. The detailed reaction path (calculated as it is shown in Section 3.1) and the corresponding energetic profile for the O_2 decomposition during the surface oxidation are shown in Fig. 4.11. The oxidation process is found to be exothermic and the barrier is strongly dependent on the surface stoichiometry

of InSe and the charging state of the adsorbed O_2 molecule. The calculated barrier E_b for the dissociation of O_2 on perfect InSe is found to be 1.21 eV (Fig. 4.11(b), blue line). This value is significantly higher than that of the O_2 chemisorption on phosphorene with E_b=0.56 eV [189] and on MoS_2 with E_b=0.74 eV [149], suggesting a higher chemical stability of InSe against oxidation than phosphorene and MoS_2.

Upon light excitation, the O_2 molecule becomes superoxide anions and the E_b is significantly reduced to 0.84 eV for the O_2^-. According to the rate theory (details are in Section 3.2.3), it is expected that the drop of E_b from 1.21 to 0.84 eV implies a 7-order higher oxidation rate. On the contrary, the barrier for the O_2^+ molecule increases to 1.32 eV. As shown in Fig. 4.11(a), starting from the physisorbed initial state (IS), the bond length of the O_2 molecule gradually increases and finally breaks. In the final state (FS), the two oxygen atoms adopt bridging configurations by forming In-O-Se and In_2-O-Se structures separately (It should be noted that the plotted atomic configurations are based on neutral O_2 calculation).

The case of O_2^- undergoes similar structural transformations (Fig. 4.12). It should be noted that upon light illumination, the hole-doped monolayer InSe is not simulated in the calculations. In reality, the generated hole population within the InSe sheet and the superoxide anions at the surface may induce an electric field near the InSe surface region, which can make the barrier even smaller. Therefore, the obtained results may explain the poor structural stability and unsatisfying mobility of the unpassivated InSe in the MOS architecture where the vertical field has been created through applying gating voltage [197].

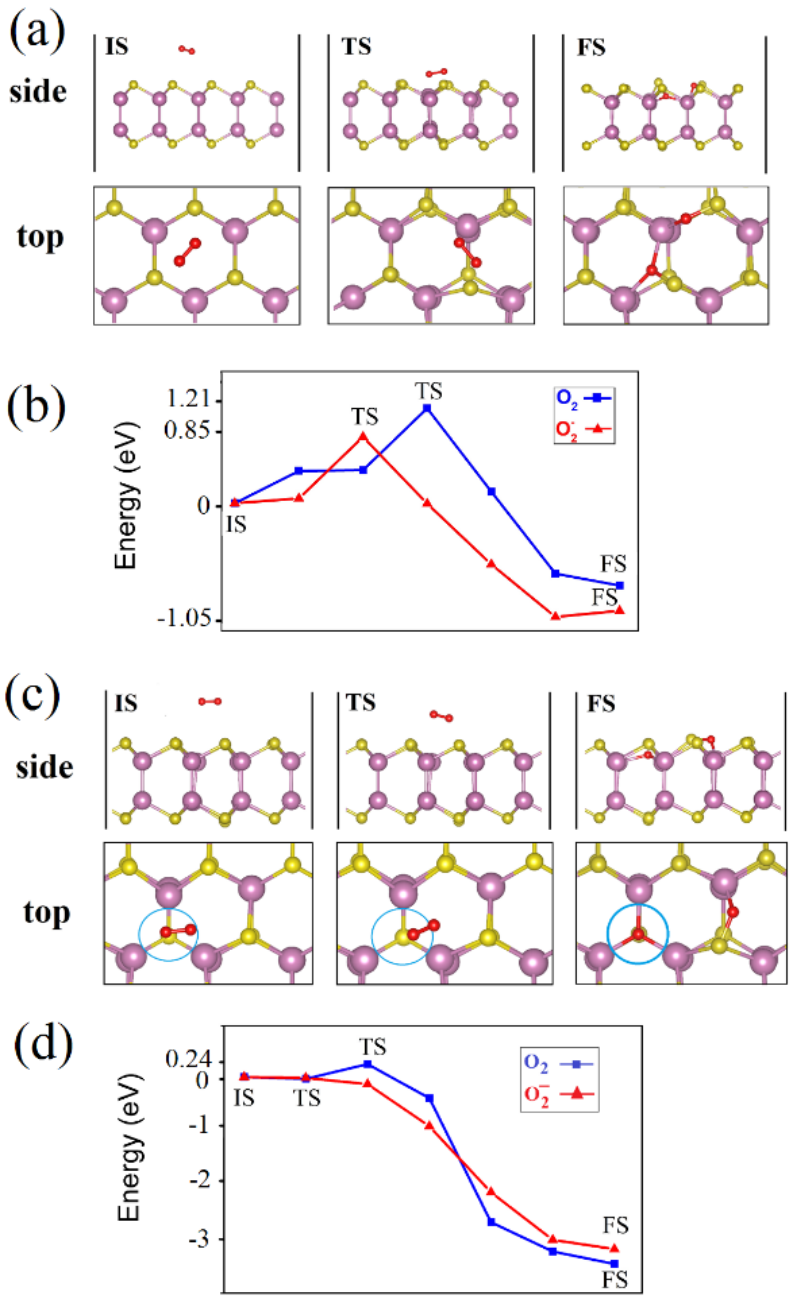

Fig. 4.11. The chemical dissociation of the O_2 molecule on (a) and (b) perfect and (c) and (d) MV-V_{Se}-containing InSe. (a) and (c) The atomic configurations from the physisorbed to the chemisorbed state in the dissociation process of O_2. (b) and (d) The energetic profiles of the reaction pathway. The IS, TS, and FS represent the initial, transition, and final states, respectively. The In, Se, and O atoms are coloured in purple, yellow, and red, respectively. The position of the V_{Se} is represented by the circle in (c).

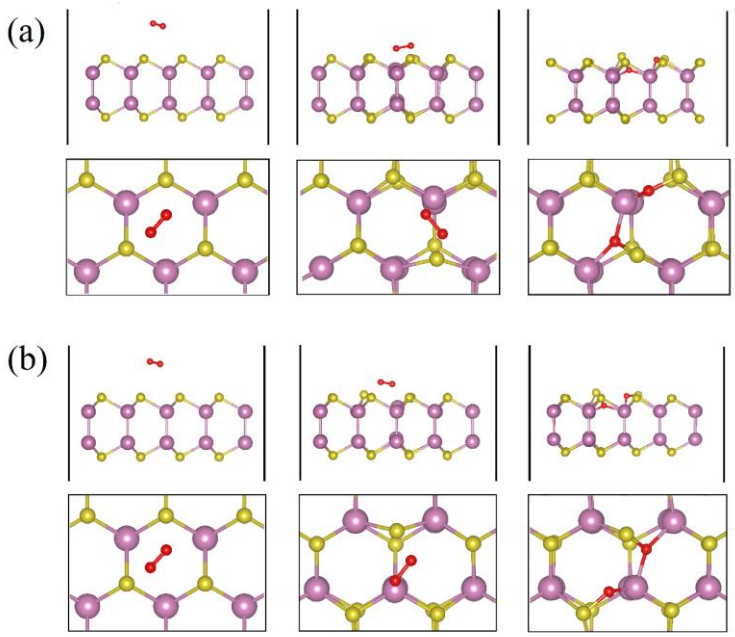

Fig. 4.12. The atomic configurations from the physisorbed to the chemisorbed state in the dissociation process of (a) O_2 and (b) O_2^- on the perfect InSe sheet. The In, Se, and O atoms are coloured in purple, yellow, and red, respectively.

Surprisingly, with the introduction of a single V_{Se} in the InSe sheet, as shown in Figs. 4.11(c) and (d), the E_b is dramatically reduced to 0.24 eV. This ultralow barrier suggests that the O_2 molecule can easily dissociate at the V_{Se} site even at a moderate temperature and the Se-deficient InSe becomes easily oxidized at ambient conditions. The mechanism of the promoted activity may originate from the following reasons. Firstly, the loss of Se atoms allows the exposure of the In atoms to oxygen where a direct transfer of unpaired excess electrons of In to the $2\pi^*$ antibonding state of O_2 molecule is. Secondly, by contacting the strong electropositive In atoms with the strong electronegative O atoms, the formation of In-O bonds in the FS is accompanied by a strong release of energy. The energy difference of the TS and IS in the MV V_{Se}-containing InSe achieves up to ~3 eV per O_2 molecule (Fig.

4.11(d)), which is nearly three times of the energy release of ~1 eV in the case of perfect InSe (Fig. 4.11(b)). Finally, the 4d state of the exposed In atoms at the vacancy site may also facilitate the spin triplet-singlet transition of the O_2 molecule, which can contribute to the low barrier of the O_2 dissociation. With the coexistence of light and V_{Se}, the E_b can be further reduced and become almost negligible for the photo-reduced O_2 molecule (O_2^- molecule, red line in Fig. 4.11(d)), undergoes similar structural transformations (Fig. 4.13), suggesting that under a proper light illumination or charge injection, the oxidation rate of InSe can dramatically increase even at room temperature.

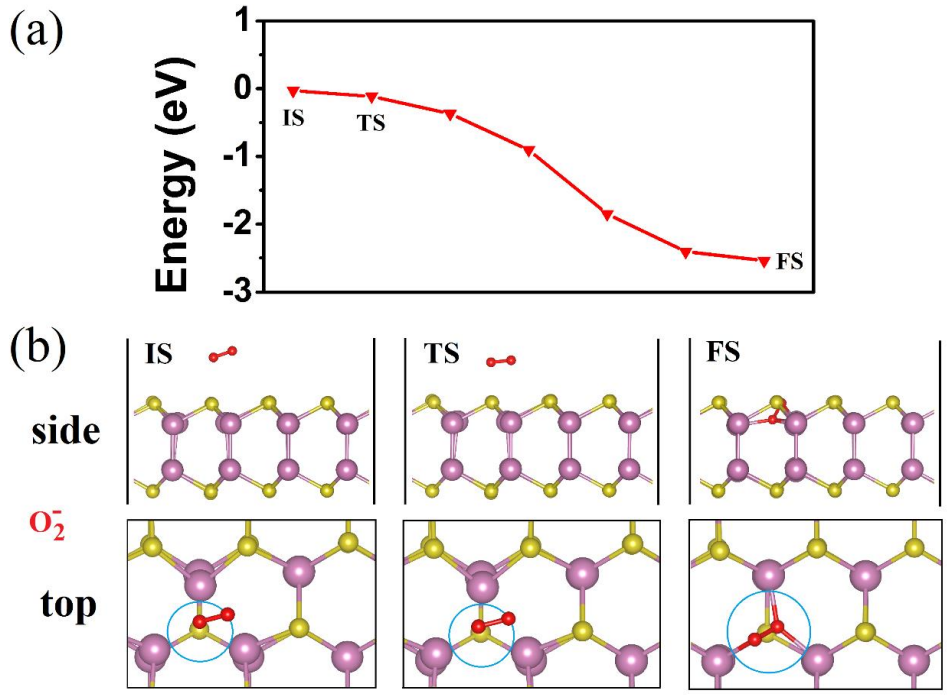

Fig. 4.13. (a) The atomic configurations from the physisorbed to the chemisorbed state in the dissociation process of O_2^-. (b) Chemical dissociation of the O_2^- molecule on MV-V_{Se} containing InSe and energetic profiles of the reaction pathway. The IS, TS, and FS represent the initial, transition, and final states, respectively. The In, Se, and O atoms are coloured in purple, yellow, and red, respectively. The position of the V_{Se} is represented by the circle.

There are two consequences arising from the chemical dissociation of the O_2 molecule on the InSe surface: the first one is related to the electronic properties. Upon the formation of the In-O-In structures in the Se-deficient InSe sheet (the TS structure shown in Fig. 4.11(c)), the defect state due to V_{Se} is quenched (LDOS in Fig. 4.10(c)). This may affect the optical properties via suppressing non-radiative recombination at the vacancy site and increasing the quantum efficiency. The second one is related to those embedding O atoms in InSe. Under ambient conditions, the bridging O atoms with In-O-In or In-O-Se bonding configurations or apical O atoms in forming O-Se vertical groups in the sheet may affect the adsorption of the polar molecules, like H_2O, on the InSe surface.

Next, the AIMD calculations are performed to further investigate the adsorption of the H_2O molecule by focusing on the pre-adsorbed O species on InSe. The kinetics of the H_2O molecule on three different InSe surfaces with different stoichiometric and oxidizing conditions are compared: i) the perfect InSe without V_{Se} and O groups, ii) the partially oxidized InSe without V_{Se}, and iii) the partially oxidized InSe with V_{Se}. The surface models for the last two cases correspond to the end states of the NEB calculations shown in Fig. 4.11. The cumulative distance d_a is analyzed for the atom a at the i^{th} MD step along the path l_a:

$$d_a(N_i) = \int_{N_0}^{N_i} dl_a \, F \tag{4.5}$$

This analysis allows the differentiation of the kinetic motion characteristics of H_2O. The cumulative distances and the trajectories of the O atom and one of the H atoms in the H_2O molecule for the three cases are shown in Fig. 4.14. For perfect pristine InSe, the

trajectory (inset of Fig. 4.14(a)) of the H_2O molecule clearly shows a random walking behaviour, which is also evidenced by the simulated snapshots in Fig. 4.15.

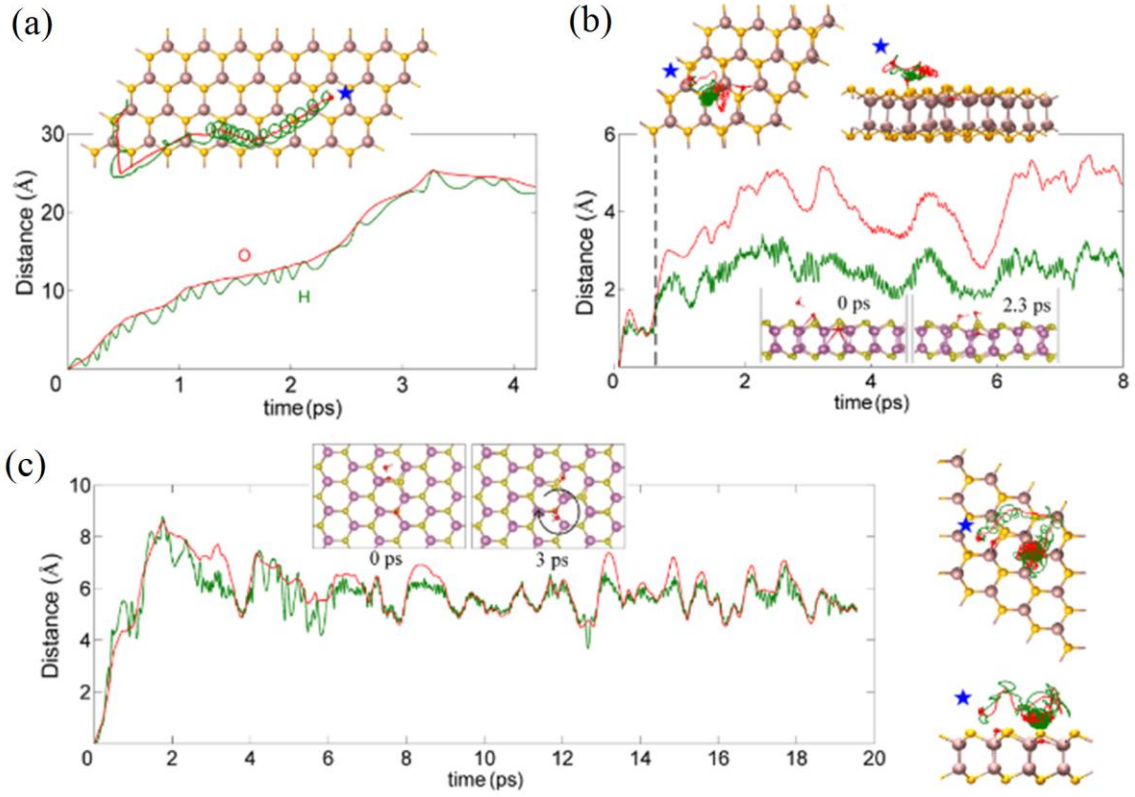

Fig. 4.14. The kinetics of the H_2O molecule on the InSe surface calculated by AIMD simulations at 300 K. The cumulative distance of the O atom (red curve) and one of the H atoms (green curve) in the H_2O molecule adsorbed on perfect InSe (a), partially oxidized InSe without V_{Se} (b) and with V_{Se} (c). The trajectories of the O (red curve) and H (green curve) atoms diffusing on the InSe surface are shown in the insets. The blue stars in the trajectory plots indicate the starting point of the H_2O molecule. AIMD snapshots in the insets of (b) and (c) show the splitting and the rotation of the H_2O molecule, respectively.

For the two partially oxidized InSe surfaces, that is the pre-oxidized stoichiometric InSe (Fig. 4.14(b)) and pre-oxidized Se-deficient InSe surfaces (Fig. 4.14(c)), the kinetic

behaviour of the H_2O molecule becomes significantly different, depending on the type of the O groups on the surface. It should be note that the H_2O molecule is initially positioned around the O group (with a distance around 3.5 Å) with only van der Waals interaction in order to reduce the computational time in sampling the phase space for the interaction of H_2O with the adsorbed O atoms.

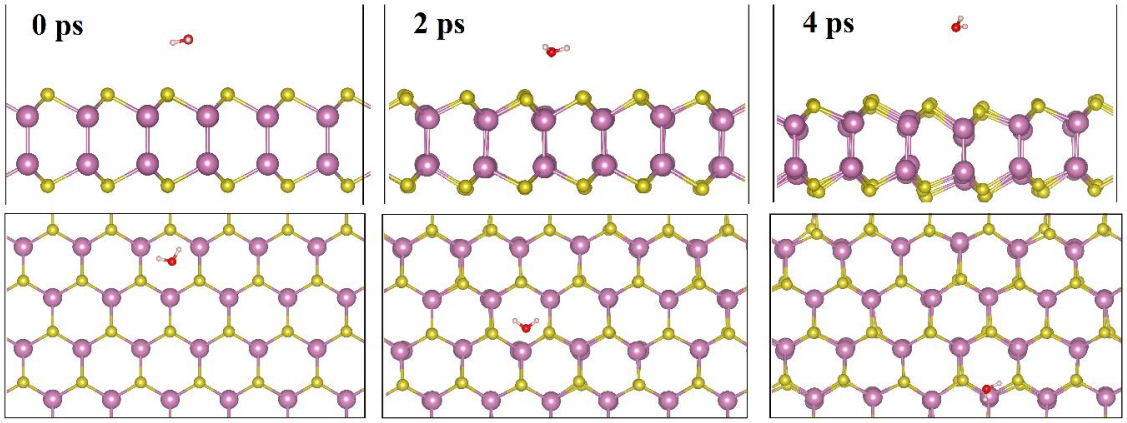

Fig. 4.15. The snapshots of the motion of water molecule on perfect InSe calculated by AIMD at 300 K. The O, H, In, and Se atoms are coloured in red, white, purple, and yellow, respectively.

For the pre-oxidized InSe without V_{Se} (Fig. 4.14(b)), the H_2O molecule initially interacts with the terminated O atom in the apical Se-O group normal to the surface. Subsequently, the H_2O molecule moves around the O atom. Interestingly, one of the O-H bonds in the water molecule is torn apart at 2.3 ps (the bottom right inset of Fig. 4.14(b)). This is accompanied by the formation of two H-O-Se groups, signifying a spontaneous dissociation of the water molecule around the terminated O atoms. This bond breaking in H_2O can be clearly seen from non-overlapping cumulative distance curves of the H and O

atoms shortly after the adsorption (the vertical dashed line in Fig. 4.14(b)). The trajectory plots also record this splitting with the H atom (green line) moving in the proximity of the terminated O atom on the InSe surface, while the left O (red line) and H (not shown) atoms in the initial H_2O molecule gradually diffuse away. In contrast to the O_2 molecule, direct dissociation of H_2O at the Se vacancy is impossible at a moderate temperature due to a large energy barrier of ~2.9 eV (Fig. 4.16).

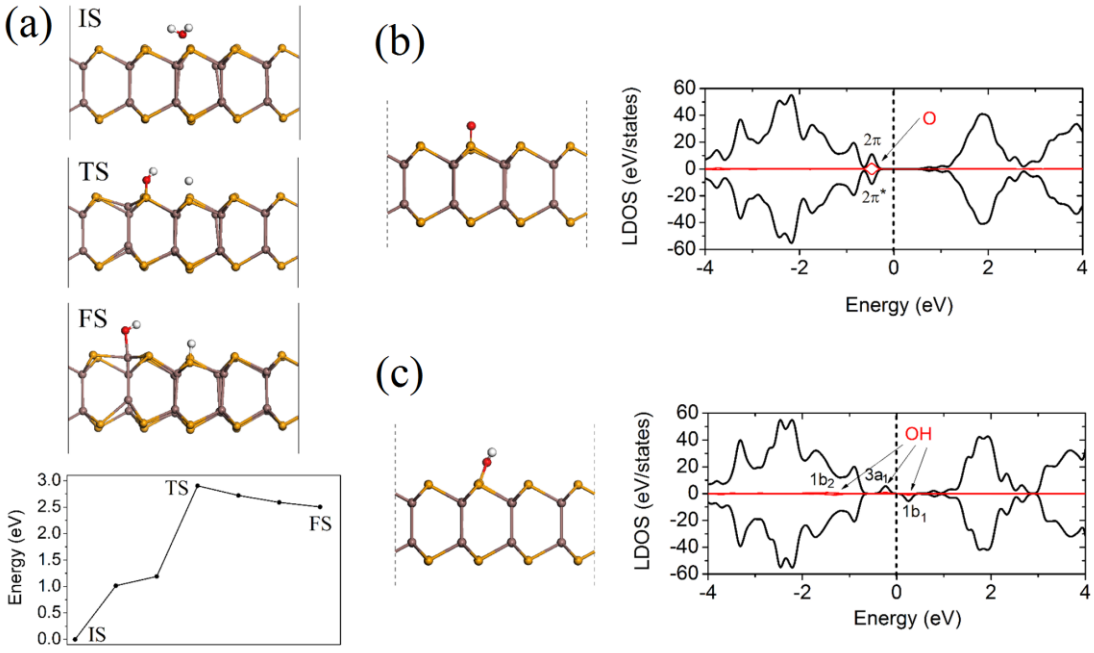

Fig. 4.16. (a) The chemical dissociation of H_2O molecule on MV-V_{Se}-containing InSe. Upper panel: Atomic configurations from the physisorbed to the chemisorbed state in the dissociation process of H_2O. Lower panel: The energetic profiles of the reaction pathway. The IS, TS and FS represent the initial, transition, and final states, respectively. In, Se, H and O atoms are coloured in purple, yellow, white and red, respectively. Atomic configuration and LDOS for (b) O and (c) OH defects on the perfect InSe surface with the Fermi level (dashed line) aligned at zero. States of O/OH (the total system) are denoted by the red (black) lines.

The AIMD simulations clearly show that besides the atomic oxygen species, the hydroxyl groups are also present on the InSe surface at ambient conditions (Fig. 4.17). Moreover, at ~7 ps, one of the Se atoms bonded with O and H atoms is lifted off the surface by the outward dragging of the H-O group. However, the stability of the InSe structure is maintained with no disintegration in subsequent MD simulation in a longer timescale (Fig. 4.17(a)). The In atomic layer, which is behind the next layer of Se atoms, is also kept intact during the simulation.

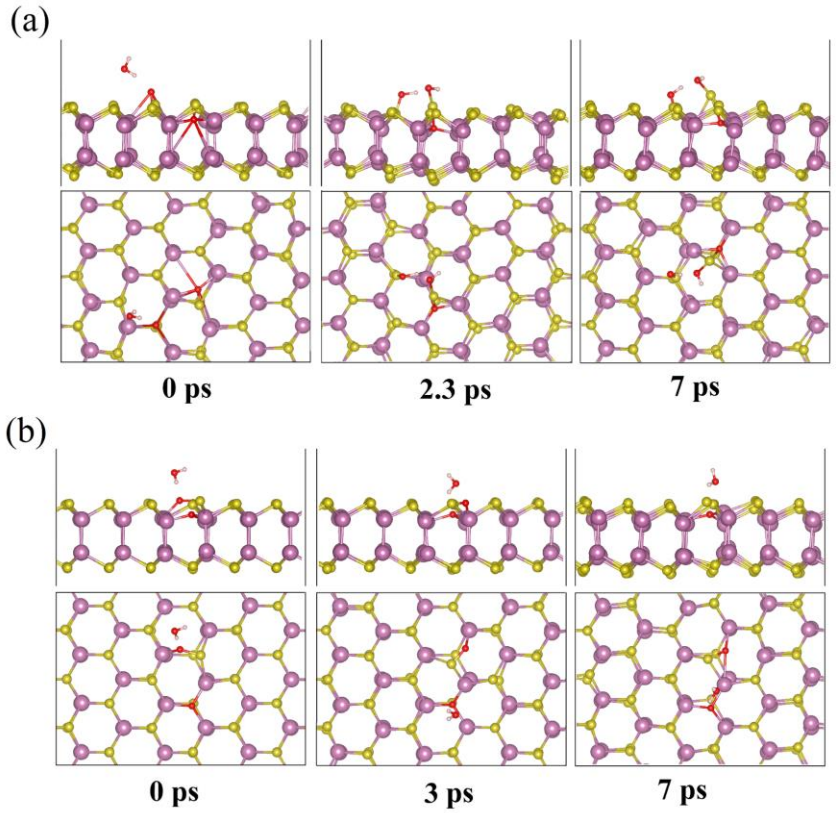

Fig. 4.17. The snapshots of AIMD simulations of H_2O on pre-oxidized (a) perfect and (b) MV-containing InSe at 300 K. The O, H, In, and Se atoms are coloured in red, white, purple, and yellow, respectively.

For chemically bonded -O and -OH groups above perfect InSe, defective states close to the valence band of InSe are introduced (Fig. 4.16), serving as carrier trapping centres. The adsorptions also induce *p*-type doping in InSe with charge transfer of 0.27 and 0.17 *e* from the InSe surface to O and OH, respectively, amounting to 1.16×10^{12} and 0.73×10^{12} e/cm^2 according to current used atomic model with the O and OH coverage of 6.25% (Fig. 4.18).

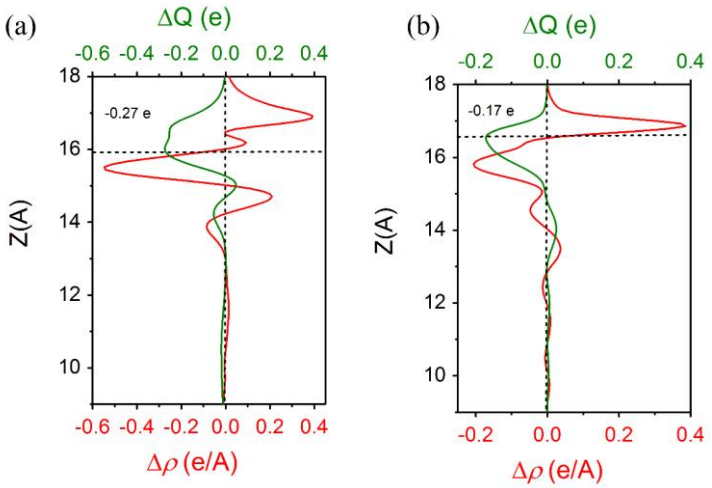

Fig. 4.18. The plane-averaged DCD $\Delta\rho(z)$ (red line) and the amount of transferred charge $\Delta Q(z)$ (green line) for (a) O and (b) OH defects on the perfect InSe surface.

Figure 4.14(c) shows the motion of the H_2O molecule above the pre-oxidized Se-deficient InSe. As aforementioned in Fig. 4.11(c), there are two oxygen atoms occupying different local environments with one forming the O-$[In]_3$ group and the other one forming the In-O-Se group. The H_2O molecule is initially placed around the In-O-Se group (see the snapshot at 0 ps in the top left inset of Fig. 4.14(c)). This type of the O atom seems to have a weak effect and the water molecule moves randomly until it meets with the second O atom

in the O-$[In]_3$ group at ~3 ps (see the snapshot in the top right inset of Fig. 4.14(c)). The H_2O molecule is trapped by this O atom and rotates strictly around it during the simulation time up to 20 ps. The trajectory plots with predominant lower-lying H atom which is close to the embedding O group suggest that the interaction mainly involves weak hydrogen bonding. The findings predicted here suggest that the presence of the atomic O group on the InSe surface can dramatically change the adsorption behaviour of the water molecule. Controlling the type of the O groups like the in-plane O-$[In]_3$ group can enhance the adsorption of H_2O and increase the hydrophilicity of the surface.

4.3 Adsorption of small molecules on antimonene: Oxidation tendency and stability

Recently, for the first time, antimonene, which is a monolayer of antimony, has been predicted by DFT calculations [212]. Subsequently, a high-quality antimonene sheet has been obtained by mechanical exfoliation of bulk antimony [213]. Importantly, antimonene exhibits a high mechanical stability [213] and unique thermodynamic stability at ambient conditions [214], in strong contrast to the poor stability of phosphorene. Antimonene also possesses a buckled structure, a wide indirect band gap of 2.28 eV, and high carrier mobility [215]. A previous theoretical study has suggested that external strain can be used to tune antimonene from an indirect to a direct band gap semiconductor [216]. Therefore, due to its tunable wide band gap, anisotropic carrier mobility, excellent optical and thermoelectric response and high structural stability at ambient conditions [217], layered antimonene is

promising for various potential applications [217, 218], such as sensors, spintronics, and energy storage devices.

Due to the high sensitivity to the external adsorbates including environmental molecules and dopants, 2D materials, particularly phosphorene, undergo structural degradation upon exposure to oxygen and water molecules [13, 219]. External molecules and dopants can also enhance electronic properties and chemical activities of 2D materials by donating electrons/holes or by altering the work function of the host material [141, 142]. For instance, surface patterning of MoS_2 with hydrogen may provide an effective way to create a metallic nanoroad for interconnection [220]. Selective surface decoration by molecules, such as NO, NO_2, and O_2, and typical charge-transfer organic molecules may cause alteration of carrier density, the shift of the Fermi level and even the change in the optical properties of many 2D materials [13, 221]. To apply the novel layered antimonene for nanoelectronic and chemical applications, a comprehensive understanding of its interaction with many common environmental molecules is highly desired. However, effects of environmental molecules on the carrier density in antimonene and tendency of charge flow across their interfaces are still unknown.

In this section by using first-principles calculations, the effects of physisorption of several small molecules, including CO, NO, NO_2, H_2O, O_2, NH_3, and H_2, on the electronic properties of monolayer antimonene are studied. A thorough analysis of the charge transfer across molecular adsorbate-antimonene interfaces is carried out. In particular, the stability issue of antimonene under the environmental oxygen and water molecules is examined and discussed from the atomic scale. This topic has not been discussed before and is critically important for the synthesis, storage, and applications of antimonene.

4.3.1 Computational details

The relaxed lattice constants of monolayer antimonene are $a = b = 4.308$ Å and the calculated band gap is 1.14 eV (GGA method), which is consistent with the results of recent works [222, 223]. To consider the effects of molecular adsorbates in the dilute doping limit, we place the molecule on an antimonene sheet consisting of a 4×4×1 supercell (32 Sb atoms). To avoid the interaction between the replicate units, a vacuum space of 20 Å is applied. The kinetic energy cut-off is set to 450 eV. The first Brillouin zone is sampled with a 6×6×1 k-mesh grid. The charge transfer analysis is conducted by the calculation of the DCD $\Delta\rho$(r) as it is described in Section 3.1.

4.3.2 Results and discussion

The influence of small molecules CO, NO, NO_2, H_2O, O_2, NH_3, and H_2 on the electronic properties and chemical activities of antimonene is considered. The adsorption energy E_a and charge transfer between the antimonene surface and these molecules are systematically investigated. For each molecule, several different configurations and possible adsorbing sites are considered, including the top of the Sb site, the top site above the centre of the hexagon, and the top site above the Sb-Sb bond with the molecules being aligned tilted, parallel or perpendicular to the surface. The random adsorption inside the hexagon is tested and it is revealed that those adsorbing configurations become similar to one of the mentioned three cases, but with slightly higher adsorption energy. The results of E_a, the charge transfer Δq and the shortest distance d from the molecule to the Sb atom for the lowest-energy configuration are summarized in Table 4.2.

CO adsorption. The most stable configuration and the DCD isosurface plot for the CO molecule adsorbed on antimonene are shown in Fig. 4.19(a). The molecule adopts a tilted configuration above the centre of the hexagon with d = ~3.72 Å and E_a = -0.12 eV. The DCD isosurface plot (Fig. 4.19(a)) clearly reflects an accumulation of electrons in the region around the C atom, indicating a loss of electrons in the proximity of the antimonene sheet. This is not surprising since elemental C is more electronegative than Sb. Quantitative DCD $\Delta\rho$(r) analysis (Fig. 4.19(b)) reveals that only a tiny amount of electrons are transferred from antimonene to the CO molecule (-0.003 e per molecule), which is consistent with the almost unchanged C-O bond length compared with that of the isolated gas molecule. Interestingly, the values of d and $E_{a,}$ and the charge transfer ability of the CO molecule adsorbed on antimonene are similar to those of the CO molecule on InSe [206], while significantly different from those for the CO molecule adsorbed on graphene [141] and phosphorene [13]. This similarity of the CO molecule behaviour on antimonene and InSe can be attributed to their similar honeycomb structure with the lone-pair electrons associated with Sb or Se atoms.

The band structure of antimonene adsorbed with the CO molecule (Fig. 4.19(c)) clearly shows that there are no additional CO-induced states within the band gap of antimonene. The value of the band gap is almost unchanged compared with that of pristine antimonene (1.14 eV). The LDOS plot (Fig. 4.19(d)) shows that the HOMO 5σ and the LUMO $2\pi^*$ of the CO molecule adsorbed on antimonene are located at -4.30 and 2.10 eV (relatively to the Fermi level), respectively. It should be noted that the HOMO level is a non-resonant state located below the valence band of antimonene, while the LUMO level is located within the conduction band. The $2\pi^*$ peak is significantly broadened compared with the 5σ level, which

is opposite to the case of CO above InSe [206]. This alignment of CO LUMO states within the conduction band of antimonene suggests that the photo-excited electrons of antimonene may partially transfer to the CO LUMO state, which can trigger different electron-hole recombination rates and prolong the lifetime of holes in the antimonene sheet upon exposure to the CO gas. On the other hand, the enhanced occupation of this antibonding orbital should weaken the C-O bond and affect its infrared frequency, which would allow the monitoring of the population of photo-excited carriers in antimonene.

Table 4.2. The adsorption energy E_a, the amount of charge transfer Δq, the shortest distance d from the molecule to the Sb atom, and the donor/acceptor characteristics of the molecular dopant on the antimonene surface. A positive (negative) Δq indicates a loss (gain) of electrons from each molecule to antimonene.

Molecule	*Antimonene*				*Phosphorene* *[Ref. 13]*		*InSe* *[Ref. 206]*	
	d (Å)	Doping nature	E_a (eV)	Δq (*e*)	E_a (eV)	Δq (*e*)	E_a (eV)	Δq (*e*)
CO	3.72	-	-0.12	-0.003	-0.31	0.007	-0.13	0.001
NO	2.70	acceptor	-0.44	-0.067	-0.32	-0.074	-0.13	-0.094
NO_2	2.44	acceptor	-0.81	-0.156	-0.50	-0.185	-0.24	-0.039
H_2O	2.98	acceptor	-0.20	-0.021	-0.14	0.035	-0.17	-0.01
O_2	3.21	acceptor	-0.61	-0.116	-0.27	-0.064	-0.12	-0.001
NH_3	3.41	acceptor	-0.12	-0.029	-0.18	0.050	-0.20	-0.019
H_2	3.56	donor	-0.04	0.138	-0.13	0.013	-0.05	0.146

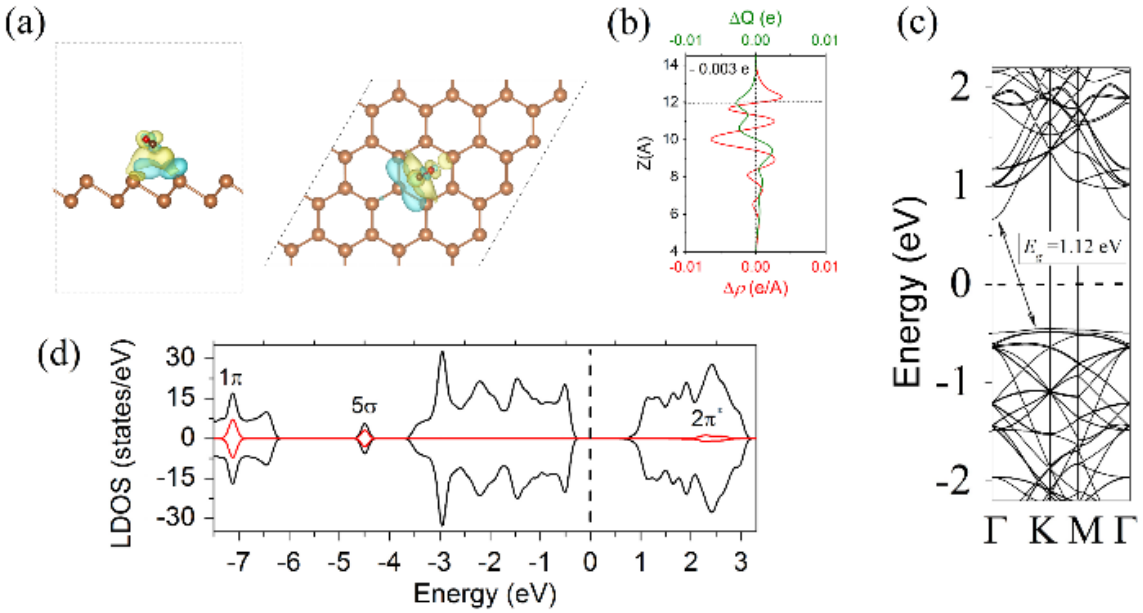

Fig. 4.19. (a) The top and side views of the lowest-energy configuration combined with the DCD isosurface plots (10^{-3} Å^{-3}) for antimonene adsorbed with the CO molecule. The yellow (blue) colour represents an accumulation (depletion) of electrons. (b) The line profiles of the plane-averaged $\Delta\rho(z)$ (red line) and the transferred amount of charge $\Delta Q(z)$ (green line). (c) The band structure of antimonene adsorbed with the CO molecule. The black dashed lines show the Fermi level. (d) The total DOS (black line) and LDOS (red line) of antimonene adsorbed with the CO molecule. The black dashed line shows the Fermi level.

NO adsorption. Figure 4.20(a) shows the most stable configuration and the DCD isosurface plot for the NO molecule adsorbed on antimonene. Similar to the CO adsorption, NO adopts a tilted configuration and is located above the centre of the hexagon with d = ~2.70 Å. However, as a typical open-shell molecule, NO has a much stronger interaction with the underlying antimonene with E_a = -0.44 eV. The magnitude is slightly larger than that of NO on phosphorene (-0.32 eV) [13]. The DCD plot (0.001 Å^{-3}) in Fig. 4.20(a) depicts the orbital-like lobes of the accumulating and diminishing electronic densities, which suggest a redistribution of the surface charges of antimonene upon the NO adsorption. On

the other hand, the population of some NO molecule orbitals becomes less occupied upon interaction with antimonene, while for antimonene most of the transferred electrons are distributed at the Sb atoms closest to the NO molecule. The charge transfer analysis (Fig. 4.20(b)) reveals that NO acts as a strong acceptor to antimonene with a charge transfer of -0.067 *e*, which is similar to the role of NO on phosphorene [13] and InSe [206].

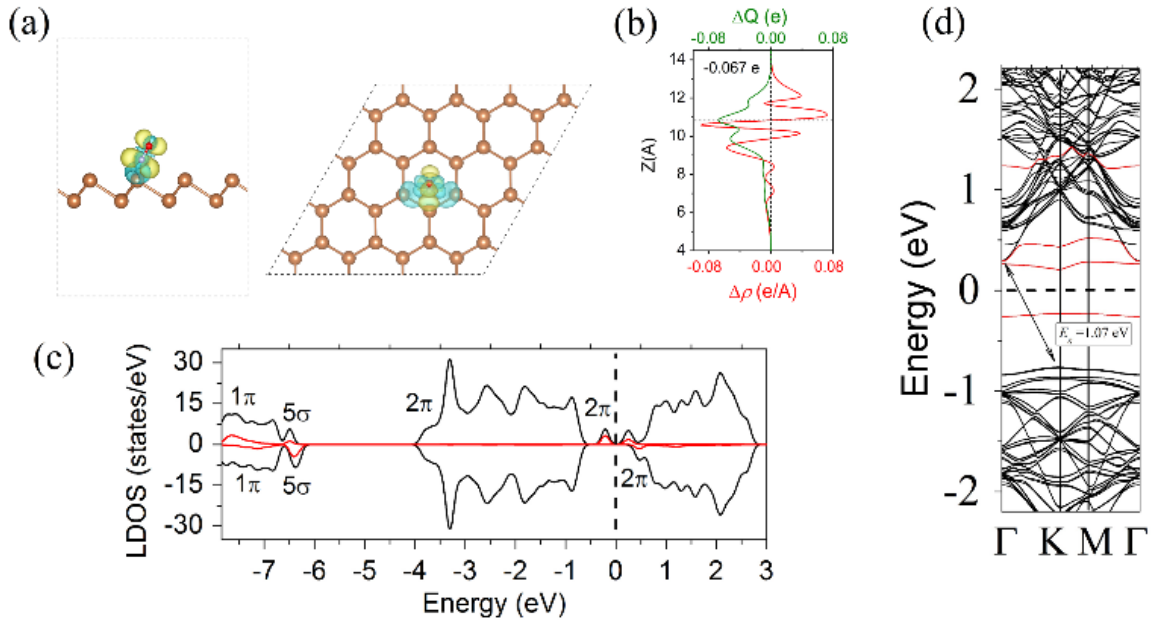

Fig. 4.20. The same as in Fig. 2.19 but for the NO molecule.

The LDOS and band structure plots, shown in Figs. 4.20(c) and (d), respectively, reveal that the state hybridization and charge transfer between NO and antimonene lead to broadening and splitting of the degeneracy of NO orbitals. More specifically, the degeneracy of the 2π orbital is lifted and evolves into two levels located close to the conduction band minimum of the antimonene (Fig. 4.20(c)). In addition, the NO molecule level is spin-split, which induces a magnetic moment of 1 μB in the adsorbed system. The band gap of antimonene adsorbed with the NO molecule slightly decreases from 1.14 eV of the pristine

sheet to 1.07 eV. The presence of NO-induced states within the band gap of antimonene (Fig. 4.20(d)) can modify the electronic and optical properties of antimonene with the NO molecule serving as an electron trapping centre.

NO_2 adsorption. NO_2 has been predicted to have the strongest interaction among the typical small molecules in the cases of phosphorene [13] and InSe [206]. Such strong interaction has been later demonstrated in experiments with the fabrication of phosphorene-based sensors, which show a high selectivity to the NO_2 gas in the presence of other gases [224]. Here, for the NO_2 molecule adsorbed on antimonene, a much stronger interaction (E_a = -0.81 eV) than on phosphorene (E_a = -0.50 eV) [13] is predicted. The most stable configuration and the DCD isosurface plot (0.003 $Å^{-3}$) for the NO_2 molecule adsorbed on antimonene are presented in Fig. 4.21(a). The molecule takes the position above the Sb-Sb bond with the two O atoms situated closer to the surface plane with d = ~2.44 Å. The N-O bond length ranges from 1.25 to 1.27 Å, which is slightly larger than the N-O bond length (1.20 Å) of the free NO_2 gas molecule, resulting from the strong molecule-antimonene interaction. The isosurface plot (Fig. 4.21(a)) and the DCD analysis (Fig. 4.21(b)) suggest a large electron transfer of -0.156 e per molecule from the antimonene surface to the NO_2.

The LDOS plot (Fig. 4.21(c)) shows that the $6a_1$ orbital is split into two levels located within the band gap of antimonene: the LUMO ($6a_1$, spin-down) just above and the HOMO state ($6a_1$, spin-up) just below the Fermi level, which lead to a magnetic moment of 1 μB. In addition, the $4b_1$ and $1a_2$ NO_2 orbitals significantly broaden and coincide with the valence states of antimonene, while the $5b_1$ state coincides with the conduction states of antimonene. Such orbital mixing and hybridization can facilitate the charge transfer between NO_2 and antimonene. The presence of the NO_2 molecule induces localized states within the band gap

(Fig. 4.21(d)), which may affect the optical properties of antimonene. On the other hand, the change of the band gap of the host antimonene (1.17 eV) is negligible compared with that of pristine antimonene (1.14 eV).

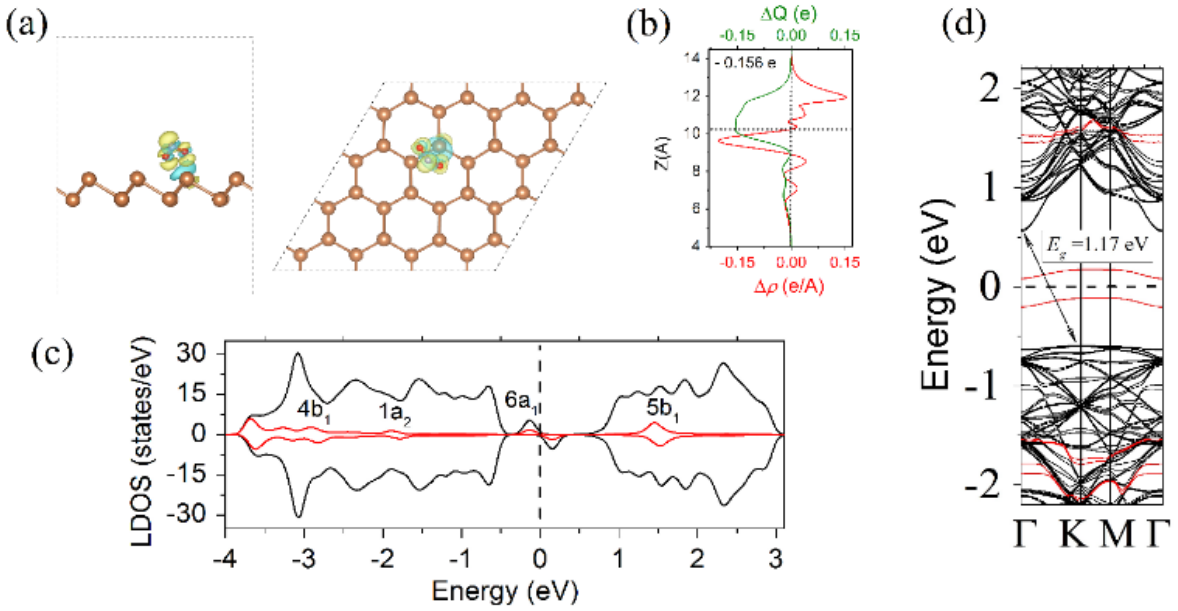

Fig. 4.21. The same as in Fig. 2.19 but for the NO_2 molecule.

H_2O and O_2 adsorptions. Effects of H_2O and O_2 molecules on the electronic properties and charge transfer of 2D materials are highly important with regard to the carrier density and structural stability. The most stable configuration and the DCD isosurface plot ($0.6 \cdot 10^{-3}$ Å^{-3}) for the H_2O and O_2 molecules adsorbed on antimonene are presented in Figs. 4.22(a) and 4.23(a), respectively. The H_2O molecule adopts a flat alignment relative to the antimonene basal plane and is located at d = ~2.98 Å. The O_2 molecule adopts a tilted configuration and is located at the centre of the hexagon at d = ~3.21 Å. The H_2O molecule possesses a relatively weak E_a = -0.20 eV, while the O_2 molecule has a much larger E_a = -0.61 eV.

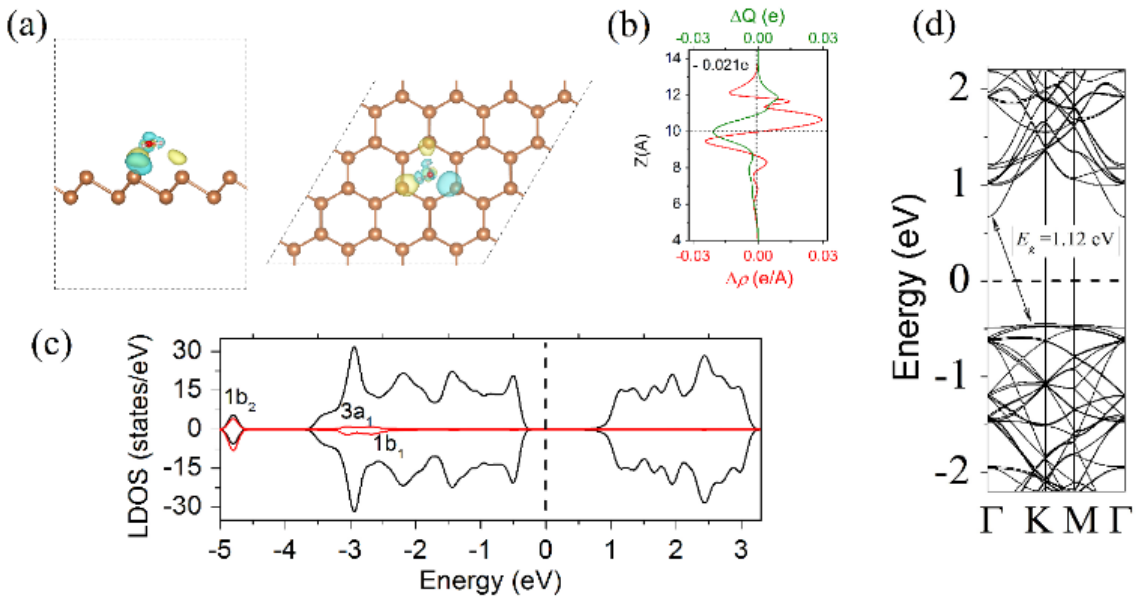

Fig. 4.22. The same as in Fig. 2.19 but for the H_2O molecule.

For the H_2O molecule, the DCD plot (Fig. 4.22(a)) together with the charge transfer analysis (Fig. 4.22(b)) show an accumulation of electrons in the H_2O molecule (acceptor to antimonene) with a total charge transfer of ~-0.021 *e* per molecule. The O_2 molecule also acts as an acceptor with the total transferred charge of ~ -0.116 *e* per molecule (Fig. 4.23(b)). The bond length of the adsorbed O_2 molecule is 1.26 Å, comparable to 1.22 Å of the free molecule. Therefore, similar to phosphorene, antimonene shows high oxidation ability and may oxidize easily at ambient conditions. On the other hand, antimonene demonstrates a weaker interaction with the H_2O molecule, which is similar to phosphorene [13] and graphene [141]. The calculation suggests that the main source of antimonene oxidation originates from the presence of O_2 rather than H_2O, owing to a stronger binding strength and a larger amount of charge transfer of O_2.

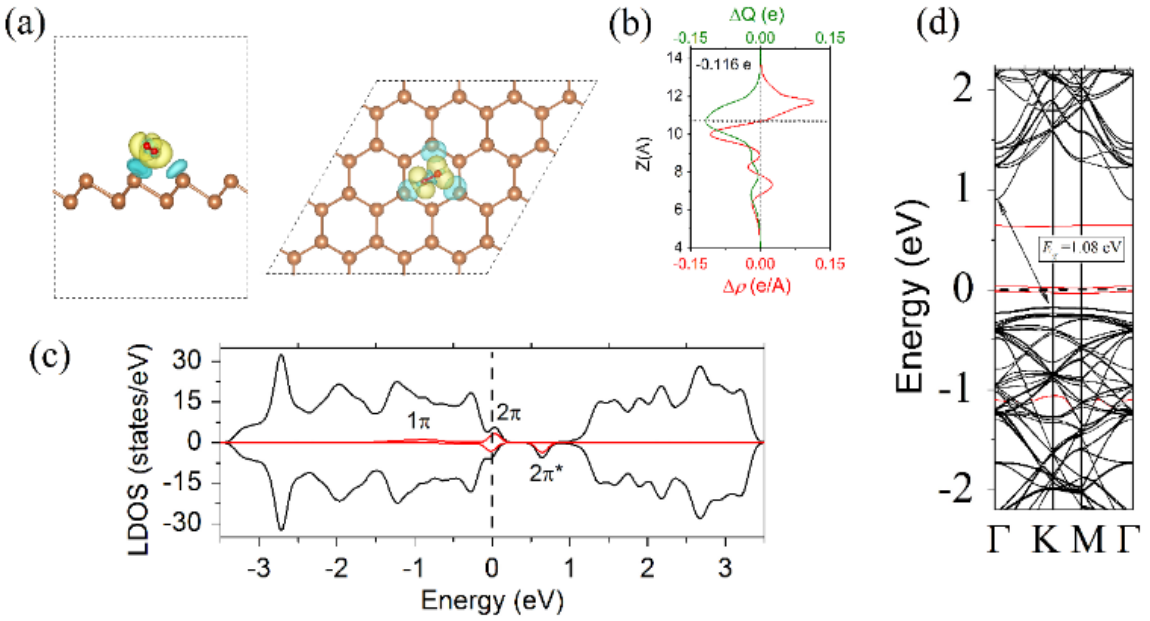

Fig. 4.23. The same as in Fig. 2.19 but for the O_2 molecule.

The LDOS and band structure plots for antimonene adsorbed with the H_2O molecule (Fig. 4.22(c) and (d)) indicate the absence of H_2O-induced states within the band gap of antimonene. In addition, the $1b_2$, $3a_1$, and $1b_1$ orbitals of the H_2O molecule significantly broaden and coincide with the valence states of antimonene (Fig. 4.22(c)). This indicates that the performance of antimonene, such as durability and carrier mobility, tends to be affected by the presence of moisture due to the strong state coupling. For antimonene adsorbed with the O_2 molecule, the LDOS and band structure (Fig. 4.23(c) and (d)) reflect additional O_2-induced states within the band gap of antimonene. The Fermi level crosses the half-filled 2π HOMO state, which aligns slightly above (~0.15 eV) the CBM, allowing the electrons to be excited to the O_2 molecule, and thereby creating holes in antimonene. The $2\pi^*$ LUMO state is located at 0.50 eV above the Fermi level (Fig.4.23 (c)). The presence of the O_2-induced states within the band gap of antimonene and the non-trivial adsorption and

oxidation ability of the O_2 molecule to antimonene can significantly alter the optical and electronic properties of antimonene. In addition, the band structure analysis also shows a small decrease of the band gap size from 1.14 eV of pristine antimonene to 1.08 eV (O_2-induced states are not taken into account) upon the O_2 molecule adsorption.

NH_3 adsorption. Concerning the adsorption of the NH_3 molecule, the lowest energy configuration is found when the molecule is located at d = 3.41 Å at the hollow hexagon centre with the N atom pointing towards the surface and the three H atoms pointing away from the surface (Fig. 4.24(a)). The E_a is -0.12 eV and the lengths of the three N-H bonds are all 1.024 Å, which is comparable with the N-H bond length of 1.01 Å of the NH_3 gas molecule. Charge analysis (Fig. 4.24(a)) shows that electrons are transferred to the NH_3 molecule from the nearest Sb atoms. The total charge transfer from the antimonene surface to the NH_3 molecule is found to be as high as -0.029 *e* per molecule (Fig. 4.24(b)). Similar acceptor behaviour is predicted for the NH_3 molecule adsorbed on InSe [206], while for graphene [141] and phosphorene [13], the NH_3 molecule acts as a donor. The underlying reason for the acceptor role of NH_3 is that the N atom is more electronegative than the Sb and Se atoms. The LDOS analysis (Fig. 4.24(c)) shows that the nonbonding $3a_1$ and the doubly degenerated 1e HOMO orbitals are significantly below the Fermi level and largely broadened, which can indicate the hybridization of these states with the valence states of antimonene. The band structure analysis (Fig. 4.24(d)) reveals no significant change in the band gap size of antimonene adsorbed with the NH_3 molecule compared with that of pristine antimonene.

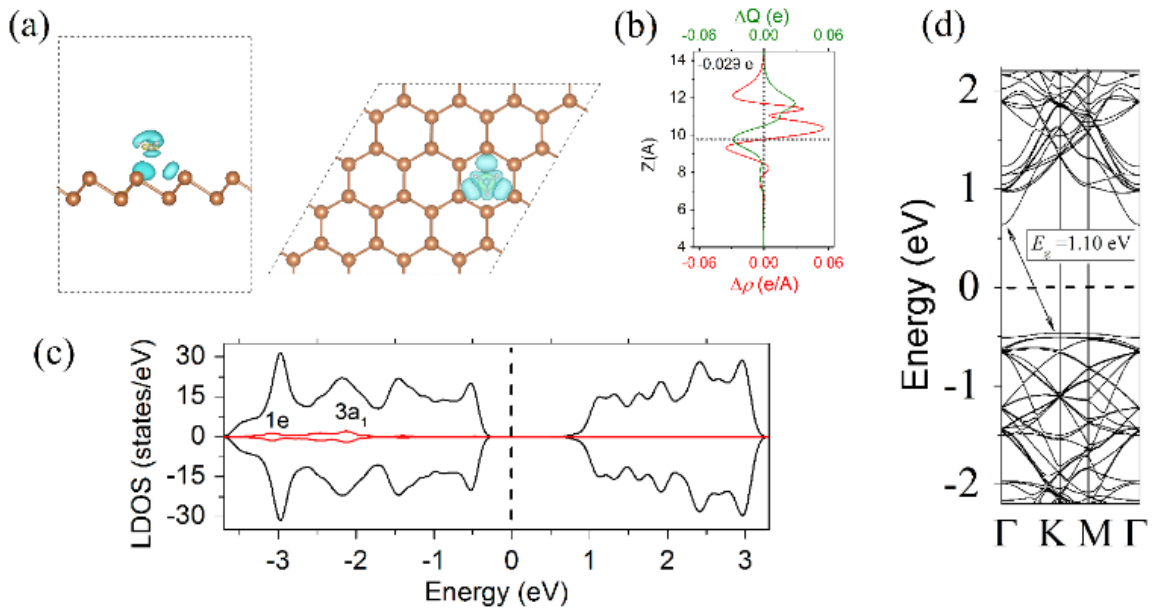

Fig. 4.24. The same as in Fig. 2.19 but for the NH_3 molecule.

H_2 adsorption. The lowest energy configuration for the H_2 molecule is shown in Fig. 4.25(a), where the molecule adopts a tilted configuration with the H-H bond length of 0.75 Å and is located above the Sb atom at d = 3.56 Å. The E_a of the H_2 molecule on antimonene is -0.04 eV, which is comparable with that of InSe [206]. Considering the wide use of graphene as a hydrogen storage material because of its ability for simultaneous stable hydrogen storage and facile release [225], the predicted here H_2 adsorption energy for antimonene suggests that antimonene is a promising material for hydrogen storage devices.

The charge transfer analysis (Fig. 4.25(b)) shows that the H_2 molecule is a donor to antimonene with the moderate charge transfer of 0.138 e per molecule. In Fig. 4.25(a) the DCD isosurface plot ($0.6 \cdot 10^{-3}$ Å^{-3}) indicates a depletion of electrons in both H atoms of the H_2 molecule and an accumulation of electrons at the nearest Sb atoms. Notably, owing to the similar presence of lone-pair electrons on the surface of phosphorene, InSe, and antimonene,

it is interesting to compare the charge doping behaviour of H_2 among them. It is found that the H_2 molecule serves as a donor for all the three cases. However, the total value of charge transfer from H_2 to antimonene is ten times that from H_2 to phosphorene, while it is comparable to that on InSe. The LDOS (Fig. 4.25(c)) and the band structure (Fig. 4.25(d)) analysis reveals that there are no additional H_2-induced states in the vicinity of the antimonene band gap. As a result, the band gap size of antimonene adsorbed with the H_2 molecule is the same as that of pristine antimonene (1.14 eV).

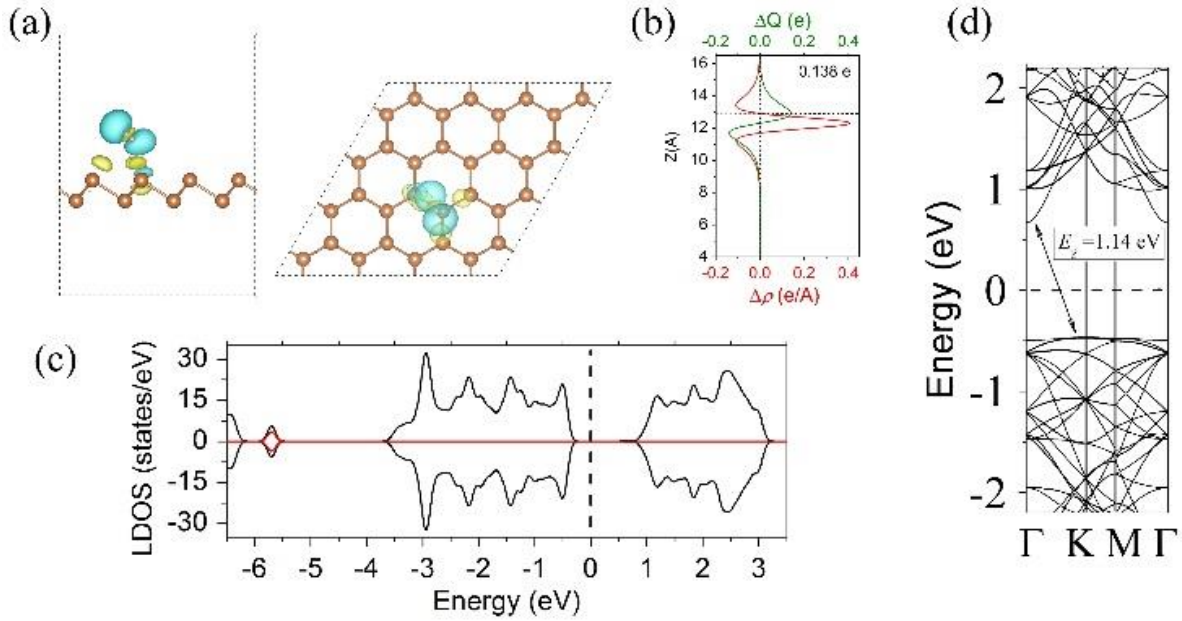

Fig. 4.25. The same as in Fig. 2.19 but for the H_2 molecule.

Comparison of antimonene with phosphorene and InSe. As antimonene is a successor of phosphorene with Sb and P elements being in the same column of the periodic group, it is interesting to compare their surface chemistry with respect to the affinity to the gas molecules. It is known that one common feature of Sb and P elements is the presence of

lone-pair electrons. A recent work on InSe has shown that the presence of lone-pair electrons of the surface Se atoms allows the Lewis base-acid reaction with the surface species [198]. To compare this recently emerging antimonene, phosphorene, and InSe 2D materials, the E_a-Δq relationship for the adsorption of small molecules on their surfaces is plotted Fig. 4.26 plots. For antimonene, the Δq is nearly linearly correlated with E_a for most of the molecules with the exception of H_2 and NH_3 molecules. This indicates that the redox process associated with the charge transfer dominates the noncovalent interaction of these molecules with antimonene. The linear trend is also largely true in InSe but absent in phosphorene.

Clearly, the overall slope of the E_a-Δq curve of phosphorene is higher than that of antimonene. This may be due to a more electronegative nature of P than Sb. Considering that As occupies the same column in the periodic table as P and Sb, it will be interesting to examine the E_a-Δq relationship of arsenene, a layered structure consisting of As atoms. All the considered molecules except the H_2 molecule adsorbed on antimonene lead to *p*-type doping. In comparison with phosphorene, the binding strengths of NO_2, O_2, NO, and H_2O molecules are much stronger, while those of CO, NH_3, and H_2 molecules are weaker on antimonene. Notably, for the H_2 adsorption, the amount of charge transferred from antimonene is 0.138 *e* per molecule, which is ten times higher than that of phosphorene (0.013 *e* per molecule) and comparable with that of InSe (0.146 *e* per molecule). The underlying reason might be attributed to the work function of antimonene, which is comparable to that of InSe but much higher than that of phosphorene. In contrast, the adsorption energy of H_2 on antimonene is much weaker than on phosphorene, largely due to the weak van der Waals interaction with the heavy Sb element.

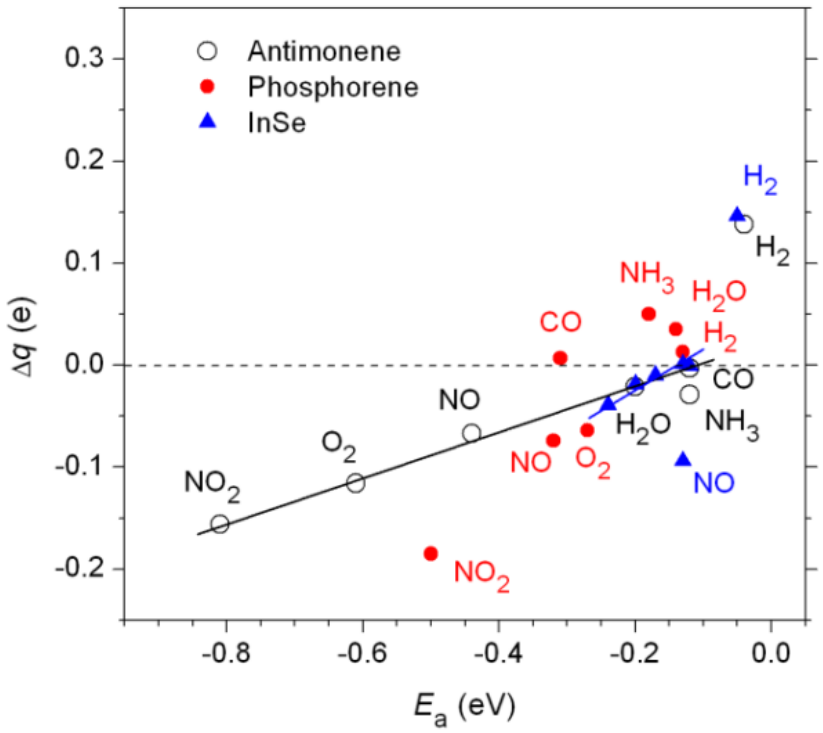

Fig. 4.26. The relationship between E_a and Δq for various molecules physisorbed on antimonene, phosphorene, and InSe. The results for phosphorene and InSe are adopted from Refs. 13 and 206, respectively.

Oxidation kinetics and mechanisms of good structural stability in antimonene. The interaction of O_2 molecules with 2D materials plays a critical role in their stability and performance under ambient conditions as oxidization is the most popular form of structural degradation. The interaction energy between the O_2 molecule and antimonene E_a is found to be -0.61 eV, which is more than two times higher than that between the O_2 molecule and phosphorene (-0.27 eV). A similar situation is found for the charge transfer. These results are reasonable since Sb is less electronegative than P, which leads to a greater transfer of electrons to the O_2 molecule from antimonene. The findings presented here suggest that the

performance of antimonene, for example, the carrier density and mobility, tends to be highly sensitive to the environmental O_2 molecule.

To predict the oxidization behaviour, thermodynamics analysis is insufficient. Therefore, the kinetic analysis on the splitting of the O_2 molecule on the antimonene sheet in the form of terminated -O groups is conducted. The result of the NEB calculation of the above process is shown in Fig. 4.27. Surprisingly, the energy barrier for the decomposition of the O_2 molecule into two apical -O groups is only ~0.40 eV. Such a small barrier implies that antimonene may undergo oxidation during synthesis and applications. The prediction is consistent with the experimental findings which have revealed that there are always some oxygen species above the surface of synthesized antimonene flakes [226]. Previously, the oxidation layer containing antimonene oxide has been reported to have exotic electronic properties [227].

The predicted facile formation of oxygen species in the antimonene sheet is somehow surprising since, as shown in the phosphorene case, these oxygen species tend to react with environmental H_2O molecules, which leads to the degradation of the material by forming acids [228]. However, antimonene has been reported to exhibit a good stability in ambient conditions [213]. Hence, the roles of O_2 and H_2O molecules and their cooperative effect on the stability of antimonene must be different from those in phosphorene. According to Fig. 4.26, while the O_2 molecule plays the same role (acceptor) in phosphorene and antimonene, the H_2O molecule behaves oppositely: it is an acceptor ($[H_2O]^{-\delta}$ with δ being a small positive real number) for antimonene but a donor ($[H_2O]^{+\delta}$) for phosphorene.

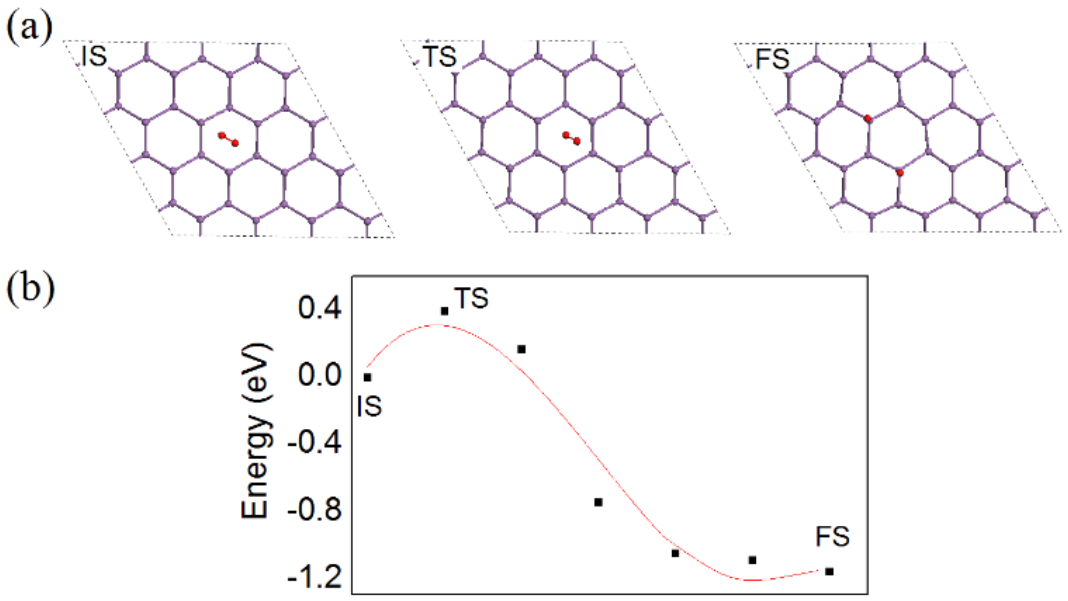

Fig. 4.27. The activation barrier for the splitting of the O_2 molecule on antimonene: (a) the atomic models for the IS, TS, and FS state; (b) The energy profile obtained by the NEB calculation for the decomposition of the O_2 molecule on antimonene.

Based on the well-known mechanism of H_2CO_3 acid formation from CO_2 and H_2O molecules, which occurs through the diffusion of the $H^{+\delta}$ ion in a partially positively charged H_2O to the negatively charged -O group in the CO_2 molecule, herein, it can be proposed that the mechanism of the antimonene stability is related to the electrostatic repulsion between $[H_2O]^{-\delta}$ and -O group (also negatively charged $-O^{-\gamma}$ with γ being a small positive real number). The negatively charged $[H_2O]^{-\delta}$ makes the formation and the diffusion of $H^{+\delta}$ proton to the $-O^{-\gamma}$ group unfavourable. In addition, the high stability of antimonene may also be related to the much longer Sb-Sb bond, which makes the transfer of $H^{+\delta}$ more difficult than the shorter P-P bond in phosphorene. The reason is that the transport of proton between water molecules should depend on the separation of the molecules. Owing to the larger lattice constant in antimonene, the anchored water molecules above Sb atoms should be more

sparsely distributed, which reduces the hopping probability of proton among the water molecules.

The stable surface oxidation layer may be helpful for protecting the underneath antimonene layer against its degradation upon interaction with environmental molecules. Therefore, by comparing the charge transfer behaviour in antimonene and InSe, it can be concluded that systems with H_2O molecules acting as acceptor groups tend to be stable as they are less likely to form acids under the co-adsorption of O_2 and H_2O molecules. The opposite implication is also true if H_2O acts as a donor - the structure tends to be decomposed: one example is an easily degradable phosphorene where H_2O is a charge donor [13].

4.4 Summary

In Chapter 4, the structure stability and electronic properties of several new and perspective 2D materials such as borophene, InSe, and antimonene have been comprehensively analyzed. In addition, properties of considered 2D materials and their behaviour under the effect of different factors, such as surface functionalization, defect engineering, ribbon construction, and influence of environmental molecules have been compared with these of phosphorene (see Chapter 3).

Particularly, the electronic properties of surface functionalized borophene sheets and the possible avenues for opening the band gap of borophene have been investigated. It has been found that the band structure of borophene is immune to the presence of vacancies and the surface functionalization. Interestingly, the anisotropy of the electronic properties and

the nature of the orbitals at the Fermi level can be altered upon the surface functionalization, enabling the modulation of the borophene properties. Due to the high density of itinerant electrons in the atomically thin borophene sheet, the band gap opening via quantum confinement, which is effective for graphene, becomes ineffective for borophene. It has also been revealed that the work function of borophene can be tuned to a large degree as the high electronic gas confined in the atomically thin sheet of borophene can be transferred to the functionalizing groups.

Next, several critical issues in the structural degradation of InSe due to oxygen and humidity at ambient conditions have been considered using first-principles calculations. The oxidation of monolayer InSe has been explored by examining the roles of light illumination, oxygen, water, and defects. It has been shown that pristine InSe has a much lower oxygen affinity than MoS_2 and phosphorene. However, the presence of V_{Se} and light excitation can significantly accelerate the oxidation by greatly decreasing the barrier through forming chemical oxygen species. These atomic O species, which are associated with strong polar O-In bonds, can quench the defective states of V_{Se}, and further act as the adsorption and trapping centres of H_2O molecule. The AIMD results have shown that the apical O atoms in the form of terminated Se-O bonds even allow the spontaneous water splitting and the formation of hydroxyl groups at room temperature. Based on these findings, the following three strategies have been proposed to suppress the oxidation of InSe: i) insulating InSe from O_2 molecules; ii) maintaining the InSe surface stoichiometry; iii) avoiding the exposure of InSe to light illumination.

Further, the energetics and charge transfer of the CO, NO, NO_2, H_2O, O_2, NH_3, and H_2 molecules adsorbed on antimonene have been investigated. It has been found that NO, NO_2,

H_2O, O_2, and NH_3 serve as charge acceptors, while CO shows a negligible charge transfer. The H_2 molecule acts as a charge donor to antimonene with the amount of charge transfer being ten times that of H_2 on phosphorene. The interaction of the O_2 molecule with antimonene is much stronger than that with phosphorene. The examination of the kinetics process of the O_2 molecule splitting on antimonene has revealed a relatively low barrier of ~0.4 eV for the O_2 decomposition, suggesting that antimonene tends to be oxidized during synthesis and applications largely due to the O_2 molecule rather than the water effect. Fortunately, the acceptor role of H_2O on antimonene, opposite to a donor role in phosphorene, helps to suppress further structural degradation of the oxidized antimonene by preventing the proton transfer between water molecules and oxygen species to form acids. By comparing antimonene with phosphorene and InSe, it has been suspected that the acceptor role of water may be a necessary condition for a good environmental stability of such 2D layers to avoid structural decomposition and achieving a robust performance. However, potential antimonene devices still need to be protected via using noncovalent functionalization for suppressing the strong effect from environmental molecules.

Chapter 5 The 2D materials-based heterostructures

Over the past few years, many researches have been focused on hybrid 2D materials, such as graphene-BN [147] and BN-silicene [229] heterostructures. These 2D heterostructures are designed to overcome limitations and to develop the performance of individual 2D materials [230, 231]. In addition, because of their atomically thin structure and large surface area, 2D materials such as phosphorene, silicene, and InSe are easily subjected to exposure of the environment, and their electronic properties can be greatly affected by it [13]. To protect chemically unstable 2D materials, commonly, passivation by using more stable 2D materials, such as graphene or BN, as a capping layer is used [232]. In this chapter, the effects of different factors on the electronic structure and chemical activity of graphene- and InSe-based heterostructures are systematically investigated.

5.1 Strain and water effects on the electronic structure and chemical activity of in-plane graphene/silicene heterostructure

Manufacturing of vertically stacked materials has disadvantages, due to the possible contamination between layers, which leads to significant challenges for the massive production of the samples [233]. In that case, the in-plane interconnected heterostructures, for which there are no such issues in their production, have attracted great attention from both theoretical and experimental sides [234, 235].

Recently, many studies have reported on the effects of various factors on the electronic properties of different heterostructures [234-236]. For example, electric-field engineering has been applied to modify the band gap of graphene/h-BN heterostructures [237]. The work

[238] has predicted that despite the differences in the electronic and mechanical properties of graphene/silicene heterostructure under different types of applied strain, for a gas adsorption at sites far away from the interface region, the type of strain applied is expected to exert little effect due to the nearly isotropic nature of both graphene and silicene sheets. In addition, mechanically-tuned band gap has been predicted in graphene/h-BN [237] and graphene/MoS_2 heterostructures [239]. However, it has been noted that the strain effects on the in-plane graphene/silicene heterostructure remain unexplored.

In this section, the investigations on the effects of strain and adsorption of humidity (H_2O) molecules on the electronic structure and chemical activity of the in-plane graphene/silicene heterostructure are performed.

5.1.1 Computational details

The free-standing graphene-silicene heterostructure is created by using the 5×5×1 and 3×3×1 supercells of graphene and silicene (60 carbon and 24 silicon atoms), respectively. To create BN-supported graphene-silicene heterostructure the initial free-standing heterostructure is placed on the BN substrate. The substrate is created by using the 5×11×1 supercell (60 boron and 60 nitride atoms). Periodic boundary conditions are applied in the two in-plane transverse directions, while the vacuum space of 20 Å is introduced along the out-of-plane direction. Due to the difference between the lattice spacing of graphene (a_{gr}) and that of silicene (a_{si}), the mismatch strain along the interface of the graphene-silicene heterostructure is:

$$\varepsilon_{mismatch} = (5a_{gr} - 3a_{si})/(5a_{gr}) \approx 2.7\% \quad (5.1)$$

Since during the relaxation, the supercell period along the zigzag direction is taken as $5a_{gr}$, the strain along the interface direction in the graphene is $\varepsilon_{gr} = 0\%$, and the silicene is $\varepsilon_{si} = \varepsilon_{mismatch}$. The compressed/stretched structure is obtained by applying uniaxial strain in the direction perpendicular to the interface of the graphene-silicene heterostructure. The choice of the asymmetric graphene-silicene interface is based on previous work [240] of in-plane heterostructures, where epitaxy of graphene with other 2D material occurs preferentially along the zigzag direction. The first Brillouin zone is sampled with a 10×10×1 k-mesh grid. The kinetic energy cut-off is set to 450 eV. The adsorption energy E_a and the electronic interaction between the H_2O molecule and graphene-silicene heterostructure was analyzed as it is shown in Section 2.1.6.

5.1.2 Results and discussion

Strain effect on the electronic structure. Figures 5.1(a)-(e) present the variation of the band gap of the in-plane graphene-silicene heterostructure under the tensile strain of 7% and 5%, planar structure (0% of strain), and under the compressive strain of -5% and -7%, respectively, along the armchair direction. It is seen that the heterostructure remains metallic within the strain range as there is no band gap near the Fermi level. For each considered case, the Dirac point is located above the Fermi level, signifying a *p*-type of conduction.

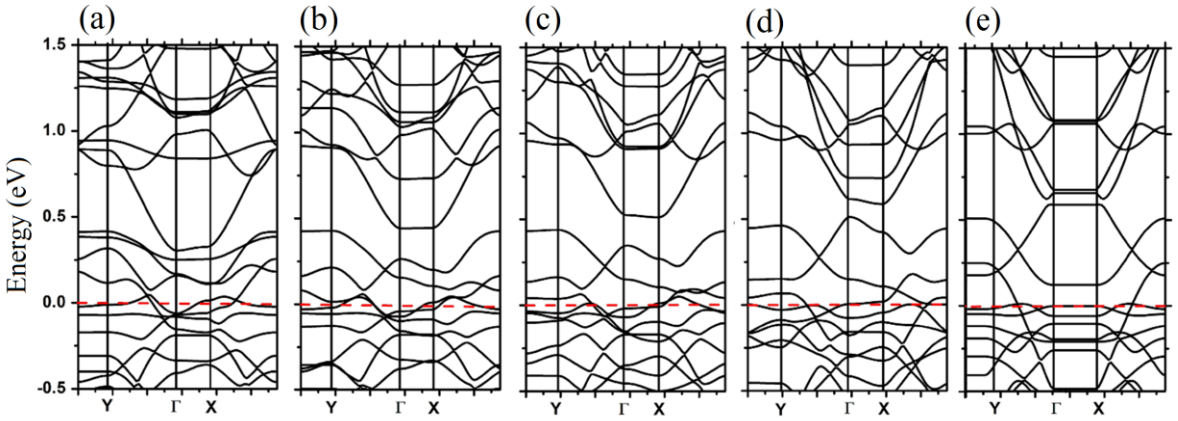

Fig. 5.1. The variation of band gap of in-plane graphene-silicene heterostructure under different strains applied along the armchair direction (a)-(e). The applied strains are (a) 7%, (b) 5%, (c) 0%, (d) -5%, and (e) -7%, respectively.

Interaction with the environmental H_2O molecule. The adsorption of the environmental H_2O molecule on the graphene, silicene, and graphene-silicene interfacial regions of the in-plane graphene-silicene surface is considered. For each case, several possible symmetric anchoring positions of the molecule on the planar and compressed surfaces are examined. All subsequent calculations on the electronic properties and energetics are based on the lowest-energy configurations of the adsorbed heterostructure. The most stable configurations for the case of the H_2O molecule adsorbed on the planar sheet are given in Figs. 5.2(a), (d), and (g). In case of H_2O adsorbed on the graphene region (Fig. 5.2(a)), both O-H bonds are disposed at the angle of around 45° to the surface and located directly above the ridge of graphene. The distance from the molecule to the surface *d* is 2.87 Å, and the value of E_a is -0.152 eV, which is in a good agreement with the result reported in [141]. Figure 5.2(d) shows the H_2O molecule adsorbed on silicene region, in which one of the O-H bonds is parallel to the surface along the armchair direction and the other one is

nearly normal to the surface with d = 2.89 Å and E_a = -0.140 eV, which is in consistent with result in [241]. Figure 5.2(g) presents H_2O adsorbed on the graphene/silicene interfacial region. It is seen that the molecule is located directly above the ridge of the graphene/silicene site, both O-H bonds are nearly parallel to the surface, with d = 2.71 Å and E_a = -0.175 eV.

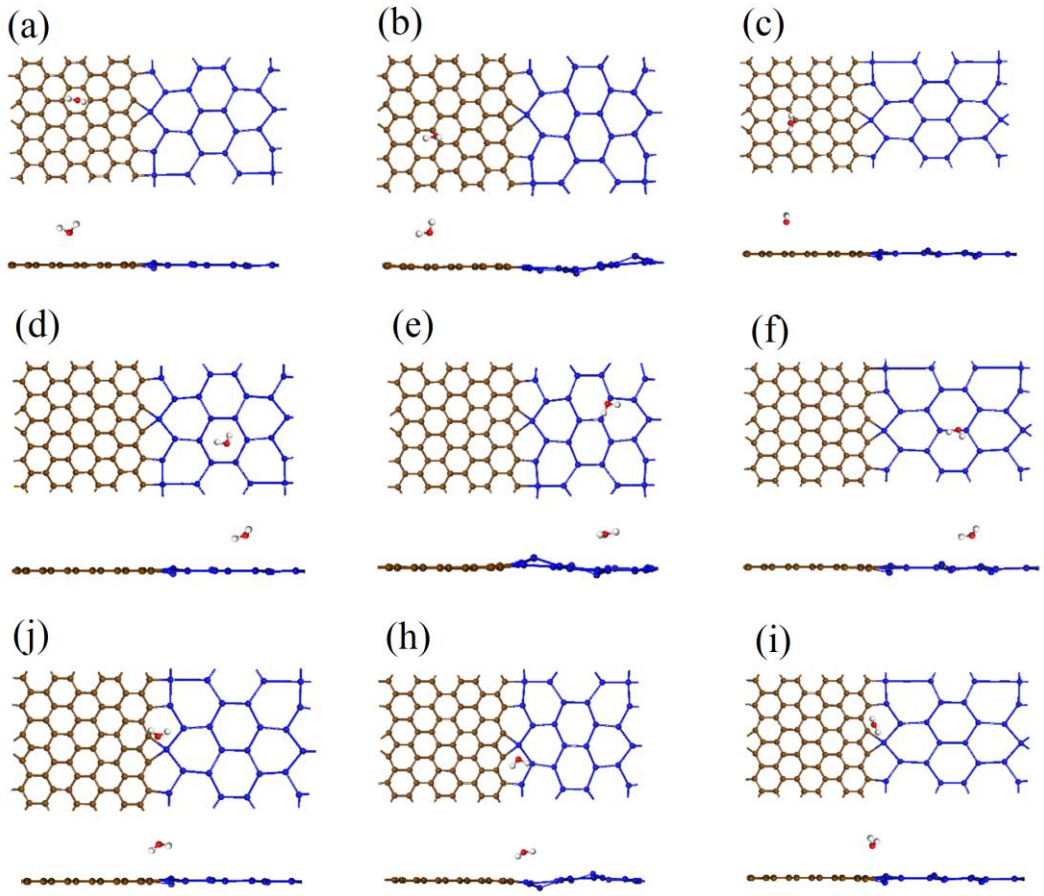

Fig. 5.2. The most stable adsorption positions of the H_2O molecule on different regions of the heterostructure. Under 0% strain: (a) graphene region, (d) silicene region, and (g) the graphene/silicene interfacial region. Under -7% strain: (b) graphene region, (e) silicene region, and (h) the graphene/silicene interfacial region. Under 7% strain: (c) graphene region, (f) silicene region, and (i) the graphene/silicene interfacial region, respectively. The balls in brown, blue, white, and red represent carbon, silicon, hydrogen, and oxygen atoms, respectively.

For H_2O adsorbed on the graphene/silicene sheet under the compressed strain of -7%, the most stable configurations are given in Figs. 5.2(b), (e), and (h). Figure 5.2(b) shows the H_2O adsorbed on the graphene region, in which the in-plane O-H bond is parallel to the surface along the armchair direction while the out-of-plane O-H bond is nearly normal to the surface and located directly above the armchair C-C bond, with d = 2.97 Å and E_a = -0.157 eV. In the case of H_2O adsorbed on the silicene region (Fig. 5.2(e)), both O-H bonds are parallel to the surface and located directly above the zigzag Si-Si bond, with d = 2.82 Å and E_a = -0.175 eV. Figure 5.2(h) presents H_2O adsorbed on the graphene-silicene interfacial region, in which the molecule is located directly above the ridge of the graphene-silicene site and both O-H bonds are nearly parallel to the surface, with d = 2.40 Å and E_a = -0.210 eV.

For H_2O adsorbed on the graphene-silicene sheet under the tensile strain of 7%, the most stable configurations are given in Figs. 5.2(c), (f), and (i). Figure 5.2(c) shows H_2O adsorbed on the graphene region, in which the O-H bonds are disposed at the angle of around 45° to the surface and located directly above the armchair C-C bonds, with d = 3.03 Å and E_a = -0.145 eV. In the case of H_2O adsorbed on the silicene region (Fig. 5.2(f)), both O-H bonds are parallel to the surface and located directly above the armchair Si-Si bond, with d = 2.72 Å and E_a = -0.154 eV. Figure 5.2(i) presents H_2O adsorbed on the graphene/silicene interfacial region, in which the molecule is located directly above the ridge of the graphene/silicene site and both O-H bonds are nearly parallel to surface, with d =2.61 Å and E_a = -0.160 eV.

It is found that in the case of the compressive strain, the adsorption energy increases with strain. A large enhancement is observed for the cases of the H_2O adsorption on the silicene and graphene-silicene interfacial regions, which may be explained by the large

distortion of the silicene lattice and Si-Si bonds deformation. Tensile strain leads to the decrease of the adsorption energy in the cases of the H_2O molecule adsorption on the graphene and graphene-silicene interfacial regions, while the adsorption energy increases in the case when H_2O adsorbed on the silicene region.

To gain insight into the electronic properties of the planar (under 0% strain), compressed (under the strain of -7%) and stretched (under the strain of 7%) graphene-silicene heterostructures after the H_2O doping, the LDOS are studied. The LDOS analysis reveals that the additional electronic states induced by H_2O are located below the Fermi level for the molecular adsorption on planar, compressed or stretched surfaces (Fig. 5.3). However, the alignment of the molecular levels of H_2O is strongly dependent on the region of molecular adsorption and affected by strain.

Figures 5.3(a), (d), and (g) present the three highest occupied molecular orbitals $1b_1$, $3a_1$, and $1b_2$ of the H_2O molecule adsorbed, respectively, on the graphene, silicene, and graphene-silicene interfacial regions of the planar sheet. Clearly, the distributions of molecular orbitals are different for each region of the heterostructure. Moreover, by comparing the planar, compressed and stretched structures of silicene region (as shown in Figs. 5.3(d), (e), and (f), respectively) and the graphene-silicene interfacial region (Figs. 5.3(g), (h), and (i)), it is seen that $1b_1$, $3a_1$, and $1b_2$ molecular orbitals of the H_2O molecule are shifted downwardly by around 0.25 eV for the cases when the compressive or tensile strains are applied.

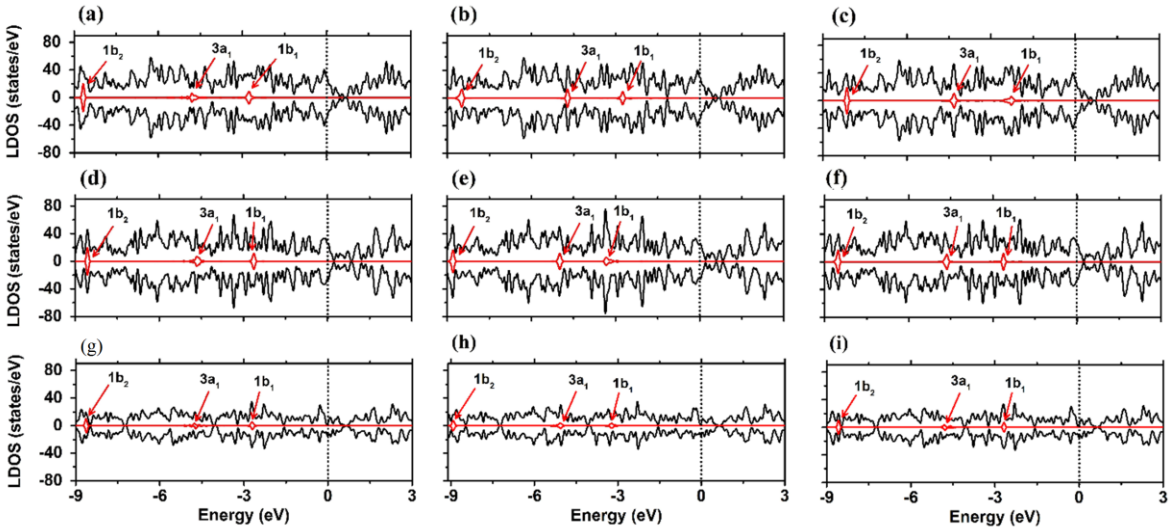

Fig. 5.3. The LDOS of the H_2O molecule on different regions of the heterostructure. Under 0% strain: (a) graphene region, (d) silicene region, and (g) the graphene/silicene interfacial region. Under -7% strain: (b) graphene region, (e) silicene region, and (h) the graphene/silicene interfacial region. Under 7% strain: (c) graphene, (f) silicene, and (i) the graphene/silicene interfacial region, respectively. The spin-up and -down bands for H_2O are the same and shown by the red line, while the black line represents the total DOS.

Modulation of carrier density and charge transfer. To analyze the electronic interaction of the graphene-silicene heterostructure with the H_2O molecule, the DCD $\Delta\rho(r)$ is calculated. The isosurface of the $\Delta\rho(r)$ for the H_2O molecule adsorbed on the different regions of the graphene-silicene heterostructure under 0, -7, and 7% strains are depicted in Figs. 5.4(a)-(c), 5.5(a)-(c) and 5.6(a)-(c), respectively.

For the planar surface, there is a depletion of electrons in the H_2O molecule and an accumulation of electrons in the nearest C atoms within the graphene region (Fig. 5.4(a)). The H_2O molecule donates electrons to the graphene (around 0.024 *e* per molecule). This result is consistent with the previous DFT study [241], where H_2O was found to be a donor

on graphene. The charge transfer analysis for the H_2O adsorbed on the silicene region of the planar structure (Fig. 5.4(b)) shows that the molecule accepts about 0.092 *e*. In the case when H_2O adsorbed on the planar graphene-silicene interfacial region (Fig. 5.4(c)), the total amount of transferred charge is 0.057 *e*. Interestingly, electrons accumulate in the nearest C atoms, while the Si atoms donate electrons to the H_2O molecule.

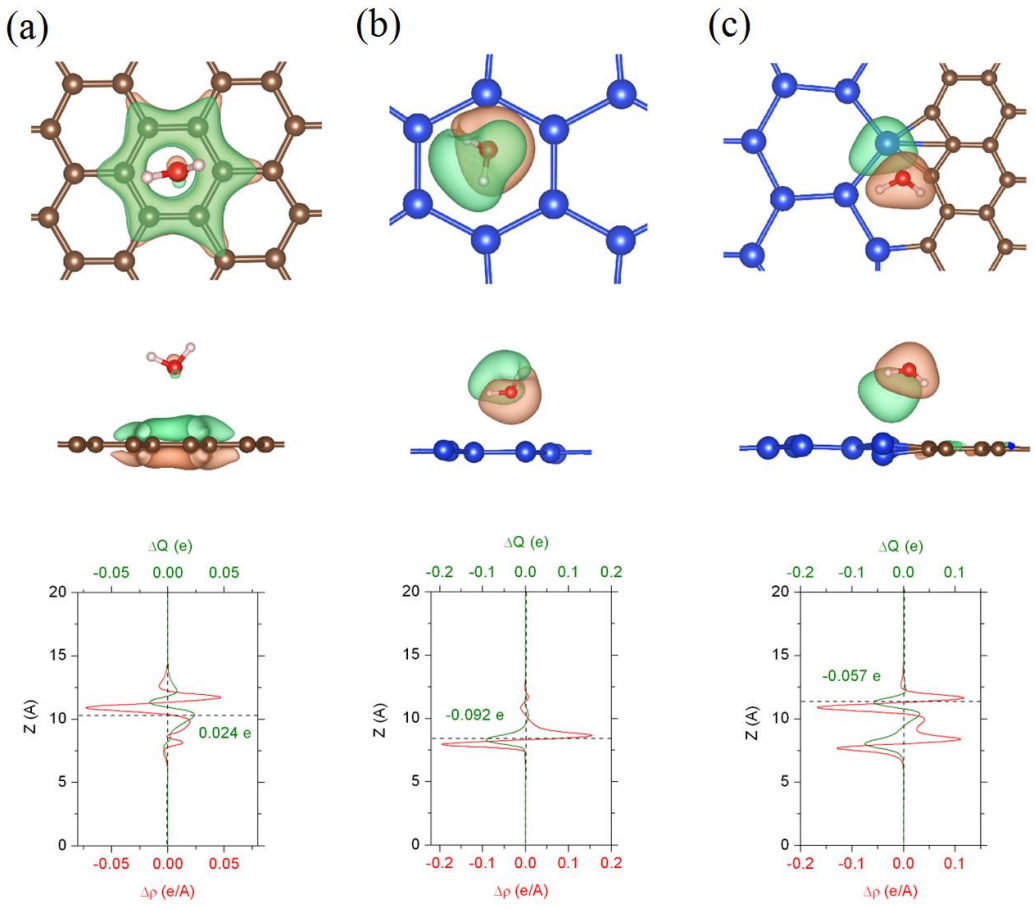

Fig. 5.4. The top and side views of the 0.02Å^{-3} DCD isosurface (the green/orange colour denotes depletion/accumulation of electrons), the plane-averaged DCD $\Delta\rho(z)$ (red line) and the amount of transferred charge $\Delta Q(z)$ (green line) for the H_2O molecule adsorbed on (a) graphene, (b) silicene, and (c) graphene-silicene interfacial regions of the planar graphene-silicene sheet.

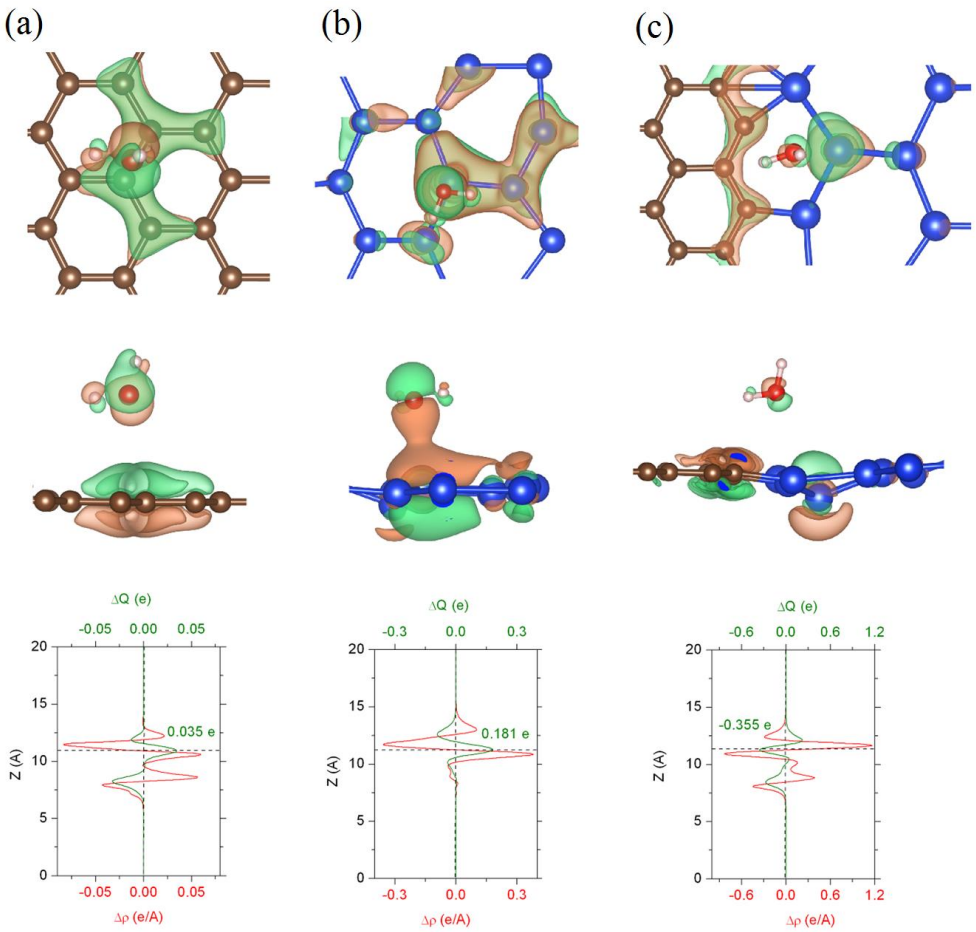

Fig. 5.5. The same as in Fig. 5.4 but for the compressed graphene-silicene sheet.

The compressive strain of -7% leads to an increase in the chemical activity of the H_2O molecule, and the total amount of the charge transferred from the molecule to the C atoms of the graphene region (Fig. 5.5(a)) is 0.035 *e*. Figure 5.5(b), where H_2O is adsorbed on the silicene region of the compressed structure, clearly indicates an accumulation of electrons in the Si atoms. Thus, H_2O serves as a donor in this case where charge transfer from the molecule to the surface is 0.181 *e*. A significant increase of the charge transfer, up to -0.355 *e*, is found for the case of H_2O adsorption on the interfacial region of the compressed structure (Fig. 5.5(c)), and the main charge transfer is still observed for the C atoms. The obtained

results suggest that the carrier density and the charge transfer between the H_2O molecule and different regions of the in-plane graphene-silicene heterostructure, as well as a donor/acceptor ability of the H_2O, can be significantly tuned by compressive strain.

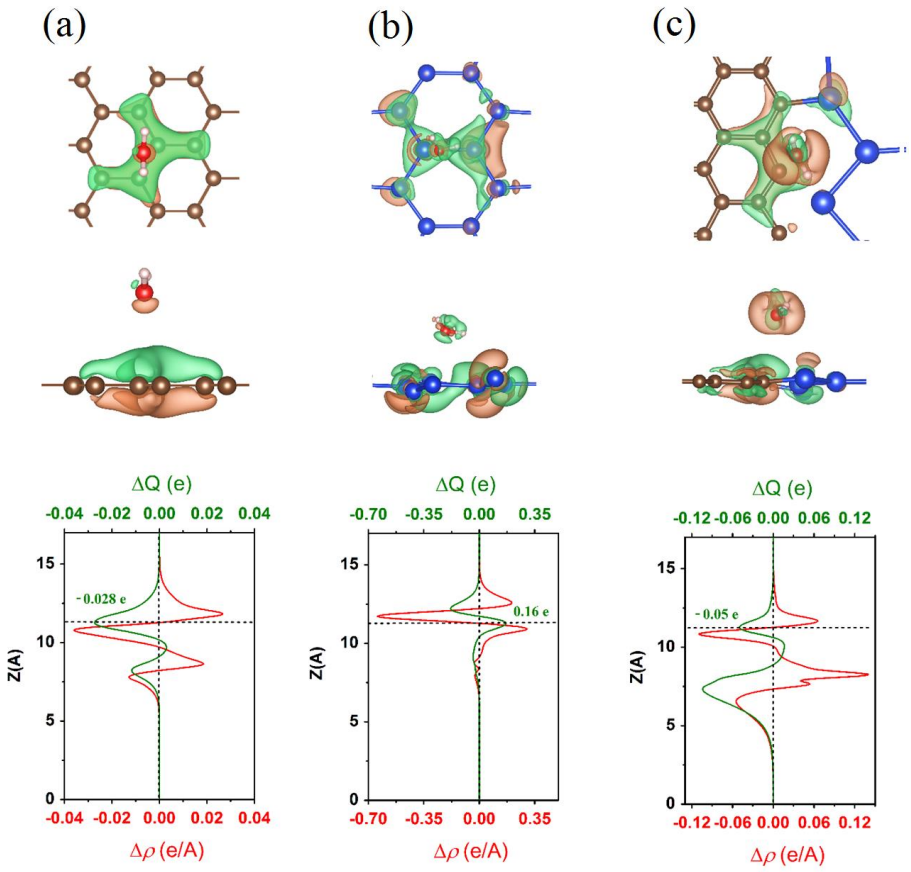

Fig. 5.6. The same as in Fig. 5.4 but for the stretched graphene-silicene sheet.

The tensile strain of 7% also leads to the change in the chemical activity of the H_2O molecule. In particular, the total amount of transferred charge from the C atoms of the graphene region to the molecule (Fig. 5.6(a)) is 0.028 *e*, clearly indicating that H_2O serves as an acceptor. Figure 5.6(b), where the H_2O is adsorbed on the silicene region of the stretched

structure, indicates that molecule donates about 0.160 *e* to the surface, signifying that H_2O serves as a donor. For the case of H_2O adsorption on the interfacial region of the stretched structure (Fig. 5.6(c)) the main charge transfer, up to 0.050 *e*, is still observed for the H_2O molecule. The obtained results suggest that the carrier density and the charge transfer between the H_2O molecule and different regions of the in-plane graphene-silicene heterostructure, as well as a donor/acceptor ability of the H_2O, can be tuned by tensile strain.

The effects of the BN-substrate on the chemical activity of the graphene-silicene heterostructure. To understand the effect of substrate on the chemical activity of the graphene-silicene heterostructure, the h-BN monolayer is selected as a substrate. Specifically, the substrate effects on the adsorption energies and the charge transfer between the graphene-silicene heterostructure and the H_2O molecule are considered. For the heterostructure supported by the substrate without applying strain, the most stable configurations for the H_2O molecule adsorbed on different regions of the heterostructure are given in Figs. 5.7(a), (b), and (c).

In the case of H_2O adsorbed on the graphene region (Fig. 5.7(a)), both O-H bonds are disposed at the angle of around 45° to the surface and located directly above the ridge of graphene, which is similar to the case in which H_2O is adsorbed on the graphene region of the free-standing surface. The value of E_a is -0.152 eV and the total amount of transferred charge from the molecule to the surface is 0.024 e. Figure 5.7(b) shows the H_2O molecule adsorbed on the silicene region of the substrate-supported heterostructure, in which the O-H bonds are disposed at the angle of around 45° to the surface and located directly above the ridge of silicene. The value of E_a is -0.140 eV and the total amount of transferred to the molecule is 0.092 e. Figure 5.7(c) presents H_2O adsorbed on the graphene-silicene region. It

is seen that the molecule is located directly above the C-Si bond of the graphene-silicene site, and both O-H bonds are disposed at the angle of around 45° to the surface. The value of E_a is -0.175 eV and the total amount of transferred to the molecule is 0.057 e.

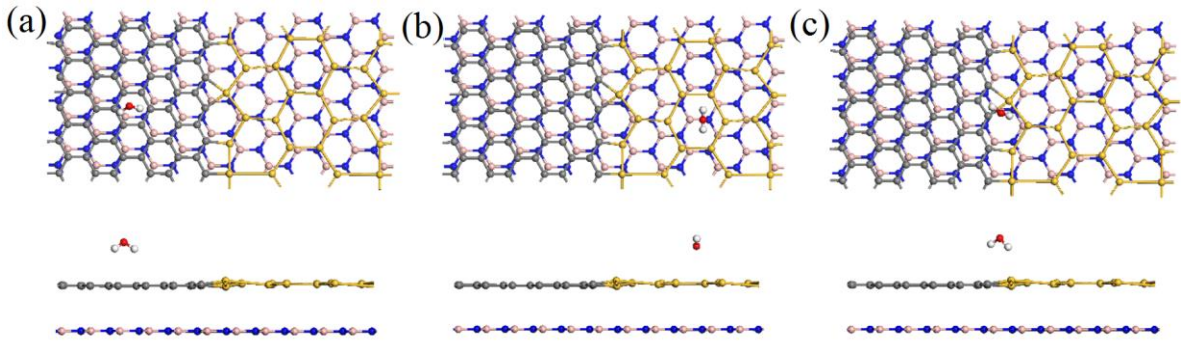

Fig. 5.7. The most stable adsorption positions of the H_2O molecule on the graphene-silicene heterostructure supported by the BN layer without applying strain: (a) graphene, (b) silicene, and (c) the graphene-silicene interfacial regions. The balls in grey, yellow, white, red, blue, and pink represent carbon, silicon, hydrogen, oxygen, nitrogen, and boron atoms, respectively.

It is found that the BN-substrate has a small effect on the adsorption energy when the H_2O molecule is adsorbed on the graphene region of the graphene/silicene heterostructure. However, for the substrate-supported heterostructure, the adsorption energy is slightly higher for the case of H_2O adsorbed on the silicene region and significantly lower for the case where H_2O is adsorbed on the graphene-silicene interfacial region, compared with the adsorption energy of the free-standing heterostructure. The charge transfer analysis reveals that the presence of the BN-substrate significantly influences the donor/acceptor ability of the H_2O molecule upon its adsorption on the graphene-silicene heterostructure and may cause an increase/decrease of the charge transfer between the H_2O molecule and the heterostructure.

5.2 Effects of graphene-BN encapsulation, surface functionalization, and molecular adsorption on the electronic properties of layered InSe

InSe, a newly emerging 2D layered metal monochalcogenide III-VI compound, has attracted great attention owing to its high carrier mobility and anomalous optical response [197, 198]. In contrast to TMDs such as MoS_2, which possesses a direct band gap for monolayer and an indirect band gap for multilayer [199], InSe has a direct band gap for bulk phase and an indirect band gap obtained by reducing the number of layers to make its thickness below a critical value at about several nanometres [242]. In addition, InSe samples with a direct band gap span a broad thickness range, from infinite thickness down to several nanometres, allowing a stronger excitonic emission and a broader frequency spectrum than TMDs. As a result, layer engineering of InSe should be highly effective for tuning the momentum conservation of quasi-particles, in addition to the traditional quantum confinement effect.

Recently, much effort has been devoted to investigating the exfoliation [242] and electronic applications [195, 203, 204, 243] of InSe, for example, in optoelectronics and photovoltaics. However, the mobility of InSe-based transistors at ambient condition has been found to degrade due to environmental effects and defects [205]. Therefore, identifying the effective strategies to protect InSe sheets is important for the reliability of InSe-based electronic devices [244]. For atomically thin 2D materials like MoS_2 and phosphorene, encapsulation by chemically more inert 2D layers, like graphene and BN, has been found to effectively suppress the adverse environment effect [147, 245] and rectify interfacial

resistance at the electrode contact [246]. Concerning InSe, the effects of BN and graphene encapsulation on its electronic and chemical properties remain unclear.

For practical applications of a semiconducting InSe layer, there is a need to develop methods to control the polarity and concentration of its conducting carriers. As an intrinsic InSe layer shows a *p*-type conduction [206], the realization of *n*-type conduction is highly desired. Traditional substitution doping strategy that has been widely adopted in bulk semiconductors is highly challenging for 2D materials as it tends to destroy their 2D structural integrity. To this end, various doping approaches by using surface functionalization of 2D materials have been developed [247]. Recently, it has been reported that *in-situ* deposition of potassium (K) atoms is able to significantly tune the band gap of black phosphorus [248] and the intercalated K dopants are able to increase the electron mobility due to a charge-transfer induced giant vertical electrical field [249]. However, there is no clear information on the modulation of electronic properties of InSe through molecular adsorption and surface functionalization.

In this section, the electronic structure of monolayer InSe is systematically investigated through graphene-BN encapsulation, molecular adsorption, and chemical functionalization. Furthermore, the charge-transfer induced effects caused by the adsorption of the K atom on monolayer InSe, InSe-graphene, and InSe-BN heterostructures are explored.

5.2.1 Computational details

The relaxed lattice constant of monolayer InSe is $a = b = 4.102$ Å. To simulate the surface chemical functionalization, a 3×3×1 supercell of InSe is used. A vacuum space of 25

Å is introduced along the out-of-plane direction. The first Brillouin zone is sampled with a 6×6×1 k-mesh grid. The kinetic energy cut-off is set to 400 eV. All structures are fully relaxed until the total energy and atomic forces are smaller than 10^{-5} eV and 0.01 eV/Å, respectively. The binding strength σ_b is calculated as $\sigma_b = E_b/S_{surface}$, where E_b is the binding energy for the InSe-graphene or the InSe-BN heterostructures and $S_{surface}$ is the surface area of the supercell. The commensurate atomic structures of the vertical InSe-graphene and InSe-BN heterostructures through stacking a monolayer InSe and a monolayer graphene-BN along the normal direction are created by using the 3×3×1 supercell of InSe and the 5×5×1 supercell of graphene-BN. The in-plane lattice constant of the hybrid structures is adjusted to the lattice constant of the InSe supercell, and in the mismatch strain in the graphene-BN layer is smaller than 1.6 %. The optimized distances of InSe from graphene and BN are 3.37 and 3.48 Å for InSe-graphene and InSe-BN, respectively. The electronic charge analysis is performed by the Bader approach.

5.2.2 Results and discussion

Heterostructures formed by graphene and BN encapsulation. To suppress the potential environmental effect, InSe passivation with the relatively inert graphene or BN layer could be an effective approach, which has been demonstrated in phosphorene flakes. However, the effect of graphene and BN on the electronic properties of InSe remains unclear. Figures 5.8(a)–(c) (upper panel) show the atomic structures of the optimized monolayer InSe, InSe-graphene, and InSe-BN heterostructures. The binding strengths σ_b for InSe-graphene and InSe/BN heterostructures are 0.52 and 0.23 eV/Å^2, respectively. Figure 5.8 (lower panel)

presents the band structures of monolayer InSe, InSe-graphene and InSe-BN heterostructures. It is found that monolayer InSe is a semiconductor (Fig. 5.8(a), lower panel) with an indirect band gap of 1.33 eV, which is consistent with previous works [206, 207].

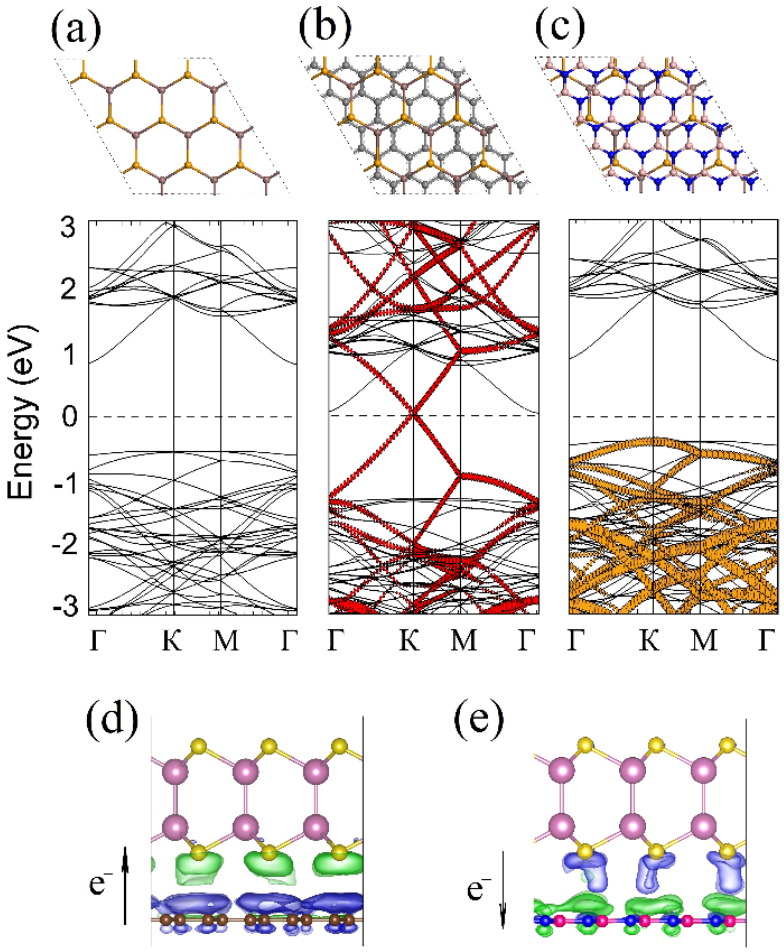

Fig. 5.8. Upper panel: the lattice and band structures of (a) InSe, (b) InSe-graphene and (c) InSe-BN. The bands coloured in black, red and orange show InSe, graphene and BN, respectively. The black dashed line shows the Fermi level. Bottom panel: the side view of the 0.12 $Å^{-3}$ DCD isosurface for (d) InSe-graphene and (e) InSe-BN heterostructures. The blue (green) colour denotes depletion (accumulation) of electrons. The spheres coloured in yellow, violet, brown, pink and blue show selenium, indium, carbon, boron, and nitrogen atoms. The black arrows show the charge transfer direction.

For InSe-graphene heterostructure (Fig. 5.8(b)), the Dirac cone formed by graphene is preserved and it almost overlaps the conduction band edges of InSe. Instead, InSe-BN heterostructure (Fig. 5.8(c), lower panel) remains a semiconductor with the reduced indirect band gap of 1.26 eV, compared with the naked monolayer InSe. The top valence band of BN is aligned with that of InSe, while there are no BN states overlapping with the InSe state in the lower lying conduction bands due to the much larger band gap of BN.

In order to gain further insight into the interlayer interactions of the considered heterostructures, the charge transfer between InSe and graphene-BN layers is examined by calculating the DCD. Figures 5.8(d) and (e) show the isosurface plots of the DCD for InSe-graphene and InSe-BN heterostructures, where blue (green) denotes depletion (accumulation) of electrons. It is found that the total amount of the transferred charge from the graphene to InSe surface is 0.11 *e*. In contrast, there is an opposite trend of the charge transfer for InSe-BN, where the electron is transferred from InSe to BN, the total amount of the transferred charge is around 0.07 *e*.

The obtained results predict that graphene and BN play an opposite role in doping InSe, which is dramatically different from the phosphorene-graphene/BN bilayer, where graphene and BN play the same role as a weak donor [13]. The charge transfer should be attributed to the dipole-induced charge redistribution at the interface due to the B-N polar bond. The lone-pair electron densities in the Se atom are distorted toward pairing with the N atom, which has a higher electronegativity than the Se atom. Moreover, both B atoms in a BN sheet and Se atoms in an InSe sheet possess Lewis acidic characteristics, thus favouring the interaction between the B atoms and the Se atoms [198]. It should be noted that the band structure of the InSe-BN bilayer system does not show a typical *p*-type doping behaviour of InSe. The

underlying reason for that may be a very weak charge transfer from InSe to BN and a weak charge screening effect in this hole-doped 2D system.

In addition to the InSe-graphene (BN) bilayer system, the periodic InSe-graphene (BN) superlattice with the sequential stacking of InSe and graphene (BN) along the normal direction is also considered. As the lone-pair electronic states exist in the top Se atoms [206], it is necessary to investigate the modulations of the electronic structure of the hybrids, in particular, to see any indirect-direct transition of InSe, by changing the van der Waals gap. The modified interlayer distance d_i should significantly affect the hybridization of the Se states and the graphene and BN states.

The total energy E_{tot} of InSe-graphene (red line) and that of InSe-BN (black line) systems as a function of d_i are calculated and shown in Fig. 5.9(a). The calculated equilibrium distance corresponding to the lowest E_{tot} is around 3.32 Å for both InSe-graphene and InSe-BN structures with the variation of E_{tot} with d_i in a range from 3.2 to 3.5 Å. In Fig. 5.9(b), the external pressure corresponding to each d_i below the equilibrium lattice for InSe-BN system is listed. It is found that the InSe-graphene heterostructure remains zero-band gap (E_g) for all the considered values of d_i due to the presence of the Dirac cone in graphene. For InSe-BN system, the modification of d_i leads to a nonlinear change of E_g. Figure 5.9(b) shows that with the decrease of d_i, E_g slightly increases from 1.24 eV (d_i = 3.20 Å) to the maximum value of 1.57 eV (d_i = 3.12 Å), and then monotonically decreases to 0 eV (d_i = 2.0 Å). The presence of a concave shape and a strong nonlinearity of the d_i - E_g curve around the equilibrium suggests a strong electron-lattice coupling in the hybrid system. The band structures of InSe-graphene and InSe-BN bulk systems at d_i = 3.2 Å are shown in Figs. 5.9(d) and (c), respectively.

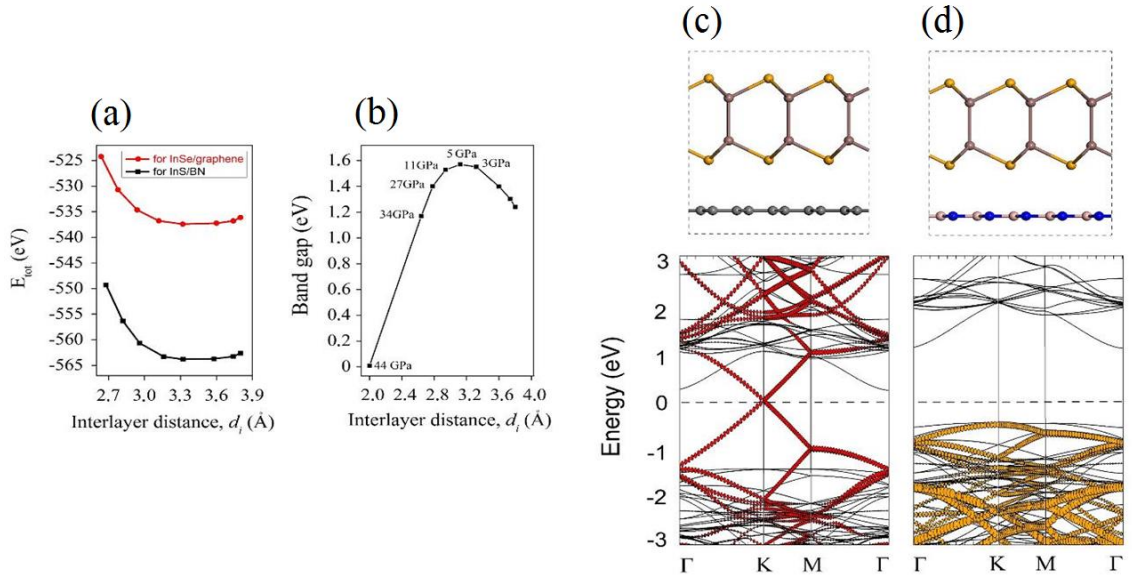

Fig. 5.9. (a) The total energy of the system as a function of the interlayer distance d_i in InSe-graphene (red line) and InSe-BN (black line). (b) The modulation of the band gap of the InSe-BN system as a function of the interlayer distance d_i. The atomic structure (upper panel) and the band structure (bottom) of (c) InSe-graphene at d_i = 3.2 Å and (d) InSe-BN at the d_i = 3.2 Å. The bands coloured in black, red and orange represent InSe, graphene, and BN, respectively. The black dashed line shows the Fermi level.

By comparing with the band structures of bilayer InSe-graphene (Fig. 5.8(b)), it is seen that the Dirac cone formed by graphene is also preserved but less shifted to the conduction band edges of InSe (Fig. 5.9(c)). This adjusted band alignment may significantly modify the carrier recombination behaviour at the interface. The optical, electronic and thermal properties under pressure are dramatically different from those in the freestanding case. For both pressured InSe-graphene and InSe-BN systems, there is no indirect-direct transition of the band gap in InSe.

Chemical functionalization of monolayer InSe-graphene and InSe-BN heterostructures. Next, the molecular adsorption of graphene (BN) encapsulated InSe is

discussed. First, the doping through adsorbing a single K, Al and Mg atom on InSe is investigated. The motivation is to induce an *n*-type conduction in InSe as the considered atoms have a small electronegativity and a strong ability to donate electrons. Figures 5.10(a)–(c) and (d)–(f), respectively, show the band structures of InSe–graphene and InSe–BN heterostructures with the K atom adsorbing at three different heights of d = 3.0, 3.6 and 4.2 Å above the surface (the atomic configurations are presented in Fig. 5.11). As found for monolayer InSe, here the upward shift of the Fermi level in K–doped InSe–graphene and InSe–BN heterostructures with the decrease of d is also observed.

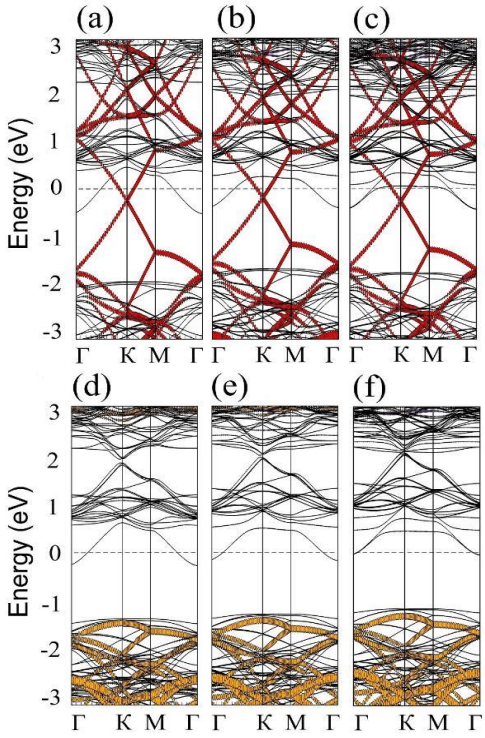

Fig. 5.10. The band structures for (a)–(c) InSe–graphene and (d)–(f) InSe–BN heterostructures with the K atom adsorbed at the distances of 3.0, 3.6 and 4.2 Å above the surface, respectively. The bands coloured in black, red, yellow and violet represent InSe, graphene, BN and K atom, respectively. The black dashed line shows the Fermi level.

The isosurface plots of DCD for K–doped InSe–graphene (Figs. 5.11(a)–(c)) and InSe–BN (Figs. 5.11(d)–(f)) heterostructures show a strong depletion of electrons in the K atom and an accumulation of electrons on the InSe surface for K at d = 3.0, 3.6 and 4.2 Å. As in the case of monolayer InSe, a linear increase of charge transfer from the K atom to the InSe surface with the decrease of d is revealed for both heterostructures (Fig. 5.11(g)).

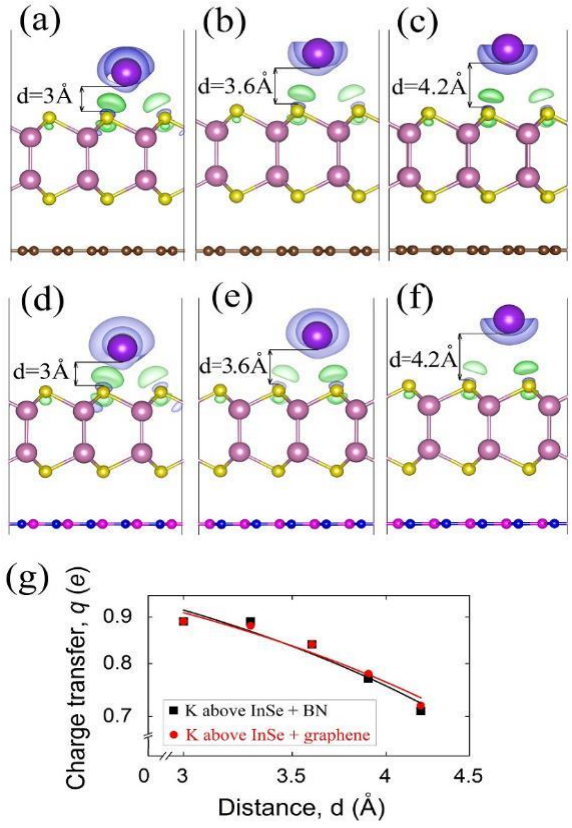

Fig. 5.11. The side view of the isosurface plots of the DCD, the blue (green) denotes depletion (accumulation) of electrons, for (a)–(c) InSe/graphene and (d)–(f) InSe–BN heterostructures with the K atom adsorbed at the distances of 3.0, 3.6 and 4.2 Å above the surface, respectively. The spheres coloured in yellow, violet, brown, pink, blue, and purple show selenium, indium, carbon, boron, nitrogen, and potassium atoms. (g) The variation of the charge transferred from the K atom to InSe–graphene (red line) and InSe–BN (black line) by changing the distance between the atom and the surface.

The maximum charge transfer from the K atom to both heterostructures reaches up to 0.89 *e*, which is almost the same as that for the monolayer case. This may be due to a strong acceptor ability of the InSe surface, which is able to accumulate charge from the K atom without transferring it to the substrate.

5.3 Summary

In Chapter 5, the strain effects on the electronic structure of the in-plane graphene–silicene heterostructure have been studied. Within the strain range from -7% (compression) to 7% (tension), the considered heterostructure is always metallic with the Dirac point being located above the Fermi level. The investigation of the strain effects on the chemical activity of the in-plane graphene/silicene heterostructure upon interaction with H_2O molecule has revealed that compressive strain can promote the adsorption of the H_2O molecule and increase the charge transfer, signifying an enhanced chemical activity. Furthermore, compressive and tensile strains have been found to be able to modulate the charge transfer between the H_2O molecule and the graphene/silicene surface, potentially allowing the control of polarity and concentration of charge carriers. In addition, the effect of the BN-substrate on the chemical activity of the in-plane graphene–silicene heterostructure upon interaction with the H_2O molecule has been considered. It has been found that the BN-substrate significantly influences the donor/acceptor ability of the H_2O molecule upon its adsorption on the graphene/silicene heterostructure and may cause an increase/decrease of the charge transfer between the H_2O molecule and heterostructure.

Further, the modulation of monolayer InSe electronic properties by encapsulation, surface functionalization, and molecular adsorption has been conducted. In particular, an opposite charge donating role of graphene (donor) and BN (acceptor) in InSe has been shown, which is dramatically different from phosphorene, where both graphene and BN play the same role (donor). A decrease in interlayer spacing between InSe and graphene (BN) can dramatically change the band alignment and tune the band gap. In addition, the effects of surface doping with the K atom on the band structure and charge transferability of InSe-based heterostructures have been studied. For the K-doped InSe–graphene and InSe–BN a linearly increasing charge transfer from the dopant to the InSe surface with a decreasing distance between them has been predicted.

The present study has not only revealed insights into the modulation of electronic properties of free-standing and substrate-supported graphene- and InSe–based heterostructures but also rendered new ways to control its electronic structure and carrier density, which may pay the way for the practical applications of the considered heterostructures in novel nanodevices.

Chapter 6 Conclusions and recommendations

In this chapter, the main conclusions are summarized, and future works are recommended based on the investigations conducted in the framework of this Ph.D. research.

6.1 Conclusions

The DFT-based first-principles simulation has been conducted to investigate the structural stability, electronic properties and chemical activity of 2D materials (phosphorene, borophene, InSe, and antimonene) and 2D heterostructures (graphene-silicene, InSe-graphene, and InSe-BN). The effects of various types of engineering factors have been studied, and their underlying mechanisms have been revealed. The methods for controlling electronic properties and chemical activity of the considered 2D systems have been proposed. In addition, the ways for preventing the structural degradation of the considered 2D systems have been discussed. More detailed conclusions of this work are the following:

- Rippling of phosphorene can lead to significant changes in its electronic properties. The strong spatial dependence of the electronic structure in rippled phosphorene along the periodic line profile may potentially allow the control of the carriers' transport via ripple engineering. The present work has explained the recent experiment that observes the spatially dependent optical properties in rippled phosphorene, where periodic ripples with large curvatures were obtained by transferring phosphorene to a greatly pre-stretched elastomeric substrate, followed by a relaxation of the pre-strain in the substrate. In addition, rippled phosphorene has been found to be able to promote the

adsorption of NO gas molecules and increase the charge transfer, signifying an enhanced chemical activity.

- Unlike other 2D materials, vacancy-containing phosphorene has been found to be almost inert to H_2O with the adsorption energy being almost the same as that in perfect phosphorene. For both perfect and vacancy-containing phosphorene, the H_2O molecule does not introduce any defect states in the band gap while the frontier orbitals of the O_2 molecule are aligned in the phosphorene band gap. The O_2 molecule increases the number of hole carriers and serves as a good electron scavenger for adsorption on perfect phosphorene. Vacancy-modulated charge transfer from H_2O and O_2 molecules may allow the modulation of the concentration and polarity of carriers in phosphorene. Finally, the kinetics analysis of the O_2 dissociation has shown that the oxidation rate is around 5000 times faster in the vacancy site than in the perfect site of phosphorene. Hence, phosphorene samples with a large number of vacancies should be more easily oxidized than those with the low vacancy concentration.
- The metallicity in borophene has been found to be immune to the presence of vacancies and the surface functionalization. Furthermore, the anisotropy of the electronic properties and the nature of the orbitals at the Fermi level can be altered upon the surface functionalization, enabling the modulation of the borophene properties. Due to the high density of itinerant electrons in the atomically thin borophene sheet, the band gap opening via quantum confinement, which is effective for graphene, becomes ineffective for borophene. In addition, it has been revealed that the work function of

borophene can be tuned to a large degree, as the high electronic gas confined in the atomically thin sheet of borophene can be transferred to the functionalizing groups.

- The oxidation of monolayer InSe by examining the roles of light illumination, oxygen, water, and defects has been explored. Perfect InSe has a much lower oxygen affinity than MoS_2 and phosphorene. However, the presence of the Se vacancy and light excitation significantly accelerates the oxidation by greatly decreasing the barrier through forming chemical oxygen species. These atomic O species, which are associated with strong polar O-In bonds, can quench the defective states of the Se vacancy, and further act as the adsorption and trapping centres of H_2O molecules. In addition, the spontaneous water splitting and the formation of hydroxyl groups at room temperature have been shown. Based on these findings, the following three strategies to suppress the oxidation of InSe have been proposed: i) insulating InSe from O_2 molecules; ii) maintaining the InSe surface stoichiometry; iii) avoiding the exposure of InSe to light illumination.
- The energetics and charge transfer of CO, NO, NO_2, H_2O, O_2, NH_3, and H_2 molecules adsorbed on antimonene have been studied. The NO, NO_2, H_2O, O_2, and NH_3 molecules have been found as effective acceptors to antimonene, while the H_2 molecule is a donor. The strong acceptors like NO_2, NO, and O_2 bind more strongly to the antimonene surface than the phosphorene surface, while the weak acceptors like CO, H_2, and NH_3 show a weaker adsorption. Additional examination of the kinetics process of the O_2 splitting on antimonene has shown a relatively low barrier of ~0.4 eV for the O_2 decomposition, suggesting that antimonene tends to be oxidized during

synthesis and applications largely due to the O_2 molecules rather than the water effect. The acceptor role of water impedes the interaction between water molecules and oxygen species on antimonene to form acids, which may be the underlying reason for the high stability of antimonene. The stable oxide layer may serve as a protecting coat for layers underneath it. While such oxide layer can serve as passivating and protecting coat for avoiding the degradation of layers underneath, for achieving a robust performance, potential antimonene devices still need to be protected via using non-covalent functionalization for suppressing the strong effect from environmental molecules, as predicted by this work.

- The strain effects on the electronic structure of the in-plane graphene/silicene heterostructure have been studied. Within the strain range from -7% (compression) to 7% (tension), the considered heterostructure is always metallic with the Dirac point being located above the Fermi level. The investigation of the strain effects on the chemical activity of the in-plane graphene/silicene heterostructure upon interaction with the H_2O molecule has revealed that compressive strain promotes the adsorption of H_2O molecules and increases the charge transfer, signifying an enhanced chemical activity. Furthermore, compressive and tensile strains have been found to be able to modulate the charge transfer between the H_2O molecule and graphene/silicene surface, potentially allowing the control of polarity and concentration of charge carriers. In addition, the BN-substrate has been found to significantly influence the donor/acceptor ability of the H_2O molecule upon its adsorption on the graphene/silicene heterostructure. This may cause a decrease/increase of the charge transfer between the H_2O molecule and heterostructure.

- The modulation of electronic properties of monolayer InSe by encapsulation, surface functionalization, and molecular adsorption has been found. An opposite charge donating role of graphene (donor) and BN (acceptor) in InSe, which is dramatically different from phosphorene, where both graphene and BN play the same role (donor), has been shown. A decrease in interlayer spacing between InSe-graphene/BN is able to dramatically change the band alignment and tune the band gap. The effects of surface doping with K atoms on the band structure and charge transferability of monolayer InSe have been considered. For K-doped InSe, a semiconductor to metal transition and a linearly increased charge transfer from the dopant to the InSe surface with a decreasing distance between them have been revealed. For the strong atomic donor like K, the charge transfer across the dopant-InSe interface is accompanied with a strong redistribution of the electric potential or field at the interface, which alters the photon kinetics and electron-hole recombination efficiency of InSe.

6.2 Recommendations

With regard to the structural stability, electronic properties, and chemical activity of 2D materials and its heterostructures, the following investigations are recommended.

- A comprehensive mechanical characterization of different 2D materials can be done. More specifically, a detailed analysis of the structural deformation and modulation of the electronic properties of phosphorene under the applied uniaxial compressive strain in the zigzag and armchair directions considered in this study can be adopted for other 2D materials, such as antimonene, InSe, arsenene etc.

- Experiments have revealed that 2D materials tend to suffer from a more rapid degradation, largely in form of oxidation, compared with bulk ones. Therefore, it is important to understand the degradation mechanisms which are predominantly involved with external adsorbates (O_2 and H_2O) at ambient conditions and it is critically important for practical applications of 2D materials. Based on the results obtained for phosphorene and InSe in this study, the investigation of degradation mechanisms of other 2D materials and their heterostructures is necessary for developing the unified mechanism for the control and suppression of the degradation of 2D systems during their synthesis, storage, and applications.
- Various approaches including functionalization, doping, and defect engineering can be adopted to enhance the properties of 2D systems. In addition, a proper composition of 2D materials may allow creating a heterostructure with the significantly improved performance compared to its individual components. Therefore, future work needs to be directed to the investigation of engineering effects and consideration of various combinations of 2D materials for achieving superior performances of 2D systems.
- Experimental verification and validation may have great importance for the continuation of this research. For instance, the findings from the first-principles investigations of the influence of mechanical deformation on the electronic properties of phosphorene are well agreed with experimental results. Moreover, theoretical calculations have allowed to confirm and explain predictions made in the experimental works. Hence, further experimental verification of the current study is not only of

scientific significance but also of great implication to the practical applications of 2D materials and their heterostructures.

References

[1] P. Miro, M. Audiffred, T. Heine. An atlas of two-dimensional materials. *Chemical Society Reviews,* 2014, **43**:6537−6554.

[2] F. Schwierz, J. Pezoldt, R. Granzner. Two-dimensional materials and their prospects in transistor electronics. *Nanoscale*, 2015, **7**:8261−8283.

[3] P. Vogt, P. De Padova, C. Quaresima, J. Avila, E. Frantzeskakis, M. C. Asensio, A. Resta, B. Ealet, G. Le Lay. Silicene: Compelling experimental evidence for graphene like two-dimensional silicon. *Physical Review Letters,* 2012, **108**:155501.

[4] M. E. Davila, L. Xian, S. Cahangirov, A. Rubio, G. Le Lay. Germanene: a novel two-dimensional germanium allotrope akin to graphene and silicene. *New Journal of Physics,* 2014, **16**:095002.

[5] A. Castellanos-Gomez, L. Vicarelli, E. Prada, J. O. Island, K. L. Narasimha-Acharya, S. I. Blanter, D. J. Groenendijk, M. Buscema, G. A. Steele, J. V. Alvarez, H. W. Zandbergen, J. J. Palacios, H. S. J. van der Zan. Isolation and characterization of few-layer black phosphorus. *2D Materials,* 2014, **1**:025001.

[6] W. Wei, Y. Dai, B. Huanga, T. Jacob. Many-body effects in silicene, silicane, germanene and germanane. *Physical Chemistry Chemical Physics,* 2013, **15**:8789−8794.

[7] B. Radisavljevic, A. Radenovic, J. Brivio, V. Giacometti, A. Kis. Single-layer MoS_2 transistors. *Nature Nanotechnology*, 2011, **6**:147−150.

[8] V. Wang, Y. Kawazoe, W. T. Geng. Native point defects in few-layer phosphorene. *Physical Review B,* 2015, **91**:045433.

[9] L. Kou, Y. Ma, S. C. Smith, C. Chen. Anisotropic ripple deformation in phosphorene. *The Journal of Physical Chemistry Letters*, 2015, **6**:1509−1513.

[10] V. Sorkin, Y. W. Zhang. The deformation and failure behavior of phosphorene nanoribbons under uniaxial tensile strain. *2D Materials*, 2015, **2**:035007.

[11] D. Cakir, H. Sahin, F. M. Peeters. Tuning of the electronic and optical properties of single-layer black phosphorus by strain. *Physical Review B*, 2014, **90**:205421.

[12] A. S. Rodin, A. Carvalho, A. H. Carlo Neto. Strain-induced gap modification in black phosphorus. *Physical Review Letters*, 2014, **112**:176801.

[13] Y. Cai, Q. Ke, G. Zhang, Y. W. Zhang. Energetics, charge transfer, and magnetism of small molecules physisorbed on phosphorene. *The Journal of Physical Chemistry C*, 2015, **119**:3102−3110.

[14] V. V. Kulish, O. I. Malyi, C. Persson, P. Wu. Adsorption of metal adatoms on single-layer phosphorene. *Physical Chemistry Chemical Physics*, 2015, **17**:992−1000.

[15] B. Ghosh, S. Nahas, S. Bhowmick, A. Agarwal. Electric field induced gap modification in ultrathin blue phosphorus. *Physical Review B*, 2015, **91**:115433.

[16] K. S. Novoselov, A. Mishchenko, A. Carvalho, A. H. Castro Neto. 2D materials and van der Waals heterostructures. *Science*, 2016, **353**:9439.

[17] P. Ajayan, P. Kim, K. Banerjee. Two-dimensional van der Waals materials. *Physics Today*, 2016, **69**:38–44.

[18] F. Bonaccorso, A. Lombardo, T. Hasan, Z. Sun, L. Colombo, A. C. Ferrari. Production and processing of graphene and 2D crystals. *Materials Today*, 2012, **15**:564–589.

[19] K. S. Novoselov, A. K. Geim, S. V. Morozov, D. Jiang, Y. Zhang, S. V. Dubonos, I. V. Grigorieva, A. A. Firsov. Electric field effect in atomically thin carbon films. *Science*, 2004, **306**:666–669.

[20] R. Dovesi, R. Orlando, A. Erba, C. M. Zicovich-Wilson, B. Civalleri, S. Casassa, L. Maschio, M. Ferrabone, M. De La Pierre, P. D'Arco, Y. N. Mauro Causà, M. Rérat, B, Kirtman. Crystal14: A program for the ab initio investigation of crystalline solids. *International Journal of Quantum Chemistry*, 2014, **114**:1287.

[21] J. M. Soler, E. Artacho, J. D. Gale, A. Garcia, J. Junquera, P. Ordejon, D. Sanchez-Portal. The SIESTA method for ab initio order-N materials simulation. *Journal of Physics: Condensed Matter*, 2002, **14**:2745–2779.

[22] G. te Velde, E. J. Baerends. Precise density-functional method for periodic structures. *Physical Review B*, 1991, **44**:7888.

[23] M. Franchini, P. H. T. Philipsen, L. Visscher. The Becke fuzzy cells integration scheme in the Amsterdam density functional program suite. *Journal of Computational Chemistry*, 2013, **34**:1818.

[24] P. H. T. Philipsen, G. te Velde, E. J. Baerends, J. A. Berger, P. L. de Boeij, M. Franchini, J. A. Groeneveld, E. S. Kadantsev, R. Klooster, F. Kootstra, P. Romaniello, M. Raupach, D. G. Skachkov, J. G. Snijders, C. J. O. Verzijl, J. A. Celis Gil, J. M. Thijssen, G. Wiesenekker, T. Ziegler. BAND2013. SCM, *Theoretical Chemistry*, Vrije Universiteit, Amsterdam, The Netherlands, 2013.

[25] G. Kresse, J. Furthmüller. Efficiency of *ab initio* total energy calculations for metals and semiconductors using a plane-wave basis set. *Computational Materials Science*, 1996, **6**:15.

[26] G. Kresse, J. Furthmüller. Efficient iterative schemes for ab initio total-energy calculations using a plane-wave basis set. *Physical Review B*, 1996, **54**:11169.

[27] X. Gonze, B. Amadon, P. M. Anglade, J.-M. Beuken, F. Bottin, P. Boulanger, et. al. Abinit: first-principles approach to material and nanosystem properties. *Computer Physics Communications*, 2009, **180**:2582–2615.

[28] P. Giannozzi, S. Baroni, N. Bonini, M. Calandra, R. Car, C. Cavazzoni, et. al. Quantum Espresso: A modular and open-source software project for quantum simulations of materials. *Journal of Physics: Condensed Matter*, 2009, **21**:395502.

[29] W. Koch, M. C. Holthausen. A chemist's guide to density functional theory. *Wiley-VCH*, **2001**.

[30] D. Becke. Density-functional exchange-energy approximation with correct asymptotic behavior. *Physical Review A*, 1988, **38**:3098–3100.

[31] J. P. Perdew, K. Burke, M. Ernzerhof. Generalized gradient approximation made simple. *Physical Review Letters*, 1996, **77**:3865–3868.

[32] Y. Yoon, K. Ganapathi, S. Sayeef. How good can monolayer MoS_2 transistors be?. *Nano Letters*, 2011, **11**:3768–3773.

[33] M. Orio, D. A. Pantazis, F. Neese. Density functional theory. *Photosynthesis Research*, 2009, **102**:443–453.

[34] Y. Zhao, D. G. Truhlar. Calculation of semiconductor band gaps with the M06-L density functional. *The Journal of Chemical Physics*, 2009, **130**:074103.

[35] N. Yakovkin, P. A. Dowben. The problem of the band gap in LDA calculations. *Surface Review and Letters*, 2007, **14**:481–487.

[36] H. Xiao, J. Tahir-Kheli, W. A. Goddard. Accurate band gaps for semiconductors from density functional theory. *The Journal of Physical Chemistry Letters*, 2011, **2**:212–217.

[37] X. Wu, E. J. Walter, A. M. Rappe, R. Car, A. Selloni. Hybrid density functional calculations of the band gap of $Ga_xIn_{1-x}N$. *Physical Review B,* 2009, **80**:115201.

[38] J. Heyd, G. E. Scuseria, M. Ernzerhof. Hybrid functionals based on a screened Coulomb potential. *The Journal of Chemical Physics,* 2003, **118**:8207–8215.

[39] C. Adamo, V. Barone. Toward reliable density functional methods without adjustable parameters: The PBE0 model. *The Journal of Chemical Physics*, 1999, **110**:6158–6170.

[40] P. Hohenberg, W. Kohn. Inhomogeneous electron gas. *Physical Review Journals*, 1964, **136**:864–871.

[41] W. Kohn, L. J. Sham. Self–consistent equations including exchange and correlation effects. *Physical Review Journals*, 1965, **140**:1133–1138.

[42] P. E. Blochl. Projector augmented–wave method. *Physical Review B*, 1994, **50**:17953–17979.

[43] G. Kresse, J. Hafner. Ab initio molecular dynamics for liquid metals. *Physical Review B*, 1993, **47**:558–561.

[44] C. Stefaan. *Density functional theory and the family of (L) APW methods: a step–by–step introduction*, 2nd edition. Instituut voor Kern- en Straligsfysica, KU Leuven, Belgium, 2013.

[45] M. Born, K. Huang. *Dynamical theory of crystal lattices*. New York: Clarendon Press, Oxford, 1998.

[46] M. J. Allen, V. C. Tung, R. B. Kaner. Honeycomb carbon: A review of graphene. *Chemical Reviews,* 2010, **110**:132–145.

[47] C. Berger, Z. Song, X. Li, X. Wu, N. Brown, C. Naud, D. Mayou, T. Li, J. Hass, A. N. Marchenkov, E. H. Conrad, P. N. First, W. A. de Heer. Electronic

confinement and coherence in patterned epitaxial graphene. *Science,* 2006, **312**:1191–1196.

[48] K. S. Kim, Y. Zhao, H. Jang, S. Y. Lee, J. M. Kim, K. S. Kim, J. H. Ahn, P. Kim, J. Y. Choi, B. H. Hong. Large-scale pattern growth of graphene films for stretchable transparent electrodes. *Nature*, 2009, **457**:706–710.

[49] S. Park, R. S. Ruoff. Chemical methods for the production of graphenes. *Nature Nanotechnology*, 2009, **4**:217–224.

[50] N. Behabtu, J. R. Lomeda, M. J. Green, A. L. Higginbotham, A. Sinitskii, D. V. Kosynkin, D. Tsentalovich, A. N. Parra-Vasquez, J. Schmidt, E. Kesselman, Y. Cohen, Y. Talmon, J. M. Tour, M. Pasquali. Spontaneous high-concentration dispersions and liquid crystals of graphene. *Nature Nanotechnology*, 2010, **5**:406–411.

[51] A. Castellanos-Gomez, M. Buscema, R. Molenaar, V. Singh, L. Janssen, H. S. J. van der Zant, G. A. Steele. Deterministic transfer of two-dimensional materials by all-dry viscoelastic stamping. *2D Materials*, 2014, **1**:011002.

[52] S. Tongay, W. Fan, J. Kang, J. Park, U. Koldemir, J. Suh, D. S. Narang, K. Liu, J. Ji, J. Li, R. Sinclair, J. Wu. Tuning interlayer coupling in large-area heterostructures with CVD grown MoS_2 and MoS_2 monolayers. *Nano Lett*ers, 2014, **14**:3185–3190.

[53] F. Ceballos, M. Z. Bellus, H. Y. Chiu, H. Zhao. Ultrafast charge separation and indirect exciton formation in a $MoS_2/MoSe_2$ van der Waals heterostructure. *ACS Nano*, 2014, **8**:12717–12724,

[54] Y. C. Lin, R. K. Ghosh, R. Addou, N. Lu, S. M. Eichfeld, H. Zhu, M. Y. Li, X. Peng, M. J. Kim, L. J. Li, R. M. Wallace, S. Datta, J. A. Robinson. Atomically thin resonant tunnel diodes built from synthetic van der Waals heterostructures. *Nature Commun*ications, 2015, **6**:7311.

[55] S. M. Eichfeld, L. Hossain, Y. C. Lin, A. F. Piasecki, B. Kupp, A. G. G. Birdwell, R. A. Burk, N. Lu, X. Peng, J. Li, A. Azcatl, S. McDonnell, R. M. Wallace, M. J. Kim, T. S. Mayer, J. M. Redwing, J. A. Robinson. Highly scalable, atomically thin WSe_2 grown via metal-organic chemical vapor deposition. *ACS Nano*, 2015, **9**:2080–2087.

[56] H. Liu, K. K. A. Antwi, S. Chua, D. Chi. Vapor-phase growth and characterization of $Mo_{(1-x)}W_{(x)}S_2$ ($0 \leq x \leq 1$) atomic layers on 2-inch sapphire substrates. *Nanoscale*, 2014, **6**:624–629.

[57] I. S. Kim, V. K. Sangwan, D. Jariwala, J. D. Wood, S. Park, K. S. Chen, F. Shi, F. Ruiz-Zepeda, A. Ponce, M. Jose-Yacaman, V. P. Dravid, T. J. Marks, M. C. Hersam, L. J. Lauhon. Influence of stoichiometry on the optical and electrical properties of chemical vapor deposition derived MoS_2. *ACS Nano*, 2014, **8**:10551–10558.

[58] U. Patil, S. C. Lee, S. Kulkarni, J. S. Sohn, M. S. Nam, S. H. Jun. Nanostructured pseudo capacitive materials decorated 3D graphene foam electrodes for next generation supercapacitors. *Nanoscale*, 2015, **7**:6999–7021.

[59] K. S. Novoselov, A. K. Geim, S. V. Morozov, D. Jiang, M. I. Katsnelson, I. V. Grigorieva, S. V. Dubonos, A. A. Firsov. Two-dimensional gas of massless Dirac fermions in graphene. *Nature*, 2005, **438**:197–200.

[60] S. V. Morozov, K. S. Novoselov, M. I. Katsnelson, F. Schedin, D. C. Elias, J. A. Jaszczak, A. K. Geim. Giant intrinsic carrier mobilities in graphene and its bilayer. *Physical Review Letters*, 2008, **100**:016602.

[61] J. H. Chen, C. Jang, S. Adam, M. S. Fuhrer, E. D. Williams, M. Ishigami. Charged-impurity scattering in graphene. *Nature Physics*, 2008, **4**:377–381.

[62] L. Banszerus, M. Schmitz, S. Engels, J. Dauber, M. Oellers, F. Haupt, K. Watanabe, T. Taniguchi, B. Beschoten, C. Stampfer. Ultrahigh-mobility

graphene devices from chemical vapor deposition on reusable copper. *Science Advances*, 2015, **1**:e1500222.

[63] Y. B. Zhang, Y. W. Tan, H. L. Stormer, P. Kim. Experimental observation of the quantum Hall effect and Berry's phase in graphene. *Nature*, 2005, **438**:201–204.

[64] L. Li, Y. Yu, G. J. Ye, Q. Ge, X. Ou, H. Wu, D. Feng, X. H. Chen, Y. Zhang. Black phosphorus field-effect transistors. *Nature Nanotechnol*ogy, 2014, **9**:372–377.

[65] J. Qiao, X. Kong, Z. X. Hu, F. Yang, W. Ji. High-mobility transport anisotropy and linear dichroism in few-layer black phosphorus. *Nature Communications*, 2014, **5**:4475.

[66] D. A. Bandurin, A. V. Tyurnina, G. L. Yu, A. Mishchenko, V. Zólyomi, S. V. Morozov, R. K. Kumar, R. V. Gorbachev, Z. R. Kudrynskyi, S. Pezzini, Z. D. Kovalyuk, U. Zeitler, K. S. Novoselov, A. Patanè, L. Eaves, I. V. Grigorieva, V. I. Fal'ko, A. K. Geim, Y. Cao. High electron mobility, quantum Hall effect and anomalous optical response in atomically thin InSe. *Nature Nanotechnology*, 2017, **12**:223–227.

[67] T. Cheng, H. Lang, Z. Li, Z. Liu, Z. Liu. Anisotropic carrier mobility in two-dimensional materials with tilted Dirac cones: Theory and application. *Physical Chemistry Chemical Physics*, 2017, **19**:23942–23950.

[68] Y. Wang, Y. Ding. Electronic Structure and carrier mobilities of arsenene and antimonene nanoribbons: A first-principle study. *Nanoscale Research Letters*, 2015, **10**:254.

[69] Z. Zhang, J. Xie, D. Yang, Y. Wang, M. Si, D. Xue, Manifestation of unexpected semiconducting properties in few-layer orthorhombic arsenene. *Applied Physics Express.* 2015, **8**:055201.

[70] S. Ghosh, I. Calizo, D. Teweldebrhan, E. P. Pokatilov, D. L. Nika, A. Balandin, W. Bao, F. Miao, C. N. Lau. Extremely high thermal conductivity of graphene: Prospects for thermal management applications in nanoelectronic circuits. *Applied Physics Letters,* 2008, **92**:151911–151913.

[71] S. Bae, H. Kim, Y. Lee, X. Xu, J. S. Park, Y. Zheng. Roll-to-roll production of 30-inch graphene films for transparent electrodes. *Nature Nanotechnol*ogy, 2010, **5**:574–578.

[72] R. S. Sundaram, M. Engel, A. Lombardo, R. Krupke, A. C. Ferrari, P. Avouris, M. Steiner. Electroluminescence in single layer MoS_2. *Nano Letters*, 2013, **13**:1416–1421.

[73] J. Y. Lin, C. Y. Chan, S. W. Chou. Electrophoretic deposition of transparent MoS_2-graphene nanosheet composite films as counter electrodes in dye-sensitized solar cells. *Chemical Communications,* 2013, **49**:1440–1442.

[74] L. Matthes, O. Pulci, F. Bechstedt. Massive Dirac quasiparticles in the optical absorbance of graphene, silicene, germanene, and tinene. *Journal of Physics: Condensed Matter,* 2013, **25**:395305.

[75] H. S. S. R. Matte, K. S. Subrahmanyam, C. N. R. Rao. Novel Magnetic properties of graphene: Presence of both ferromagnetic and antiferromagnetic features and other aspects. *The Journal of Physical Chemistry C,* 2009, **113**:9982–9985.

[76] S. Tongay, S. S. Varnoosfaderani, B. R. Appleton, J. Wu, A. F. Hebard. Magnetic properties of MoS_2: Existence of ferromagnetism. *Applied Physics Letters*, 2012, **101**:123105.

[77] C. Lee, X. Wei, J. W. Kysar, J. Hone. Measurement of the elastic properties and intrinsic strength of monolayer graphene. *Science,* 2008, **321**:385–388.

[78] F. Liu, P. Ming, J. Li. Ab initio calculation of ideal strength and phonon instability of graphene under tension. *Physical Review B,* 2007, **76**:064120.

[79] A. Castellanos-Gomez, M. Poot, G. A. Steele, H. S. J. van der Zant, N. Agraït, G.Rubio-Bollinger. Elastic properties of freely suspended MoS_2 nanosheets. *Advanced Materials*, 2012, **24**:772–775.

[80] A. Kis, D. Mihailovic, M. Remskar, A. Mrzel, A. Jesih, I. Piwonski, A. J. Kulik, W. Benoît, L. Forró. Shear and Young's moduli of MoS_2 nanotube ropes. *Advanced Materials*, 2003, **15**:733–736.

[81] J. W. Jiang, H. S. Park. Mechanical properties of MoS_2/graphene heterostructures. *Applied Physics Letters*, 2014, **105**:033108.

[82] J. W. Jiang, H. S Park. Mechanical properties of single-layer black phosphorus. *Journal of Physics D: Applied Physics*, 2014, **47**:385304.

[83] Q. Wei, X. Peng. Superior mechanical flexibility of phosphorene and few-layer black phosphorus. *Applied Physics Letters*, 2014, **104**:251915.

[84] J. W. Jiang, H. S. Park. Negative poisson's ratio in single-layer black phosphorus. *Nature Communications*, 2014, **5**:4727.

[85] S. M. Choi, S. H. Jhi, Y. W. Son. Effects of strain on electronic properties of graphene. *Physical Review B*, 2010, **81**:081407.

[86] M. Mohr, K. Papagelis, J. Maultzsch, C. Thomsen. Two-dimensional electronic and vibrational band structure of uniaxially strained graphene from ab initio calculations. *Physical Review B*, 2009, **80**:205410.

[87] V. M. Pereira, A. H. Castro Neto. Tight-binding approach to uniaxial strain in graphene. *Physical Review B*, 2009, **80**:045401.

[88] A. Castellanos-Gomez, R. Roldan, E. Cappelluti, M. Buscema, F. Guinea, H. S. J. van der Zant, G. A. Steele. Local strain engineering in atomically thin MoS_2. *Nano Letters*, 2013, **13**:5361–5366.

[89] H. Pan, Y. W. Zhang. Tuning the electronic and magnetic properties of MoS_2 nanoribbons by strain engineering. *The Journal of Physical Chemistry C*, 2012, **116**:11752–11757.

[90] Y. Y. Hui, X. Liu, W. Jie, N. Y. Chan, J. Hao, Y. T. Hsu, L. J. Li, W. Guo, S. P. Lau. Exceptional tunability of band energy in a compressively strained trilayer MoS_2 sheet. *ACS Nano*, 2013, **7**:7126–7131.

[91] X. Peng, Q. Wei, A. Copple. Strain-engineered direct-indirect band gap transition and its mechanism in two-dimensional phosphorene. *Physical Review B*, 2014, **90**:085402.

[92] Z. Y. Ong, Y. Cai, G. Zhang, Y. W. Zhang. Strong thermal transport anisotropy and strain modulation in single-layer phosphorene. *The Journal of Physical Chemistry C*, 2014, **118**:25272–25277.

[93] R. Qin, C. H. Wang, W. Zhu, Y. Zhang. First-principles calculations of mechanical and electronic properties of silicene under strain. *AIP Advances*, 2012, **2**:022159.

[94] M. Hu, X. Zhang, D. Poulikakos. Anomalous thermal response of silicene to uniaxial stretching. *Physical Review B*, 2013, **87**:195417.

[95] Y. Wanga, Y. Ding. Strain-induced self-doping in silicene and germanene from first-principles. *Solid State Communications*, 2013, **155**:6–11.

[96] E. V. Castro, K. S. Novoselov, S. V. Morozov, N. M. R. Peres, J. M. B. L. dos Santos, J. Nilsson, F. Guinea, A. K. Geim, A. H. Castro Neto. Biased bilayer

graphene: semiconductor with a gap tunable by the electric field effect. *Physical Review Letters*, 2007, **99**:216802.

[97] J. Qi, X. Li, X. Qian, J. Feng. Bandgap engineering of rippled MoS_2 monolayer under external electric field. *Applied Physics Letters*, 2013, **102**:173112.

[98] Q. Liu, L. Li, Y. Li, Z. Gao, Z. Chen, J. Lu. Tuning electronic structure of bilayer MoS_2 by vertical electric field: A first-principles investigation. *The Journal of Physical Chemistry C*, 2012, **116**:21556–21562.

[99] Z. Ni, Q. Liu, K. Tang, J. Zheng, J. Zhou, R. Qin, Z. Gao, D. Yu, J. Lu. Tunable bandgap in silicene and germanene. *Nano Letters*, 2012, **12**:113–118.

[100] Q. Liu, X. Zhang, L. B. Abdalla, A. Fazzio, A. Zunger. Switching a normal insulator into a topological insulator via electric field with application to phosphorene. *Nano Letters*, 2015, **15**:1222–1228.

[101] Y. G. Zhou, X. T. Zu, F. Gao, H. F. Lv, H. Y. Xiao. Adsorption-induced magnetic properties and metallic behavior of graphene. *Applied Physics Letters*, 2009, **95**:123119.

[102] K. T. Chan, J. B. Neaton, M. L. Cohen. First-principles study of metal adatom adsorption on graphene. *Physical Review B*, 2008, **77**:235430.

[103] Y. H. Zhang, Y. B. Chen, K. G. Zhou, C. H. Liu, J. Zeng, H. L. Zhang, Y. Peng. Improving gas sensing properties of graphene by introducing dopants and defects: A first-principles study. *Nanotechnology*, 2009, **20**:185504.

[104] J. He, K. Wu, R. Sa, Q. Li, Y. Wei. Magnetic properties of nonmetal atoms absorbed MoS_2 monolayers. *Applied Physics Letters*, 2010, **96**:082504.

[105] J. Sivek, H. Sahin, B. Partoens, F. M. Peeters. Adsorption and absorption of boron, nitrogen, aluminum, and phosphorus on silicene: Stability and electronic and phonon properties. *Physical Review B*, 2013, **87**:85444.

[106] Y. Jing, Q. Tang, P. He, Z. Zhou, P. Shen. Small molecules make big differences: molecular doping effects on electronic and optical properties of phosphorene. *Nanotechnology*, 2015, **26**:095201.

[107] P. Zhang, X. D. Li, C. H. Hu, S. Q. Wu, Z. Z. Zhu. First-principles studies of the hydrogenation effects in silicene sheets. *Physics Letters A*, 2012, **376**:1230–1233.

[108] C. Grazianetti, D. Chiappe, E. Cinquanta, G. Tallarida, M. Fanciulli, A. Molle. Exploring the morphological and electronic properties of silicene superstructures. *Applied Surface Science*, 2014, **291:**109–112.

[109] J. I. Paredes, S. Villar-Rodil, P. Solís-Fernández, M. J. Fernández-Merino, L. Guardia, A. Martínez-Alonso, J. M. D. Tascón. Preparation, characterization and fundamental studies on graphenes by liquid-phase processing of graphite. *Journal of Alloys and Compounds*, 2012, **536**:450–455.

[110] Q. Li, B. W. Noffke, Y. Liu, L. Li. Understanding fundamental processes in carbon materials with well-defined colloidal graphene quantum dots. *Current Opinion in Colloid & Interface Science*, 2015, **20**:346–353.

[111] M. A. Milani, D. González, R. Quijada, N. R. S. Basso, M. L. Cerrada, D. S. Azambuja, G. B. Galland. Polypropylene/graphene nanosheet nanocomposites by in situ polymerization: Synthesis, characterization and fundamental properties. *Composites Science and Technology*, 2013, **84**:1–7.

[112] A. Kara, C. Léandri, M. E. Dávila, P. De Padova, B. Ealet, H. Oughaddou, B. Aufray, G. L. Lay. Physics of silicene stripes. *Journal of Superconductivity and Novel Magnetism*, 2009, **22**:259–263.

[113] S. Yu, W. Zheng. Fundamental insights into the electronic structure of zigzag MoS_2 nanoribbons. *Physical Chemistry Chemical Physics*, 2016, **18**:4675–4683.

[114] Y. Lin, X. Li, D. Xie, T. Feng, Y. Chen, R. Song, H. Tian, T. Ren, M. Zhong, K. Wang, H. Zhu. Graphene/semiconductor heterojunction solar cells with modulated antireflection and graphene work function. *Energy & Environmental Science,* 2013, **6**:108.

[115] M. L. Tsai, S. H. Su, J. K. Chang, D. S. Tsai, C. H. Chen, C. I Wu, L. J. Li, L. J. Chen, J. H. He. Monolayer MoS_2 heterojunction solar cells. *ACS Nano*, 2014, **8**:8317–8322.

[116] Y. Deng, Z. Luo, N. J. Conrad, H. Liu, Y. Gong, S. Najmaei, P. M. Ajayan, J. Lou, X. Xu, P. D. Ye. Black phosphorus-monolayer MoS_2 van der Waals heterojunction p-n diode. *ACS Nano,* 2014, **8**:8292–8299.

[117] S. S. Varghes, S. H. Varghese, S. Swaminathan, K. K. Singh, V. Mittal. Two-dimensional materials for sensing: graphene and beyond. *Electronics*, 2015, **4**:651–687.

[118] S. H. Bae, Y. Lee, B. K. Sharma, H. J. Lee, J. H. Kim, J. H. Ahn. Graphene-based transparent strain sensor. *Carbon,* 2013, **51**:236–242.

[119] S. E. Zhu, M. K. Ghatkesar, C. Zhang, G. C. A. M. Janssen. Graphene based piezoresistive pressure sensor. *Applied Physics Letters*, 2013, **102**:161904.

[120] V. Sorkin, Y. W. Zhang. Graphene-based pressure nano-sensors. *Journal of Molecular Modeling*, 2011, **17**:2825–2830.

[121] Y. Wang, Z. Shi, Y. Huang, Y. Ma, C. Wang, M. Chen, Y. Chen. Supercapacitor devices based on graphene materials. *The Journal of Physical Chemistry C*, 2009, **113**:13103–13107.

[122] J. Cao, Y. Wang, Y. Zhou, J. H. Ouyang, D. Jia, L. Guo. High voltage asymmetric supercapacitor based on MnO_2 and graphene electrodes. *Journal of Electroanalytical Chemistry*, 2013, **689**:201–206.

[123] Y. Xie, Y. Liu, Y. Zhao, Y. H. Tsang, S. P. Lau, H. Huanga, Y. Chai. Stretchable all-solid-state supercapacitor with wavy shaped polyaniline/graphene electrode. *Journal of Materials Chemistry A*, 2014, **2**:9142–9149.

[124] L. Cao, S. Yang, W. Gao, Z. Liu, Y. Gong, L. Ma, G. Shi, S. Lei, Y. Zhang, S. Zhang, R. Vajtai, P. M. Ajayan. Direct laser-patterned micro-supercapacitors from paintable MoS_2 films. *Small*, 2013, **9**:2905–2910.

[125] N. Choudhary, M. Patel, Y. H. Ho, N. B. Dahotre, W. Lee, J. Y. Hwang, W. Choi. Directly deposited MoS_2 thin film electrodes for high performance supercapacitors. *Journal of Materials Chemistry A*, 2015, **3**:24049–24054.

[126] K. J. Huang, L. Wang, Y. J. Liu, Y. M. Liu, H. B. Wang, T. Gan, et. al. Layered MoS_2-graphene composites for supercapacitor applications with enhanced capacitive performance. *International Journal of Hydrogen Energy*, 2013, **38**:14027–14034.

[127] M. A. Bissett, I. A. Kinloch, R. A. W. Dryfe. Characterization of MoS_2−Graphene composites for high performance coin cell supercapacitors. *ACS Applied Materials & Interfaces*, 2015, **7**:17388−17398.

[128] F. Xia, S. Kwon, W. W. Lee, Z. Liu, S. Kim, T. Song., K. J. Choi, U. Paik, W. Park. Graphene as an interfacial layer for improving cycling performance of Si nanowires in lithium-ion batteries. *Nano Lett*ers, 2015, **15**:6658−6664.

[129] S. Zhao, W. Kangab, J. Xuea. The potential application of phosphorene as an anode material in Li-ion batteries. *Journal of Materials Chemistry A*, 2014, **2**:19046–19052.

[130] G. C. Guo, D. Wang, X. L. Wei, Q. Zhang, H. Liu, W. M. Lau, L. M. Liu. First-principles study of phosphorene and graphene heterostructure as anode materials for rechargeable Li batteries. *The Journal of Physical Chemistry Letters*, 2015, **6**:5002−5008.

[131] V. V. Kulish, O. I. Malyi, C. Perssoncd, P. Wu. Phosphorene as an anode material for Na-ion batteries: A first-principles study. *Physical Chemistry Chemical Physics*, 2015, **17**:13921−13928.

[132] T. Ramireddy, T. Xing, M. M. Rahman, Y. Chen, Q. Dutercq, D. Gunzelmanna, A. M. Glushenkov. Phosphorus–carbon nanocomposite anodes for lithium-ion and sodium-ion batteries. *Journal of Materials Chemistry A*, 2015, **3**:5572–5584.

[133] J. Sun, H. W. Lee, M. Pasta, H. Yuan, G. Zheng, Y. Sun, Y. Li, Y. Cui. A phosphorene-graphene hybrid material as a high-capacity anode for sodium-ion batteries. *Nature Nanotechnol*ogy, 2015, **10**:280–286.

[134] J. Chang, C. Hobbs. Theoretical study of phosphorene tunneling field effect transistors. *Applied Physics Letters*, 2015, **106**:083509.

[135] S. Das, M. Demarteau, A. Roelofs. Ambipolar phosphorene field effect transistor. *ACS Nano*, 2014, **8**:11730–11738.

[136] J. W. González, F. Delgado, J. Fernández-Rossier. Graphene single-electron transistor as a spin sensor for magnetic adsorbates. *Physical Review B*, 2013, **87**:085433.

[137] L. Vicarelli, M. S. Vitiello, D. Coquillat, A. Lombardo, A. C. Ferrari, W. Knap, M. Polini, V. Pellegrini, A. Tredicucci. Graphene field-effect transistors as room-temperature terahertz detectors. *Nature Materials*, 2012, **11**:865–871.

[138] X. Li, H. Zhu, K. Wang, A. Cao, J. Wei, C. Li, Y. Jia, Z. Li, X. Li, D. Wu. Graphene-on-silicon Schottky junction solar cells. *Advanced Materials*, 2010, **22**:2743–2748.

[139] P. Dutta, P. M. Horn. Low-frequency fluctuations in solids: 1/f noise. *Reviews of Modern Physics*, 1981, **53**:497–516.

[140] F. Schedin, A. K. Geim, S. V. Morozov, E. W. Hill, P. Blake, M. I. Katsnelson, K. S. Novoselov. Detection of individual gas molecules adsorbed on graphene. *Nature Materials*, 2007, **6**:652−655.

[141] O. Leenaerts, B. Partoens, F. M. Peeters. Adsorption of H_2O, NH_3, CO, NO_2, and NO on graphene: A first-principles study. *Physical Review B*, 2008, **77**:125416.

[142] A. C. Crowther, A. Ghassaei, N. Jung, L. E. Brus. Strong charge-transfer doping of 1 to 10 layer graphene by NO_2. *ACS Nano*, 2012, **6**:1865−1875.

[143] L. Kou, T. Frauenheim, C. Chen. Phosphorene as a superior gas sensor: selective adsorption and distinct I–V response. *The Journal of Physical Chemistry Letters*, 2014, **5**:2675−2681.

[144] W. Hu, N. Xia, X. Wu, Z. Liab, J. Yang. Silicene as a highly sensitive molecule sensor for NH_3, NO and NO_2. *Physical Chemistry Chemical Physics*, 2014, **16**:6957−6962.

[145] W. Xia, W. Hu, Zh. Lia, J. Yang. A first-principles study of gas adsorption on germanene. *Physical Chemistry Chemical Physics*, 2014, **16**:22495−22498.

[146] G. Henkelman, B. P. Uberuaga, H. Jonsson. A climbing image nudged elastic band method for finding saddle points and minimum energy paths. *The Journal of Chemical Physics*, 2000, **113**:9901.

[147] Y. Cai, G. Zhang, Y. W. Zhang. Electronic properties of phosphorene/graphene and phosphorene/hexagonal boron nitride heterostructures. *The Journal of Physical Chemistry C*, 2015, **119**:13929−13936.

[148] J. Feng, X. Qian, C. W Huang, J. Li. Strain-engineered artificial atom as a broad-spectrum solar energy funnel. *Nature Photonics*, 2012, **6**:866−872.

[149] Y. Liu, P. Stradins, S. H. Wei. Air passivation of chalcogen vacancies in two-dimensional semiconductors. *Angewandte Chemie International Edition*, 2016, **55**:965–968.

[150] T. Hu, J. Dong. Geometric and electronic structures of mono- and di-vacancies in phosphorene. *Nanotechnology*. 2015, **26**:065705.

[151] W. Hu, J. Yang. Defects in phosphorene. *The Journal of Physical Chemistry C*, 2015, **119**:20474–20480.

[152] P. Srivastava, K. P. S. S. Hembram, H. Mizuseki, K. R. Lee, S. S. Han, S. Kim. Tuning the electronic and magnetic properties of phosphorene by vacancies and adatoms. *The Journal of Physical Chemistry C*, 2015, **119**:6530–6538.

[153] Y. Cai, Q. Ke, G. Zhang, B. I. Yakobson, Y. W. Zhang. Highly itinerant atomic vacancies in phosphorene. *Journal of the American Chemical Society*, 2016, **138**:10199–10206.

[154] Y. Okamoto, Y. J. Miyamoto. Ab initio investigation of physisorption of molecular hydrogen on planar and curved graphenes. *The Journal of Physical Chemistry B*, 2001, **105**:3470−3474.

[155] A. L. Va´zquez de Parga, F. Calleja, B. Borca, M. C. G. Passeggi, Jr. Hinarejos, J. J. Guinea, R. Miranda. Periodically rippled graphene: growth and spatially resolved electronic structure. *Physical Review Letters*, 2008, **100**:056807.

[156] D. Boukhvalov, M. Katsnelson. Enhancement of chemical activity in corrugated graphene. *The Journal of Physical Chemistry C*, 2009, **113**:14176−14178.

[157] V. Atanasov, A. Saxena. Tuning the electronic properties of corrugated graphene: Confinement, curvature, and band-gap opening. *Physical Review B*, 2010, **81**:205409.

[158] H. Pan, B. Chen. Ultra-flexibility and unusual electronic, magnetic and chemical properties of waved graphenes and nanoribbons. *Scientific Reports*, 2014, **4**:4198.

[159] Y. L. Song, Y. Zhang, J. M. Zhang, D.B. Lu, K. W. Xu. First-principles study of the structural and electronic properties of armchair silicene nanoribbons with vacancies. *Journal of Molecular Structure,* 2011, **990**:75–78

[160] O. V. Yazyev, L. Helm. Defect-induced magnetism in graphene. *Physical Review B*, 2007, **75**:125408

[161] C. Ataca, H. Sahin, E. Akturk, S. Ciraci. Mechanical and electronic properties of MoS_2 nanoribbons and their defects. *The Journal of Physical Chemistry C*, 2011, **115**:3934–3941.

[162] Y. Liu, F. Xu, Z. Zhang, E. S. Penev, B. I. Yakobson. Two-dimensional mono-elemental semiconductor with electronically inactive defects: the case of phosphorus. *Nano Letters,* 2014, **14**:6782–6786.

[163] J. Kang, J. D. Wood, S. A. Wells, J. H. Lee, X. Liu, K. S. Chen, M. C. Hersam. Solvent exfoliation of electronic-grade, two-dimensional black phosphorus. *ACS Nano*, 2015, **9**:3596–3604.

[164] M. Serrano-Ruiz, M. Caporali, A. Ienco, V. Piazza, S. Heun, M. Peruzzini. The role of water in the preparation and stabilization of high-quality phosphorene flakes. *Advanced Materials Interfaces*, 2016, **3**:1500441.

[165] E. Passaglia, F. Cicogna, G. Lorenzetti, S. Legnaioli, M. Caporali, M. Serrano-Ruiz, A. Ienco, M. Peruzzini. Novel polystyrene-based nanocomposites by phosphorene dispersion. *RSC Adv*ances, 2016, **6**:53777–53783.

[166] A. Ziletti, A. Carvalho, D. K. Campbell, D. F. Coker, A. H. Castro Neto. Oxygen defects in phosphorene. *Physical Review Letters*, 2015, **114**:046801.

[167] R. F. W. Bader. *Atoms in Molecules - A Quantum Theory*. Oxford University Press: New York, 1990.

[168] J. Quereda, P. San-Jose, V. Parente, L. Vaquero-Garzon, A. J. Molina-Mendoza, N. Agraït, G. Rubio-Bollinger, F. Guinea, R. Roldán, A. Castellanos-Gomez. Strong modulation of optical properties in black phosphorus through strain-engineered rippling. *Nano Letters*, 2016, **16**:2931–2937.

[169] A. J. Mannix, X. F. Zhou, B. Kiraly, J. D. Wood, D. Alducin, B. D. Myers, X. Liu, B. L. Fisher, U. Santiago, J. R. Guest, M. J. Yacaman, A. Ponce, A. R. Oganov, M. C. Hersam, N. P. Guisinger. Synthesis of borophenes: Anisotropic, two-dimensional boron polymorphs. *Science*, 2015, **350**:1513–1516.

[170] B. Feng, J. Zhang, Q. Zhong, W. Li, S. Li, H. Li, P. Cheng, S. Meng, L. Chen, K. Wu. Experimental realization of two-dimensional boron sheets. *Nature Chemistry*, 2016, **8**:563–568.

[171] Z. Zhang, A. J. Mannix, Z. Hu, B. Kiraly, N. P. Guisinger, M. C. Hersam, B. I. Yakobson. Substrate-induced nanoscale undulations of borophene on silver. *Nano Letters*, 2016, **16**:6622–6627.

[172] D. V. P. Massote, L. Liang, N. Kharche, V. Meunier. Electronic, vibrational, Raman, and scanning tunneling microscopy signatures of two-dimensional boron nanomaterials. *Physical. Review B*, 2016, **94**:195416.

[173] Z. A. Piazza, H. S. Hu, W. L. Li, Y. F. Zhao, J. Li, L. S. Wang. Planar hexagonal B_{36} as a potential basis for extended single-atom layer boron sheets. *Nature Communications*, 2014, **5**:3113.

[174] S. Jalife, L. Liu, S. Pan, J. L. Cabellos, E. Osorio, C. Lu, T. Heine, K. J. Donald, G. Merino. Dynamical behavior of boron clusters. *Nanoscale*, 2016, **8**:17639.

[175] B. Feng, J. Zhang, R. Y. Liu, T. Limori, C. Lian, H. Li, L. Chen, K. Wu, S. Meng, F. Komori, I. Matsuda. Direct evidence of metallic bands in a monolayer boron sheet. *Physical Review B*, 2016, **94**:041408.

[176] Y. Liu, Y. J. Dong, Z. Tang, X. F. Wang, L. Wang, T. Hou, H. Lin, Y. Li. Stable and metallic borophene nanoribbons from first-principles calculations. *Journal of Materials Chemistry C*, 2016, **4**:6380–6385.

[177] H. Gao, L. Wang, J. Zhao, F. Ding, J. Lu. Band Gap Tuning of hydrogenated graphene: H coverage and configuration dependence. *The Journal of Physical Chemistry C*, 2011, **115**:3236–3242.

[178] X. Niu, H. Shu, Y. Li, J. Wang. Photoabsorption tolerance of intrinsic point defects and oxidation in black phosphorus quantum dots. *The Journal of Physical Chemistry Letters*, 2017, **8**:161–166.

[179] Y. Du, J. Zhuang, H. Liu, X. Xu, S. Eilers, K. Wu, P. Cheng, J. Zhao, X. Pi, K. W. See, G. Peleckis, X. Wang, S. X. Dou. Tuning the band gap in silicene by oxidation. *ACS Nano*, 2014, **8**:10019–10025.

[180] A. R. Oganov, J. Chen, C. Gatti, Y.; Ma, C. W. Glass, Z. Liu, T. Yu, O. O. Kurakevych, V. L. Solozhenko. Ionic high-pressure form of elemental boron. *Nature*, 2009, **457**:863.

[181] G. Hummer, L. R. Pratt, A. E. Garcia. Free energy of ionic hydration. *The Journal of Physical Chemistry*, 1996, **100**:1206.

[182] E. S. Penev, A. Kutana, B. I. Yakobson. Can two-dimensional boron superconduct?. *Nano Lett*ers, 2016, **16**:2522–2526.

[183] A. Lherbier, A. R. Botello-Méndez, J. C. Charlier. Electronic and optical properties of pristine and oxidized borophene. *2D Materials*, 2016, **3**:045006.

[184] H. Shu, F. Li, P. Liang, X. Chen. Unveiling the atomic structure and electronic properties of atomically thin boron sheets on an Ag(111) surface. *Nanoscale*, 2016, **8**:16284.

[185] E. J. H. Lee, K. Balasubramanian, R. T. Weitz, M. Burghard, K. Kern. Contact and edge effects in graphene devices. *Nature Nanotechnology*, 2008, **3**:486–490.

[186] J. A. Robinson, M. LaBella, M. Zhu, M. Hollander, R. Kasarda, Z. Hughes, K. Trumbull, R. Cavalero, D. Snyder. Contacting graphene. *Applied Physics Letters*, 2011, **98**:053103.

[187] Y. Cai, A. Zhang, Y. P. Feng, C. Zhang, H. F. Teoh, G. W. Ho. Strain effects on work functions of pristine and potassium-decorated carbon nanotubes. *The Journal of Chemical Physics*, 2009, **131**:224701.

[188] Y. Cai, G. Zhang, Y. W. Zhang. Layer-dependent band alignment and work function of few-layer phosphorene. *Scientific Reports*, 2014, **4**:6677.

[189] Q. Zhou, Q. Chen, Y. Tong, J. Wang. Light-induced ambient degradation of few-layer black phosphorus: mechanism and protection. *Angewandte Chemie International Edition*, 2016, **128**:11609–11613.

[190] Y. Cai, H. Zhou, G. Zhang, Y. W. Zhang. Modulating carrier density and transport properties of MoS_2 by organic molecular doping and defect engineering. *Chemistry of Materials*, 2016, **28**:8611–8621.

[191] W. Wu, W. Guo, X. C. Zeng. Intrinsic electronic and transport properties of graphyne sheets and nanoribbons. *Nanoscale*, 2013, **5**:9264–9276.

[192] J. Kibsgaard, T. F. Jaramillo. Molybdenum phosphosulfide: an active, acid-stable, earth-abundant catalyst for the hydrogen evolution reaction. *Angewandte Chemie International Edition*, 2014, **53**:14433–14437.

[193] Z. Luo, P. M. Vora, E. J. Mele, A. T. C. Johnson, J. M. Kikkawa. Photoluminescence and band gap modulation in graphene oxide. *Applied Physics Letters*, 2009, **94**:111909.

[194] A. Favron, E. Gaufres, F. Fossard, A. L. P. Heureux, N. Y. W. Tang, P. L. Levesque, A. Loiseau, R. Leonelli, S. Francoeur, R. Martel. Photooxidation and quantum confinement effects in exfoliated black phosphorus. *Nature Materials*, 2015, **14**:826.

[195] S. R. Tamalampudi, Y. Y. Lu, U. R. Kumar, R. Sankar, C. D. Liao, B. K. Moorthy, C. H. Cheng, F. C. Chou, Y. T. Chen. High performance and bendable few-layered InSe photodetectors with broad spectral response. *Nano Letters*, 2014, **14**:2800–2806.

[196] J. Lauth, A. Kulkarni, F. C. M. Spoor, N. Renaud, F. C. Grozema, A. J. Houtepen, J. M. Schins, S. Kinge, L. D. A. Siebbeles. Photogeneration and mobility of charge carriers in atomically thin colloidal InSe nanosheets probed by ultrafast terahertz spectroscopy. *The Journal of Physical Chemistry Letters*, 2016, **7**:4191–4196.

[197] D. A. Bandurin, A. V. Tyurnina, G. L. Yu, A. Mishchenko, V. Zo´lyomi, S. V. Morozov, R. K. Kumar, R. V. Gorbachev, Z. R. Kudrynskyi, S. Pezzini, Z. D. Kovalyuk, U. Zeitler, K. S. Novoselov, A. Patane`, L. Eaves, I. V. Grigorieva, V. I. Fal'ko, A. K. Geim, Y. Cao. High electron mobility, quantum Hall effect and anomalous optical response in atomically thin InSe. *Nature Nanotechnology*, 2017, **12**:223–227.

[198] S. Lei, X. Wang, B. Li, J. Kang, Y. He, A. George, L. Ge, Y. Gong, P. Dong, Z. Jin, G. Brunetto, W. Chen, Z. T. Lin, R. Baines, D. S. Galva˜o, J. Lou, E. Barrera, K. Banerjee, R. Vajtai and P. Ajayan. Surface functionalization of two-dimensional metal chalcogenides by Lewis acid–base chemistry. *Nature Nanotechnology*, 2016, **11**:465–471.

[199] G. W. Mudd, M. R. Molas, X. Chen, V. Zo´lyomi, K. Nogajewski, Z. R. Kudrynskyi, Z. D. Kovalyuk, G. Yusa, O. Makarovsky, L. Eaves, M. Potemski, V. I. Falko, A. Patane. The direct-to-indirect band gap crossover in two-dimensional van der Waals indium selenide crystals. *Scientific Reports*, 2016, **6**:39619.

[200] S. Lei, L. Ge, S. Najmaei, A. George, R. Kappera, J. Lou, M. Chhowalla, H. Yamaguchi, G. Gupta, R. Vajtai, A. D. Mohite, P. M. Ajayan. Evolution of the electronic band structure and efficient photo-detection in atomic layers of InSe. *ACS Nano*, 2014, **8**:1263–1272.

[201] K. Xu, L. Yin, Y. Huang, T. A. Shifa, J. Chu, F. Wang, R. Cheng, Z. Wang, J. He. Synthesis, properties and applications of 2D layered $M^{III}X^{VI}$ (M = Ga, In; X = S, Se, Te) materials. *Nanoscale*, 2016, **8**:16802–16818.

[202] M. A. Airo, S. Gqoba, M. P. Kalenga, S. Govindraju, M. J. Moloto, N. Moloto. Synthesis and characterization of indium monoselenide nanosheets: A proposed pseudo top-down mechanism. *Journal of Crystal Growth*, 2014, **406**:1–7.

[203] M. Brotons-Gisbert, J. F. Sanchez-Royo and J. P. Martınez-Pastor. Thickness identification of atomically thin InSe nanoflakes on SiO_2/Si substrates by optical contrast analysis. *Applied Surface Science*, 2015, **354**:453–458.

[204] W. Feng, W. Zheng, X. Chen, G. Liu, W. Cao, P. Hu. Solid-state reaction synthesis of a InSe/$CuInSe_2$ lateral p–n heterojunction and application in high performance optoelectronic devices. *Chemistry of Materials*, 2015, **27**:983–989.

[205] Z. Chen, J. Biscaras, A. Shukla. A high performance graphene/few-layer InSe photo-detector. *Nanoscale*, 2015, **7**:5981–5986.

[206] Y. Cai, G. Zhang, Y. W. Zhang, Charge transfer and functionalization of monolayer InSe by physisorption of small molecules for gas sensing. *The Journal of Physical Chemistry C*, 2017, **121**:10182–10193.

[207] G. W. Mudd, S. A. Svatek, T. Ren, A. Patane`, O. Makarovsky, L. Eaves, P. H. Beton, Z. D. Kovalyuk, G. V. Lashkarev, Z. R. Kudrynskyi, A. I. Dmitriev. Tuning the bandgap of exfoliated InSe nanosheets by quantum confinement. *Advanced Materials*, 2013, **25**:5714–5718.

[208] D. V. Rybkovskiy, A. V. Osadchy, E. D. Obraztsova. Transition from parabolic to ring-shaped valence band maximum in few-layer GaS, GaSe, and InSe. *Physical Review B: Condensed Matter and Materials Physics*, 2014, **90**:235302.

[209] C. M. Chow, H. Yu, A. M. Jones, J. Ya, D. G. Mandrus, T. Taniguchi, K. Watanabe, W. Yao, X. Xu. Unusual exciton–phonon interactions at van der Waals engineered interfaces. *Nano Letters*, 2017, **17**:1194–1199.

[210] W. Luo, Y. Cao, P. Hu, K. Cai, Q. Feng, F. Yan, T. Yan, X. Zhang, K. Wang. Gate tuning of high-performance InSe-based photodetectors using graphene electrodes. *Advanced Optical Materials*, 2015, **3**:1418–1423.

[211] N. Balakrishnan, Z. R. Kudrynskyi, E. F. Smith, M. W. Fay, O. Makarovsky, Z. D. Kovalyuk, L. Eaves, P. H. Beton, A. Patane. Engineering p–n junctions and bandgap tuning of InSe nanolayers by controlled oxidation. *2D Materials*, 2017, **4**:025043.

[212] S. Zhang, Z. Yan, Y. Li, Z. Chen and H. Zeng. Atomically thin arsenene and antimonene: semimetal-semiconductor and indirect-direct band-gap transitions. *Angewandte Chemie International Edition*, 2015, **54**:3112–3115.

[213] P. Ares, F. Aguilar-Galindo, D. Rodriguez-San-Miguel, D. A. Aldave, S. Diaz-Tendero, M. Alcami, F. Martin, J. Gomez-Herrero, F. Zamora. Mechanical isolation of highly stable antimonene under ambient conditions. *Advanced Materials*, 2016, **28**:6332–6336.

[214] J. Ji, X. Song, J. Liu, Z. Yan, C. Huo, S. Zhang, M. Su, L. Liao, W. Wang, Z. Ni, Y. Hao, H. Zeng. Two-dimensional antimonene single crystals grown by van der Waals epitaxy. *Nature Communications*, 2016, **7**:13352.

[215] P. Ares, J. J. Palacios, G. Abellán, J. Gómez-Herrero, F. Zamora. Recent progress on antimonene: A new bidimensional material. *Advanced Materials*, 2018, **30**:1703771.

[216] S. Zhang, M. Xie, F. Li, Z. Yan, Y. Li, E. Kan, W. Liu, Z. Chen, H. Zeng. Semiconducting group 15 monolayers: A broad range of band gaps and high carrier mobilities. *Angewandte Chemie International Edition*, 2016, **55**:1666–1669.

[217] C. Kamal, M. Ezawa. Arsenene: Two-dimensional buckled and puckered honeycomb arsenic systems. *Physical Review B*, 2015, **91**:085423.

[218] G. Wang, R. Pandey, S. P. Karna. Atomically thin group V elemental films: Theoretical investigations of antimonene allotropes. *ACS Applied Materials & Interfaces*, 2015, **7**:11490–11496.

[219] J. Gao, G. Zhang, Y. W. Zhang. Vastly enhancing the chemical stability of phosphorene by employing an electric field. *Nanoscale*, 2017, **9**:4219−4226.

[220] Y. Cai, Z. Bai, H. Pan, Y. P. Feng, B. I. Yakobson, Y. W. Zhang. Constructing metallic nanoroads on a MoS_2 monolayer via hydrogenation. *Nanoscale*, 2014, **6**:1691−1697.

[221] D. J. Late, Y. K. Huang, B. Liu, J. Acharya, S. N. Shirodkar, J. Luo, A. Yan, D. Charles, U. V. Waghmare, V. P. Dravid, C. N. R. Rao. Sensing behavior of atomically thin-layered MoS_2 transistors. *ACS Nano*, 2013, **7**:4879−4891.

[222] Ü. O. Aktürk, E. Aktürk, S. Ciraci. Effects of adatoms and physisorbed molecules on the physical properties of antimonene. *Physical Review B*, 2016, **93**:035450.

[223] Ü. O. Aktürk, O. V. Özçelik, S. Ciraci. Single-layer crystalline phases of antimony: Antimonenes. *Physical Review B*, 2015, **91**:235446.

[224] S. Cui, H. Pu, S. A. Wells, Z. Wen, S. Mao, J. Chang, M. C. Hersam, J. Chen. Ultrahigh sensitivity and layer-dependent sensing performance of phosphorene-based gas sensors. *Nature Communications*, 2015, **6**:8632.

[225] C. Ataca, E. Aktürk, S. Ciraci, H. Ustunel. High-capacity hydrogen storage by metallized graphene. *Applied Physics Letters*, 2008, **93**:043123.

[226] C. Gibaja, D. Rodriguez-San-Miguel, P. Ares, J. Gomez-Herrero, M. Varela, R. Gillen, J. Maultzsch, F. Hauke, A. Hirsch, G. Abellan, F. Zamora. Few-layer antimonene by liquid-phase exfoliation. *Angewandte Chemie International Edition*, 2016, **55**:14345–14349.

[227] S. Zhang, W. Zhou, Y. Ma, J. Ji, B. Cai, S. A. Yan, Z. Zhu, Z. Chen, H. Zeng. Antimonene oxides: Emerging tunable direct bandgap semiconductor and novel topological insulator. *Nano Lett*ers, 2017, **17**:3434–3440.

[228] Y. Huang, J. Qiao, K. He, S. Bliznakov, E. Sutter, X. Chen, D. Luo, F. Meng, D. Su, J. Decker, W. Ji, R. S. Ruoff, P. Sutter. Interaction of black phosphorus with oxygen and water. *Chemistry of Materials*, 2016, **28**:8330–8339.

[229] Y. Cai, Q. X. Pei, G. Zhang, Y. W. Zhang. Decoupled electron and phonon transports in hexagonal boron nitride silicene bilayer heterostructure. *Journal of Applied Physics*, 2016, **119**:065102.

[230] A. K. Geim, I. V. Grigorieva. Van der Waals heterostructures. *Nature*, 2013, **499**:419–425.

[231] H. Wang, F. Liu, W. Fu, Z. Fang, W. Zhou, Z. Liu. Two dimensional heterostructures: fabrication, characterization, and application. *Nanoscale*, 2014, **6**:12250–12272.

[232] G. R. Berdiyorov, M. Neek-Amal, F. M. Peeters, A. C. T. van Duin. Stabilized silicene within bilayer graphene: A proposal based on molecular dynamics and density-functional tight-binding calculations. *Physical Review B*, 2014, **89**:024107.

[233] S. J. Haigh, A. Gholinia, R. Jalil, S. Romani, L. Britnell, D. C. Elias, K. S. Novoselov, L. A. Ponomarenko, A. K. Geim, R. Gorbachev. Cross-sectional imaging of individual layers and buried interfaces of graphene-based heterostructures and superlattices. *Nature Materials*, 2012, **11**:764–767.

[234] Y. Gong, J. Lin, X. Wang, G. Shi, S. Lei, Z. Lin, X. Zou, G. Ye, R. Vajtai, B. I. Yakobson, H. Terrones, M. Terrones, B. K. Tay, J. Lou, S. T. Pantelides, Z. Liu, W. Zhou, P. M. Ajayan. Vertical and in-plane heterostructures from WS_2/MoS_2 monolayers. *Nature Materials*, 2014, **13**:1135–1142.

[235] Q. Sun, Y. Dai, Y. Ma, W. Wei, B. Huang. Lateral heterojunctions within monolayer h-BN/graphene: A first principles study. *RSC Advances*, 2015, **5**:33037.

[236] Z. Huang, C. He, X. Qi, H. Yang, W. Liu, X. Wei, X. Peng, J. Zhong. Band structure engineering of monolayer MoS_2 on h-BN: First-principles calculations. *Journal of Physics D: Applied Physics*, 2014, **47**:075301.

[237] A. Ramasubramaniam, D. Naveh, E. Towe. Tunable band gaps in bilayer graphene-BN heterostructures. *Nano Letters*, 2011, **11**:1070–1075.

[238] C. Guoxin. Atomistic studies of mechanical properties of graphene. *Polymers*, 2014, **6**:2404–2432.

[239] X. Liu, Z. Li. Electric field and strain effect on graphene-MoS_2 hybrid structure: ab initio calculations. *The Journal of Physical Chemistry Letters*, 2015, **6**:3269–3275.

[240] Y. Gao, Y. Zhang, P. Che, Y. Li, M. Liu, T. Gao, D. Ma, Y. Chen, Z. Cheng, X. Qiu, W. Duan, Z. Liu. Towards single layer uniform hexagonal boron nitride-graphene patchworks with zigzag linking edges. *Nano Lett*ers, 2013, **13**:3439–3443.

[241] W. Hu, Z. Li, J. Yang. Water on silicene: A hydrogen bond-autocatalyzed physisorption–chemisorption–dissociation transition. *Nano Research*, 2017, **10**:2223.

[242] J. Lauth, F. E. S. Gorris, M. S. Khoshkhoo, T. Chassé, W. Friedrich, V. Lebedeva, A. Meyer, C. Klinke, A. Kornowski, M. Scheele, H. Weller. Solution-processed two-dimensional ultrathin InSe nanosheets. *Chemistry of Materials*, 2016, **28**:1728–1736.

[243] M. Osman, Y. Huang, W. Feng, G. Liu, Y. Qiu, P. Hu. Modulation of opto-electronic properties of InSe thin layers via phase transformation. *RSC Advances*, 2016, **6**:70452.

[244] L. Shi, Q. Zhou, Y. Zhao, Y. Ouyang, C. Ling, Q. Li, J. Wang. Oxidation mechanism and protection strategy of ultrathin indium selenide: Insight from theory. *The Journal of Physical Chemistry Letters*, 2017, **8**:4368−4373.

[245] T. Hu, J. Hong. Anisotropic effective mass, optical property, and enhanced band gap in BN/phosphorene/BN heterostructures. *ACS Applied Materials & Interfaces*, 2015, **7**:23489–23495.

[246] H. J. Chuang, B. Chamlagain, M. Koehler, M. M. Perera, J. Yan, D. Mandrus, D. Tomanek, Z. Zhou. Low-resistance 2D/2D ohmic contacts: A universal

approach to high-performance WSe_2, MoS_2, and $MoSe_2$ transistors. *Nano Letters*, 2016, **16**:1896–1902.

[247] T. Ohta, A. Bostwick, T. Seyller, K. Horn, E. Rotenberg. Controlling the electronic structure of bilayer graphene. *Science*, 2006, **313**:951–954.

[248] J. Kim, S. S. Baik, S. H. Ryu, Y. Sohn, S. Park, B. G. Park, J. Denlinger, Y. Yi, H. J. Choi. K. S. Kim. Observation of tunable band gap and anisotropic Dirac semimetal state in black phosphorus. *Science*, 2015, **349**:723–726.

[249] C. Han, Z. Hu, L. C. Gomes, Y. Bao, A. Carvalho, S. J. R. Tan, B. Lei, D. Xiang, J. Wu, D. Qi, L. Wang, F. Huo, W. Huang, K. P. Loh, W. Chen. Surface functionalization of black phosphorus via potassium toward high-performance complementary devices. *Nano Letters*, 2017, **17**:4122–4129.